COHERENT X-RAY DIFFRACTION

BY

JOHN ALLEN PITNEY

B.S., University of Missouri–Columbia, 1995
M.S., University of Illinois at Urbana-Champaign, 1999

THESIS

Submitted in partial fulfillment of the requirements
for the degree of Doctor of Philosophy in Physics
in the Graduate College of the
University of Illinois at Urbana-Champaign, 2000

Urbana, Illinois

Red-Border Form Placed Here

COHERENT X-RAY DIFFRACTION

John Allen Pitney, Ph.D.
Department of Physics
University of Illinois at Urbana-Champaign, 2000
Ian K. Robinson, Advisor

Conventional x-ray diffraction has historically been done under conditions such that the measured signal consists of an incoherent addition of scattering which is coherent only on a length scale determined by the the properties of the beam. The result of the incoherent summation is a statistical averaging over the whole illuminated volume of the sample, which yields certain kinds of information with a high degree of precision and has been key to the success of x-ray diffraction in a variety of applications. Coherent x-ray scattering techniques, such as coherent x-ray diffraction (CXD) and x-ray intensity fluctuation spectroscopy (XIFS), attempt to reduce or eliminate any incoherent averaging so that specific, local structures couple to the measurement without being averaged out. In the case of XIFS, the result is analogous to dynamical light scattering, but with sensitivity to length scales less than 200 nm and time scales from 10^{-3} s to 10^{3} s. When combined with phase retrieval, CXD represents an imaging technique with the penetration, *in situ* capabilities, and contrast mechanisms associated with x-rays and with a spatial resolution ultimately limited by the x-ray wavelength. In practice, however, the spatial resolution of CXD imaging is limited by exposure to about 100 Å. This thesis describes CXD measurements of the binary alloy Cu_3Au and the adaptation of phase retrieval methods for the reconstruction of real-space images of Cu_3Au antiphase domains.

The theoretical foundations of CXD are described in Chapter 1 as derived from the kinematical formulation for x-ray diffraction and from the temporal and spatial coherence of radiation. The antiphase domain structure of Cu_3Au is described, along with the associated reciprocal-space structure which is measured by CXD. CXD measurements place relatively stringent requirements on the coherence properties of the

beam and on the detection mechanism of the experiment; these requirements and the means by which they have been met are delineated in Chapter 2. The results and interpretation of a set of Cu_3Au measurements are presented in Chapter 3. Chapter 4 describes the Gerchberg-Saxton and the hybrid input-output (HIO) algorithms for phase retrieval and shows the results of image reconstruction tests with simulated Cu_3Au CXD, including the effect of oversampling in reciprocal space.

Acknowledgements

I would like to express my gratitude to Ian K. Robinson, under whose direction I have been fortunate to pursue the research described in this thesis. His deep understanding of x-ray diffraction physics and his expertise with synchrotron x-ray experiments have benefitted me greatly.

I also have a great appreciation for the opportunity to interact with Ivan A. Vartaniants, a visiting theoretical physicist from the Institute for Crystallography, Russian Academy of Sciences. A number of my personal insights with regard to coherent x-ray diffraction have come about as a result of many fruitful discussions with him.

Other graduate students in Professor Robinson's research group have very often been a source of moral support and technical insight, and my sincere thanks go to Kevin Whiteaker, Don Walko, Yong Chu, Chinkyo Kim, David Fanning, and Mark Pfeifer.

Jeff Libbert, a former postdoc with the group, deserves credit for the roller-blade slits which comprise a critical part of the experimental setup I have used. Also I learned a great deal about coherent x-ray diffraction from him during the beginning of my graduate study.

My wife and my best friend, Julie, has been a constant source of support and encouragement. Her contribution to this work cannot be overstated.

The staff scientists at the UNICAT beamline at the Advanced Photon Source (APS) have been very helpful in the experiments described below. In particular, I

would like to thank Paul Zschack, Associate Director of UNICAT, and Beam Line Scientists Hawoong Hong and Pete R. Jemian for their assistance in setting up the experiment at beamline 33-ID-D. They have succeeded in providing an efficient and state-of-the-art user facility.

The UNICAT facility located at the APS is supported by the University of Illinois, Materials Research Laboratory, the Oak Ridge National Laboratory, the National Institute for Standards and Technologies, and UOP Research & Development. The APS is supported by the U.S. Department of Energy, BES, Office of Energy Research under contract No. W-31-109-ENG-38.

I gratefully acknowledge fellowship support for the 1998-1999 academic year from the National Science Foundation (NSF) under grant number DGE93-54978. This work was also supported by the NSF under project number DMR98-76610. The University of Illinois Materials Research Laboratory is supported by the U.S. Department of Energy under grant number DEFG02-96ER45439.

Contents

List of Tables

List of Figures

Chapter 1

Introduction

1.1 X-ray Diffraction

X-ray diffraction has a long history of significant contributions to widely varying fields of scientific study. By providing a probe of the structure of materials on the length scale of single atoms, x-ray diffraction has made possible the atomic-scale study of a wide array of materials, including metals, semiconductors, alloys, ceramics, and biological macromolecules. Inherent in conventional x-ray diffraction measurements, or those conducted with the sample under illumination by a beam lacking spatial coherence, is an ensemble averaging over the illuminated volume of the sample. The reason this averaging occurs will be discussed below. Often, the averaging is desirable, as it allows atomic-scale quantities to be measured over a region of micrometers or millimeters with great statistical precision.

Information about the sample is lost in this averaging process; however, coherent scattering measurements can be sensitive to specific local structures within the sample or to changes within the sample which do not alter its statistical properties. This thesis concerns exploiting the former kind of sensitivity in order to *image* local structures within a sample by a technique which will be referred to as coherent x-ray diffraction (CXD). The latter asset of coherent x-ray scattering measurements has found

several applications already in the form of x-ray intensity fluctuation spectroscopy (XIFS), also known as x-ray photon correlation spectroscopy (XPCS). Essentially the extension of laser-light dynamical light scattering to x-ray wavelengths with the concomitant sensitivity to fluctuations on a smaller length scale, XIFS measurements have been reported on critical fluctuations of the binary alloy Fe_3Al [1]; diffusion of colloidal particles of gold [2], palladium [3], and antimony oxide [4]; equilibrium dynamics of block-copolymer micelles [5], a polymer gel, and a single crystal of an AlLi alloy [6]; and nonequilibrium dynamics of phase separation in sodium borosilicate glass [7].

Two concepts of x-ray diffraction theory which are fundamental to the development of CXD presented here are the structure factor and the Ewald construction. These are introduced in Ref. [8], and are summarized in the following sections.

1.1.1 The Structure Factor and Bragg Reflections

The diffracted signal from a crystal is typically dominated by elastically scattered x-rays from the electrons in the specimen. For a beam polarized perpendicular to the plane of scattering, the amplitude A scattered from a single free electron is given by the Thomson scattering cross section,

$$A = A_0 \frac{e^2}{mc^2 R}\,, \tag{1.1}$$

where A_0 is the incident beam amplitude, e is the electron charge, m is the electron mass, c is the speed of light, and R is the distance from the electron to the detector. Thus, the incoming plane wave is scattered into a spherical wave. For a beam polarized in the plane of scattering, which will not be the case for vertically scattering synchrotron measurements such as reported here, there is an additional factor of $\cos\,'2\theta'$, where '2θ' is the scattering angle. Usually, the classical electron radius, which will be used for the remainder of this section, is defined in the following

manner:

$$r_e \equiv \frac{e^2}{mc^2} \approx 2.818 \times 10^{-15} \text{ m}\,. \tag{1.2}$$

In a solid, the electrons are mostly located at the positions of the atoms. The diffracted amplitude from an atom is the coherent superposition of the amplitudes scattered from each of its Z electrons,

$$A = A_0 \frac{r_e}{R} e^{ikR} \sum_{n=1}^{Z} e^{i\mathbf{q}\cdot\mathbf{r}_n}\,, \tag{1.3}$$

where $\mathbf{r}$ is the location of each electron in the atom, and $\mathbf{q}$, called the momentum transfer, is defined

$$\mathbf{q} \equiv \mathbf{k}_f - \mathbf{k}_i\,, \tag{1.4}$$

where $\mathbf{k}_i$ and $\mathbf{k}_f$ are the incident and final scattering wavevectors, respectively, each with magnitude $k = 2\pi/\lambda$. Here it is assumed that the atom is much smaller than the distance from the atom to the detector, so that R is the same for each electron. The sum over the n electrons should in fact be recast using a fully quantum-mechanical treatment of the scattering of photons by a multielectron atom, which can be found elsewhere [9]. It is referred to as the atomic scattering factor, $f(q)$, and computed values of $f(q)$ are found in tabulated form [10]. Note that $f(q)$ approaches Z as q becomes small. Typically, f is written

$$f = f_0 + \Delta f' + i\Delta f''\,, \tag{1.5}$$

where $\Delta f' + i\Delta f''$, called the dispersion correction, becomes significant near absorption edges of the atom. The atomic scattering factor as described here assumes spherical symmetry of the atom; however, this is not always strictly true.

The scattered amplitude from a single unit cell of a crystal lattice is given by the sum of the amplitudes scattered by the atoms in the unit cell:

$$A = A_0 \frac{r_e}{R} e^{ikR} \sum_{j=1} f_j(q) e^{i\mathbf{q}\cdot\mathbf{r}_j}\,, \tag{1.6}$$

where f_j is the atomic scattering factors for the jth atom in the unit cell, and r_i is the position of the atom relative to some point in the unit cell. The structure factor, $F(\mathbf{q})$, is defined

$$F(\mathbf{q}) \equiv \sum_{j=1} f_j(q) e^{i\mathbf{q}\cdot\mathbf{r}_j} \,. \tag{1.7}$$

In the case of a crystal specimen, the amplitude of the scattered beam at the detector will be the sum of the amplitudes scattered by the crystal's unit cells. Often, the extent of the illuminated region in the crystal will be such that not every pair of scatterers will interfere coherently at the detector. In that case, a rather complicated mixture of coherent and incoherent addition of signals occurs instead, giving rise to a kind of ensemble average over the illuminated sample region. Consider a grouping of unit cells small enough that coherent addition of scattered amplitude is appropriate. For the sake of simplicity, let the grouping be in the shape of a parallelpipedon with its edges of length $N_1 a_1$, $N_2 a_2$, and $N_2 a_2$ parallel to the crystal axes $\mathbf{a}_1$, $\mathbf{a}_2$, and $\mathbf{a}_3$. It is straightforward to generalize to any other shape of crystal. The scattered amplitude from this grouping is

$$A = A_0 \frac{r_e}{R} e^{ikR} F(\mathbf{q}) \sum_{m_1=0}^{N_1-1} \sum_{m_2=0}^{N_2-1} \sum_{m_3=0}^{N_3-1} e^{i\mathbf{q}\cdot(m_1\mathbf{a}_1 + m_2\mathbf{a}_2 + m_2\mathbf{a}_2)} \,. \tag{1.8}$$

The sums can be separated to obtain

$$A = A_0 \frac{r_e}{R} e^{ikR} F(\mathbf{q}) \sum_{m_1=0}^{N_1-1} e^{im_1\mathbf{q}\cdot\mathbf{a}_1} \sum_{m_2=0}^{N_2-1} e^{im_2\mathbf{q}\cdot\mathbf{a}_2} \sum_{m_3=0}^{N_3-1} e^{im_3\mathbf{q}\cdot\mathbf{a}_3} \,. \tag{1.9}$$

The quantity that is typically measured by a detector is the intensity, $I = A^* A$, which after substituting the above and simplifying becomes

$$I = A_0^* A_0 \left(\frac{r_e}{R}\right) F^*(\mathbf{q}) F(\mathbf{q}) \frac{\sin^2 \frac{1}{2} N_1 \mathbf{q}\cdot\mathbf{a}_1}{\sin^2 \frac{1}{2}\mathbf{q}\cdot\mathbf{a}_1} \frac{\sin^2 \frac{1}{2} N_2 \mathbf{q}\cdot\mathbf{a}_2}{\sin^2 \frac{1}{2}\mathbf{q}\cdot\mathbf{a}_2} \frac{\sin^2 \frac{1}{2} N_3 \mathbf{q}\cdot\mathbf{a}_3}{\sin^2 \frac{1}{2}\mathbf{q}\cdot\mathbf{a}_3} \,. \tag{1.10}$$

For the large values of N_1, N_2, and N_3 which are typical in a measurement, the result is that the scattered intensity is nearly zero except when the following equations,

known as the Laue equations, hold:

$$\begin{aligned} \mathbf{q} \cdot \mathbf{a}_1 &= 2\pi h \,, \\ \mathbf{q} \cdot \mathbf{a}_2 &= 2\pi k \,, \\ \mathbf{q} \cdot \mathbf{a}_3 &= 2\pi l \,, \end{aligned} \tag{1.11}$$

with h, k, and l having integer values. A Bragg reflection occurs when the Laue equations hold, provided that the structure factor is nonzero; the case of $F(\mathbf{q}) = 0$ with integer hkl is referred to as a "forbidden reflection." Bragg reflections will be denoted using (hkl) notation, with overbars indicating negative numbers.

1.1.2 The Ewald Construction

The momentum transfer vector, $\mathbf{q}$, indicates a location in *reciprocal space* which is being probed by the experiment. A convenient and standard basis for use in reciprocal space is defined by

$$\mathbf{b}_1 = 2\pi \frac{\mathbf{a}_2 \times \mathbf{a}_3}{\mathbf{a}_1 \cdot \mathbf{a}_2 \times \mathbf{a}_3} \,, \quad \mathbf{b}_2 = 2\pi \frac{\mathbf{a}_3 \times \mathbf{a}_1}{\mathbf{a}_1 \cdot \mathbf{a}_2 \times \mathbf{a}_3} \,, \quad \mathbf{b}_3 = 2\pi \frac{\mathbf{a}_1 \times \mathbf{a}_2}{\mathbf{a}_1 \cdot \mathbf{a}_2 \times \mathbf{a}_3} \,. \tag{1.12}$$

This allows writing the momentum transfer as

$$\mathbf{q} = h\mathbf{b}_1 + k\mathbf{b}_2 + l\mathbf{b}_3 \,. \tag{1.13}$$

The Ewald sphere, a very powerful construction, aids in visualizing the scattering process and locating Bragg reflections. The sphere has a radius k, and its center located at $-\mathbf{k}_i$, as shown in Figure 1.1. For a given $\mathbf{k}_i$, all points $\mathbf{q} = \mathbf{k}_f - \mathbf{k}_i$ lie on the sphere. Where a point with integer-valued hkl lies on the sphere, a Bragg reflection can be observed. Reorientation of the sample changes the direction of $\mathbf{k}_i$, which reorients the Ewald sphere with respect to the origin.

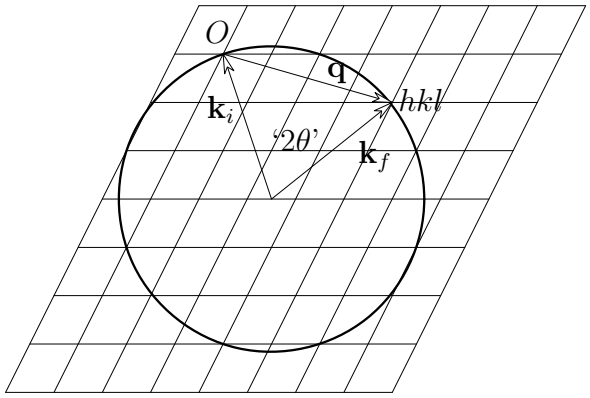

Figure 1.1: Ewald sphere construction. Shown is the the two-dimensional slice containing the scattering plane and the center of the Ewald sphere. At the **q** shown, a Bragg reflection may be observed, as a reciprocal lattice point lies on the Ewald sphere at that position.

1.2 Coherence

1.2.1 Temporal and Spatial Coherence

The coherence properties of a beam are generally described in terms of two types of coherence, temporal (or longitudinal) and spatial (or lateral). Both types play a large role in the theory of CXD. A more thorough development of coherence can be found in the excellent text by Born and Wolf [11].

The temporal coherence of a beam is a measure of the ability of the beam to interfere with itself after part of the beam has experienced a time delay with respect to the other part. The time delay is introduced by means of a path length difference (PLD), as in a Michelson interferometer. Temporal coherence is characterized by a temporal coherence length, $\xi_{\parallel}$, measured parallel to the direction of the beam propagation. As the PLD exceeds $\xi_{\parallel}$, the addition of the beam and the time-delayed beam gradually switches from complex-amplitude addition in the purely coherent case to real-valued intensity addition in the purely incoherent case. The régime in between is that of partially coherent interference, which will be treated in the following section.

The temporal coherence length is determined by the length of the individual wave

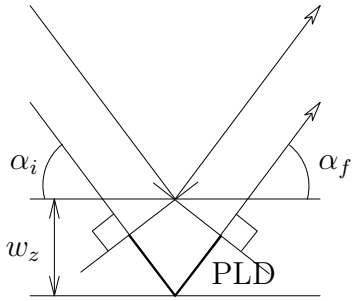

Figure 1.2: Penetration depth and PLD. The lower beam experiences an optical path length difference PLD $= w_z(\sin\alpha_i + \sin\alpha_f)$, where α_i and α_f are the angles shown, measured relative to the sample surface.

trains present in the beam. By analogy to the Heisenberg uncertainty relation from quantum mechanics, the temporal duration of the wave trains, Δt, and the spread in frequency of the wave trains, $\Delta\nu$, have an inverse relationship:

$$\Delta t\,\Delta\nu \geq \frac{1}{4\pi}\,. \tag{1.14}$$

In most cases, one only requires an order-of-magnitude comparison between $\xi_\parallel$ and some PLD, so the relation

$$\xi_\parallel = c\Delta t \sim \frac{c}{\Delta\nu} = \frac{\lambda^2}{\Delta\lambda}\,, \tag{1.15}$$

where λ is the mean wavelength, is convenient. Hence, $\xi_\parallel$ is a property of the monochromator in an experiment.

The effect of the temporal coherence length on a CXD or other coherent scattering experiment is typically on the penetration depth which can be allowed before contrast is lost. The PLD introduced by penetration into a sample is illustrated in Fig. 1.2. The penetration depth, measured normal to the surface of the sample, is calculated using the mass attenuation coefficients, at the appropriate beam energy, for the materials present in the sample. For a sample composed of N elements, the penetration depth is given by

$$w_z = \left(\sum_{j=1}^{N}\rho_j\mu_j\right)^{-1}\frac{\sin\alpha_i\sin\alpha_f}{\sin\alpha_i+\sin\alpha_f}\,, \tag{1.16}$$

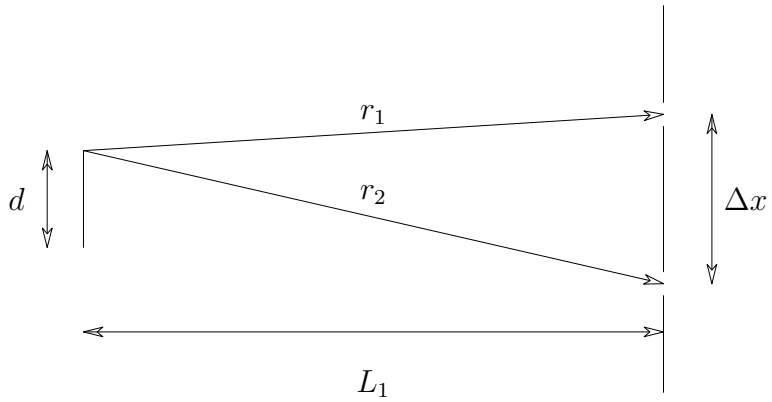

Figure 1.3: Double slit construction for spatial coherence length. An extended incoherent source of size d is located a distance L_1 from a pair of slits separated by a distance $\Delta x \ll L_1$.

where ρ_j is the mass density of element j, μ_j is its mass attenuation coefficient, and α_i and α_f are the angles of incidence and exit relative to the surface, respectively. The mass densities are available in tabular form [12]. Of course, for a thin film specimen, w_z can be limited to the thickness of the film.

Most conventional synchrotron x-ray diffraction experiments are carried out with a beam which has been passed through some type of monochromator and have adequate temporal coherence for the CXD measurements described in Chapter 3. For reflection-geometry CXD experiments involving samples with large penetration depths, however, the temporal coherence length may be inadequate to provide full coherence over the entire illuminated volume. This may be addressed by using grazing incidence or by preparing a thin film specimen.

The requirement for doing CXD which does severely impact experiment design is for spatial coherence. The spatial coherence of a beam characterizes the correlation in phase across the wavefront in the direction perpendicular to the beam's propagation. A Young's double slit experiment yields fringes only when the separation between the slits does not greatly exceed the spatial coherence length of the beam. A qualitative description of the origin of the spatial coherence length can be described using the construction shown in Figure 1.3. If the extended source is taken to be completely

incoherent, it consists of a collection of infinitesimal points sources which are uncorrelated with respect to one another. Such a description models a wide variety of sources, including synchrotrons and x-ray tubes, but it does *not* accurately model laser sources. If the distances r_1 and r_2 from one of these point sources to each of the slits differ by less than half the wavelength, then the spherical wavefront emanating from the point source should have complex amplitudes at the two slit positions which are strongly correlated. The same is true for every point within the extended source. The figure is drawn for the case which maximizes the difference $r_2 - r_1$, which is given by

$$r_2 - r_1 = \left[\left(\frac{\Delta x}{2} + \frac{d}{2}\right)^2 + L_1^2\right]^{\frac{1}{2}} - \left[\left(\frac{\Delta x}{2} - \frac{d}{2}\right)^2 + L_1^2\right]^{\frac{1}{2}} . \tag{1.17}$$

After some approximations, the requirement that this quantity be less than half the wavelength becomes

$$\Delta x < \frac{\lambda L_1}{d} \sim \xi_x \, . \tag{1.18}$$

Therefore, the spatial coherence length is seen to be proportional to the wavelength and inversely proportional to the angle subtended by the source when viewed from the plane containing the double slit.

A coherent x-ray beam therefore can be prepared by spatially filtering the beam from an incoherent source. If an aperture or a set of slits with an extent $\Delta x < \xi_x$ and $\Delta y < \xi_y$ is introduced into the beam, what passes can be treated as a coherent beam. Also, a sample with such a small extent, introduced into the full unfiltered beam, can be considered coherently illuminated. Conventional incoherent x-ray diffraction experiments have no strict requirements on spatial coherence, but for CXD it is critical. The coherence length of a typical synchrotron x-ray beam is much smaller than the beam itself, so that spatial filtering to produce a coherent beam requires cutting out a very large fraction of the beam. It is this effect which has precluded coherent x-ray experiments until the advent of high-brilliance synchrotron sources;

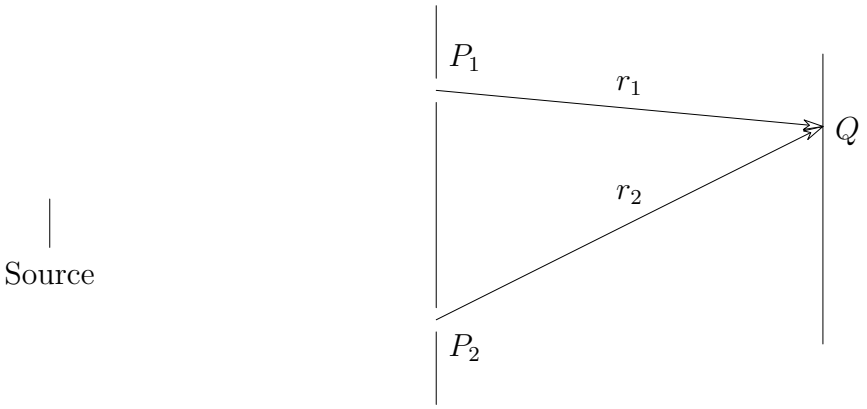

Figure 1.4: A partially coherent interference experiment. Two pinholes at P_1 and P_2 act as secondary sources interfering at the observation point Q.

even now, it is often experimentally expedient to make measurements using apertures which are of the same order in size as the spatial coherence lengths of the beam. As a result, the beam is best described as partially coherent.

1.2.2 The Complex Degree of Coherence and the Interference of Partially Coherent Sources

A more precise decription for spatial coherence of a beam involves the complex degree of coherence. Consider the double slit experiment shown in Fig. 1.4. If the pinholes at P_1 and P_2 are separated by a distance small compared with the spatial coherence length, a fringe pattern with high contrast will be seen on the screen; however, if the separation is large, then no interference will be seen. Instead, the incoherent sum of intensities from P_1 and P_2 will impinge on the screen. The degree to which the sources P_1 and P_2 interfere is determined by the complex degree of coherence, $\gamma_{12}(\tau)$, where

$$\tau = \frac{r_2 - r_1}{c} \tag{1.19}$$

is the difference in time-of-flight from the sources to Q.

The complex amplitude at Q at a time t is the sum of the contribution from each

source:

$$A(Q,t) = m_1 A(P_1, t - t_1) + m_2 A(P_2, t - t_2)\,, \tag{1.20}$$

where m_1 and m_2 are constants, which have a magnitude which depends on the size of the pinholes, the distances r_1 and r_2, and the angles by which the beam bends at P_1 and P_2, and are pure imaginary in phase, reflecting the phase shift for secondary wavelets [11]. The times t_1 and t_2 are the times-of-flight from P_1 and P_2 to Q. A measurement will record the time-averaged intensity at a point, which at Q will have the value

$$\begin{aligned} I(Q) &= m_1 m_1^* \left\langle A_1(t - t_1) A_1^*(t - t_1) \right\rangle \\ &+ m_2 m_2^* \left\langle A_2(t - t_2) A_2^*(t - t_2) \right\rangle \\ &+ m_1 m_2^* \left\langle A_1(t - t_1) A_2^*(t - t_2) \right\rangle \\ &+ m_2 m_1^* \left\langle A_2(t - t_2) A_1^*(t - t_1) \right\rangle\,, \end{aligned} \tag{1.21}$$

where $A_1(t)$ and $A_2(t)$ are shorthand for $A(P_1, t)$ and $A(P_2, t)$, respectively, and the angle brackets indicate averaging over time. Let $I_1 = \langle A_1(t) A_1^*(t) \rangle$ and $I_2 = \langle A_2(t) A_2^*(t) \rangle$ give the intensity at each pinhole. By defining the mutual coherence function,

$$\Gamma_{12}(\tau) \equiv \left\langle A_1(t + \tau) A_2^*(t) \right\rangle\,, \tag{1.22}$$

the expression for the intensity simplifies to

$$I(Q) = |m_1|^2 I_1 + |m_2|^2 I_2 + 2\,|m_1 m_2|\,\Gamma_{12}^{(r)}(\tau)\,, \tag{1.23}$$

where $\Gamma_{12}^{(r)}$ indicates the real part of Γ_{12}. The normalized form of Γ_{12} is defined the complex degree of coherence:

$$\gamma_{12}(\tau) \equiv \frac{\Gamma_{12}(\tau)}{\sqrt{\Gamma_{11}(0)}\sqrt{\Gamma_{22}(0)}} = \frac{\Gamma_{12}(\tau)}{\sqrt{I_1}\sqrt{I_2}}\,. \tag{1.24}$$

Note that $|m_1|^2 I_1$ would be the intensity measured at Q if the pinhole at P_2 were covered, and that $|m_2|^2 I_2$ would be the intensity measured at Q if the pinhole at P_1

were covered. Let these be called $I^{(1)}(Q)$ and $I^{(2)}(Q)$, respectively. Now, the intensity at Q can be written

$$I(Q) = I^{(1)}(Q) + I^{(2)}(Q) + 2\sqrt{I^{(1)}(Q)}\sqrt{I^{(2)}(Q)}\gamma_{12}(\tau)\,. \tag{1.25}$$

It can be shown via the Schwarz inequality that $|\gamma_{12}(\tau)| \leq 1$. A further simplification can be obtained if one writes

$$\gamma_{12}(\tau) = |\gamma_{12}(\tau)|\, e^{i[\alpha_{12}(\tau) - ck_0\tau]}\,, \tag{1.26}$$

where k_0 represents the mean wavenumber in the quasi-monochromatic light source and

$$\alpha_{12}(\tau) \equiv ck_0\tau + \arg\gamma_{12}(\tau)\,. \tag{1.27}$$

Then the intensity at Q becomes

$$I(Q) = I^{(1)}(Q) + I^{(2)}(Q) + 2\sqrt{I^{(1)}(Q)}\sqrt{I^{(2)}(Q)}\,|\gamma_{12}(\tau)|\cos\left[\alpha_{12}(\tau) - ck_0\tau\right]\,. \tag{1.28}$$

From this expression, it can be seen that the intensity at Q can be described as the sum of two contributions: one from the coherent addition of two beams with intensities $|\gamma_{12}(\tau)|\, I^{(1)}(Q)$ and $|\gamma_{12}(\tau)|\, I^{(2)}(Q)$ with a relative phase difference $\alpha_{12}(\tau) - ck_0\tau$, and the other from the incoherent addition of two beams of intensity $[1 - |\gamma_{12}(\tau)|]\, I^{(1)}(Q)$ and $[1 - |\gamma_{12}(\tau)|]\, I^{(2)}(Q)$. Evidently, $\alpha_{12}(\tau)$ represents the relative phase difference of the two secondary sources at P_1 and P_2 themselves, since $ck_0\tau$ expresses the phase difference of the two beams arriving at Q due to the difference in their time-of-flight.

In the usual case of sufficient temporal coherence, $\tau \ll \frac{\xi_\parallel}{c}$, then $\Gamma_{12}(\tau)$, $\gamma_{12}(\tau)$ and $\alpha_{12}(\tau)$ should be slowly varying functions with respect to τ. Let these be approximated by the following:

$$\begin{aligned} J_{12} &= \Gamma_{12}(0) = \langle A_1(t) A_2^*(t)\rangle\,, \\ \mu_{12} &= \gamma_{12}(0) = \tfrac{J_{12}}{\sqrt{I_1}\sqrt{I_2}}\,, \text{ and} \\ \beta_{12} &= \alpha_{12}(0) = \arg\mu_{12}\,. \end{aligned} \tag{1.29}$$

Even though μ_{12} represents only a special case of $\gamma_{12}(\tau)$, the two are often used interchangeably, since $\xi_{\|}$ is typically sufficiently large. The spatial coherence of an extended source, measured at some plane a distance L_1 away, is characterized by J_{12} and μ_{12} for pairs of points on the plane. The calculation of the latter is facilitated by the van Cittert-Zernike theorem [13; 14].

1.2.3 The van Cittert-Zernike Theorem

Given a source distribution on a plane parallel to and a distance L_1 away from the observation plane, the van Cittert-Zernike theorem provides a means for calculating the complex degree of coherence, μ_{12}, for two points $\mathbf{r}'_1$ and $\mathbf{r}'_2$ in the observation plane. In this section, points within the source plane will be described with unprimed vectors $\mathbf{r}$ relative to the origin in the source plane, O, while points within the observation plane will be described with primed vectors $\mathbf{r}'$ relative to the origin in the observation plane, O'. The magnitudes of $\mathbf{r}$ and $\mathbf{r}'$ in the following discussion will be assumed to be much smaller than the length L_1.

Take the source to consist of small, independently radiating elements, each with intensity $I(\mathbf{r})d^2r$, where $I(\mathbf{r})$ indicates the intensity per unit area of the source at $\mathbf{r}$. If the complex amplitude at $\mathbf{r}'_1$ and at $\mathbf{r}'_2$ due to the mth source element are denoted $A_{m1}(t)$ and $A_{m2}(t)$, the total complex amplitudes at these points are

$$A_1(t) = \sum_m A_{m1}(t)\,, \text{ and } A_2(t) = \sum_m A_{m2}(t)\,. \tag{1.30}$$

As a result,

$$J(\mathbf{r}'_1, \mathbf{r}'_2) = \langle A_1(t)A_2^*(t)\rangle = \sum_m \langle A_{m1}(t)A_{m2}^*(t)\rangle + \sum_m \sum_{n\neq m} \langle A_{m1}(t)A_{n2}^*(t)\rangle\ . \tag{1.31}$$

Since the source elements are statistically independent and have zero-mean amplitudes, the cross terms comprising the second term all equal zero. If the complex amplitude of the source element m at $\mathbf{r}_m$ is $A_m^{(s)}(t)$ and the distance from that source

element to an observation screen point $\mathbf{r}'_1$ or $\mathbf{r}'_2$ is l_{m1} or l_{m2}, then

$$\begin{aligned} A_{m1}(t) &= A_m^{(s)}\left(t - \frac{l_{m1}}{c}\right)\frac{e^{-ick_0\left(t-\frac{l_{m1}}{c}\right)}}{l_{m1}}\,, \text{ and} \\ A_{m2}(t) &= A_m^{(s)}\left(t - \frac{l_{m2}}{c}\right)\frac{e^{-ick_0\left(t-\frac{l_{m2}}{c}\right)}}{l_{m2}}\,, \end{aligned} \tag{1.32}$$

where, again, $k_0 = 2\pi/\lambda_0$ is the mean wavenumber of the source. Hence

$$\begin{aligned} J(\mathbf{r}'_1, \mathbf{r}'_2) &= \sum_m \left\langle A_m^{(s)}\left(t - \frac{l_{m1}}{c}\right) A_m^{(s)*}\left(t - \frac{l_{m2}}{c}\right)\right\rangle \frac{e^{ik_0(l_{m2}-l_{m1})}}{l_{m1}l_{m2}} \\ &= \sum_m \left\langle A_m^{(s)}(t)\, A_m^{(s)*}\left(t - \frac{l_{m2}-l_{m1}}{c}\right)\right\rangle \frac{e^{ik_0(l_{m2}-l_{m1})}}{l_{m1}l_{m2}} \end{aligned} \tag{1.33}$$

If the light is sufficiently monochromatic such that $l_{m2} - l_{m1} \ll \xi_\parallel$, then the time delay due to the difference in time-of-flight does not alter the time average above for each of the m sources, so that

$$\begin{aligned} J(\mathbf{r}'_1, \mathbf{r}'_2) &= \sum_m \left\langle A_m^{(s)}(t)\, A_m^{(s)*}(t)\right\rangle \frac{e^{ik_0(l_{m2}-l_{m1})}}{l_{m1}l_{m2}} \\ &= \int I(\mathbf{r})\frac{e^{ik_0(l_2-l_1)}}{l_1 l_2} d^2r\,, \end{aligned} \tag{1.34}$$

where l_1 and l_2 are the distances from the source point $\mathbf{r}$ to the points $\mathbf{r}'_1$ and $\mathbf{r}'_2$, respectively. By Eqn. 1.29, the complex degree of coherence is then

$$\mu_{12} = \mu(\mathbf{r}'_1, \mathbf{r}'_2) = \frac{1}{\sqrt{I(\mathbf{r}'_1)}\sqrt{I(\mathbf{r}'_2)}} \int I(\mathbf{r})\frac{e^{ik_0(l_2-l_1)}}{l_1 l_2} d^2r\,, \tag{1.35}$$

where

$$I(\mathbf{r}'_1) = J(\mathbf{r}'_1, \mathbf{r}'_1) \text{ and } I(\mathbf{r}'_2) = J(\mathbf{r}'_2, \mathbf{r}'_2) \tag{1.36}$$

are the intensities at $\mathbf{r}'_1$ and $\mathbf{r}'_2$. Note that the integral appearing in Equation 1.35 is the same as the integral over Huygens wavelets which would occur in computing the diffraction pattern of a spherical wave converging on the screen, after being passed through an aperture imposing the same intensity distribution $I(\mathbf{r})$. The equivalence of the functional forms for these two calculations is referred to as the van Cittert-Zernike theorem. The expression for $\mu(\mathbf{r}'_1, \mathbf{r}'_2)$ can be simplified further by replacing

l_1 and l_2 by L_1 in the denominator of the integrands. For other occurrences of l_1 and l_2, since

$$l_1^2 = |\mathbf{r}_1' - \mathbf{r}|^2 + L_1^2 \,, \tag{1.37}$$

the approximation can be made that

$$l_1 \approx L_1 + \frac{|\mathbf{r}_1' - \mathbf{r}|^2}{2L_1} \,, \tag{1.38}$$

with an analogous approximation for l_2. Accordingly, the difference $l_1 - l_2$ can be approximated by the expression

$$l_1 - l_2 \approx \frac{|\mathbf{r}_1'|^2 - |\mathbf{r}_2'|^2}{2L_1} - \frac{(\mathbf{r}_1' - \mathbf{r}_2') \cdot \mathbf{r}}{L_1} \,. \tag{1.39}$$

With the definitions

$$\mathbf{q} \equiv k_0 \frac{(\mathbf{r}_1' - \mathbf{r}_2')}{L_1} \tag{1.40}$$

and

$$\psi \equiv k_0 \frac{|\mathbf{r}_1'|^2 - |\mathbf{r}_2'|^2}{2L_1} \,, \tag{1.41}$$

Equation 1.35 takes the convenient form

$$\mu(\mathbf{r}_1', \mathbf{r}_2') = \frac{e^{i\psi} \int I(\mathbf{r}) e^{i\mathbf{q}\cdot\mathbf{r}} d^2r}{\int I(\mathbf{r}) d^2r} \,. \tag{1.42}$$

The result is that the degree of coherence between two points, in the far field relative to the source, is the normalized Fourier transform of the intensity distribution of the source itself.

Synchrotron sources can be modelled by a Gaussian distribution of intensity with a size determined by the distribution of the particle orbit. Hence, if a synchrotron orbit yields a source size with sigma widths σ_x, σ_y, then the complex degree of coherence will be Gaussian at the experiment with sigma widths

$$\sigma_{\mu_x} = \frac{\lambda L_1}{2\pi\sigma_x} \,, \quad \sigma_{\mu_y} = \frac{\lambda L_1}{2\pi\sigma_y} \,, \tag{1.43}$$

where λ is the x-ray wavelength and L_1 is the distance from the source to the experiment. Thus, at the experiment, the beam can be treated as coherent after being passed through an aperture measuring less than $\sigma_x^{(x)}\sqrt{\pi} \times \sigma_y^{(y)}\sqrt{\pi}$ [15]. Note that this is simply a criterion based on an integration across the complex degree of coherence and represents what is thought to be an acceptable fraction of incoherent contribution to the beam. Effectively, then, the spatial coherence lengths of a Gaussian-profile source a distance L_1 away are

$$\xi_x = \frac{\lambda L_1}{2\sigma_x\sqrt{\pi}} \quad \xi_y = \frac{\lambda L_1}{2\sigma_y\sqrt{\pi}}\,. \tag{1.44}$$

Note that this has the same form as that of the qualitative result of Equation 1.18, but with an effective source size $d = 2\sigma_y\sqrt{\pi}$.

1.3 Cu_3Au

Binary alloys such as Cu_3Au have been a classical system for x-ray diffraction study for at least 60 years. The reasons Cu_3Au has been productive for x-ray experiments are that it consists of strongly scattering elements, which facilitates x-ray measurement; it is robust with respect to beam damage; and it has a conveniently accessible phase transition temperature $T_c = 390°C$, near which diffusion takes place on a suitable time scale for experiments. Several review articles [16–18] have addressed (incoherent) x-ray diffraction from binary alloys, as have chapters in Warren [8] and in Guinier [19]. More recently, investigators have studied the dynamics of Cu_3Au with x-ray diffraction. Some articles have reported on the phase transition in the surface layers of Cu_3Au [20–23], while others concerned the nonequilibrium dynamics of Cu_3Au after a quench from above T_c [22; 24–29]. The long-range ordering below T_c gives rise to antiphase domains, which are of interest for the CXD study detailed in this thesis.

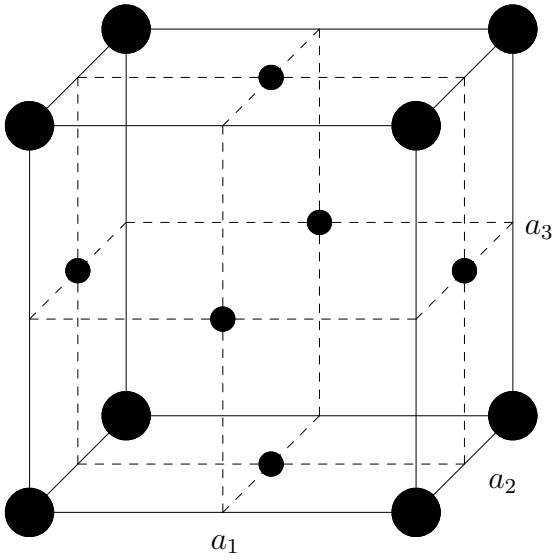

Figure 1.5: Unit cell of Cu_3Au. Small circles indicate the α-sites, while large circles indicate the β-sites. In perfectly ordered Cu_3Au, the copper atoms occupy only the α-sites, and the gold atoms occupy only the β-sites.

1.3.1 Crystalline Structure and Antiphase Domains

Cu_3Au has a face-centered cubic structure, like that of gold or copper, as shown in Figure 1.5. In a perfectly ordered crystal, the copper atoms occupy the face sites and the gold atoms occupy the corner sites in the unit cell. These sites will be referred to as α-sites and β-sites, respectively. The resulting structure consists of alternating planes along the principal axis directions which are either half-copper and half-gold or all-copper. If the temperature of a perfectly ordered crystal is raised, some of the sites will become occupied by the wrong atom. The long-range order of the system vanishes at the critical temperature $T_c = 390°C$. Above T_c, the presence of one kind of atom in a particular site only influences the occupancy of the nearest-neighbor sites.

As a Cu_3Au sample is annealed below the critical temperature, a nucleation and growth of domains having a consistent stacking sequence occurs; these domains are referred to as antiphase domains. The boundary between two antiphase domains can be constructed in two ways in a plane perpendicular to a principal axis of the

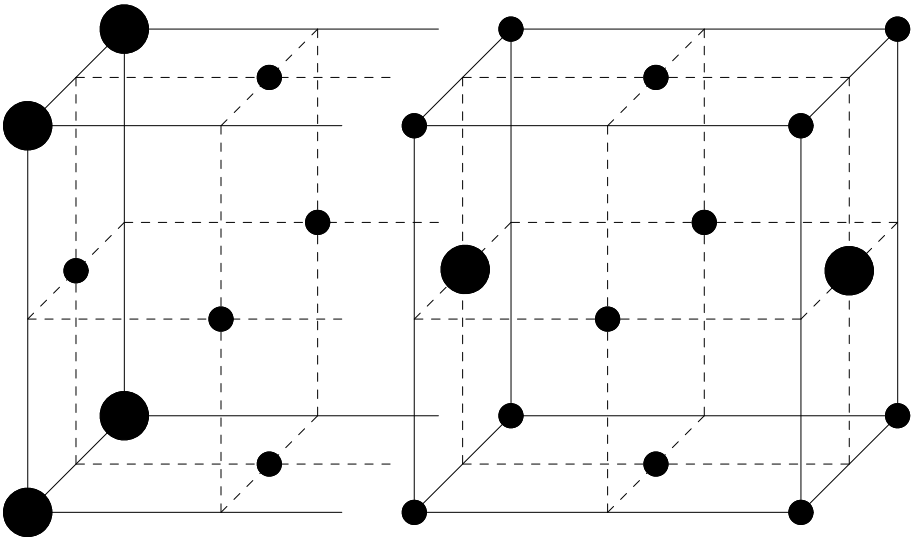

Figure 1.6: Type I domain wall in Cu_3Au. With the axis running to the right denoted $\mathbf{a}_1$, the domain wall consists of a glide plane in the $\frac{1}{2}(\mathbf{a}_2 + \mathbf{a}_3)$ direction.

crystal. A Type I domain wall in a plane perpendicular to a given principal axis, say $\mathbf{a}_1$, consists of a half-diagonal glide in the $\frac{1}{2}(\mathbf{a}_2 + \mathbf{a}_3)$-direction or symmetry equivalent. See Figure 1.6. Type I domain walls do not alter the local nearest-neighbor environment for any of the atoms, and hence have a low energy associated with their formation. A Type II domain wall in a plane perpendicular to $\mathbf{a}_1$ consists of a translation of the lattice by $\frac{1}{2}(\mathbf{a}_1 + \mathbf{a}_2)$ or symmetry equivalent. See Figure 1.7. Type II domain walls do alter the local nearest-neighbor configuration of the atoms, and so they represent a higher energy than Type I domain walls. The domain walls can be imaged using dark-field TEM as shown in Figure 1.8 for the case of a ~ 500 Å thick Cu_3Au film [30].

The structure factor, F, of Cu_3Au can be seen to depend on the long-range order. The evaluation of the structure factor presented in Warren [8] introduces the four

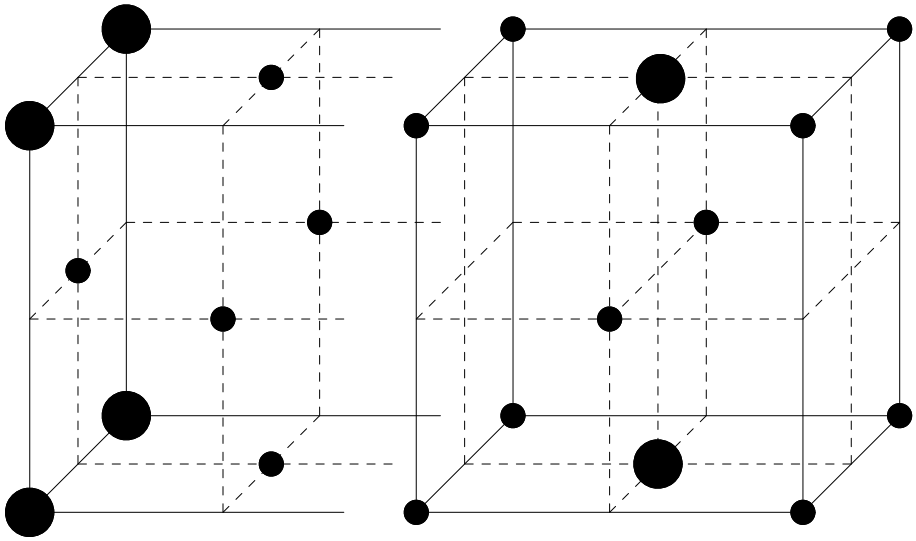

Figure 1.7: Type II domain wall in Cu_3Au. With the axis running to the right denoted $\mathbf{a}_1$, the domain wall consists of a glide plane in the $\frac{1}{2}(\mathbf{a}_1 + \mathbf{a}_2)$ direction. The domain wall here forms a copper-rich region; forming the domain wall to the right of the middle plane instead would form a gold-rich region.

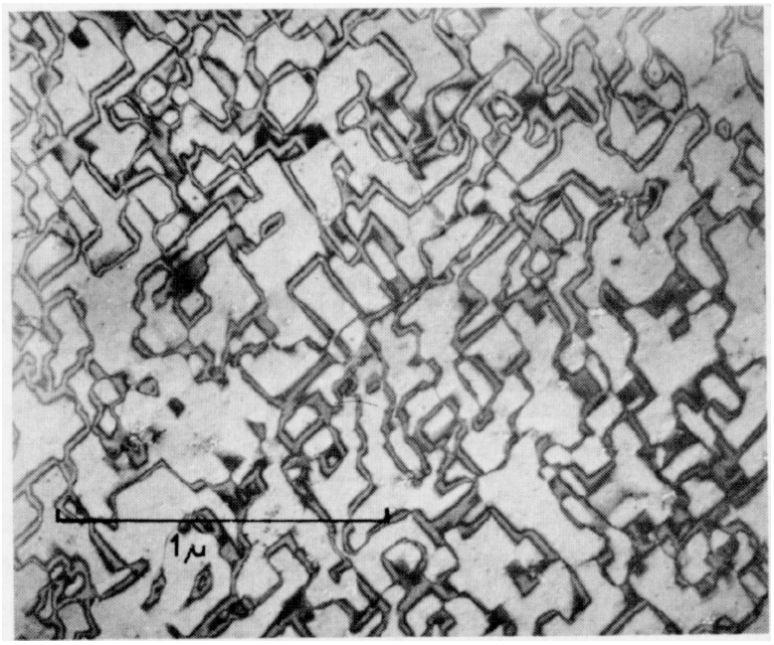

Figure 1.8: Dark-field TEM image of Cu_3Au antiphase domain boundaries. From Reference [30].

parameters, with "r" denoting "right" and "w" denotiong "wrong,"

$$\begin{aligned} r_\alpha &\equiv \text{ fraction of } \alpha\text{-sites occupied by a Cu atom,} \\ w_\alpha &\equiv \text{ fraction of } \alpha\text{-sites occupied by a Au atom,} \\ r_\beta &\equiv \text{ fraction of } \beta\text{-sites occupied by a Au atom, and} \\ w_\beta &\equiv \text{ fraction of } \beta\text{-sites occupied by a Cu atom.} \end{aligned} \tag{1.45}$$

From these definitions, along with the assumption of a stoichiometric ratio of copper to gold, it is clear that

$$\frac{3}{4}r_\alpha + \frac{1}{4}w_\beta = \frac{3}{4}, \text{ and} \quad \frac{3}{4}r_\beta + \frac{1}{4}w_\alpha = \frac{1}{4}\,, \tag{1.46}$$

since there are three α-sites for each β-site. The Bragg and Williams long-range order parameter S is defined

$$S \equiv r_\alpha + r_\beta - 1\,, \tag{1.47}$$

so that $S = 0$ for a completely random arrangement and $S = 1$ for a completely ordered arrangement. Later, in the discussion of antiphase domains, we will take $S = 1$ to indicate complete ordering within each antiphase domain separately.

Using the average scattering factor for each lattice site in the unit cell, the structure factor can be written in terms of a sum over the α-sites and a sum over the β-sites:

$$\begin{aligned} F = &\sum_\alpha (r_\alpha f_{\mathrm{Cu}} + w_\alpha f_{\mathrm{Au}}) e^{2\pi i(hx_n + ky_n + lz_n)} \\ &+ \sum_\beta (r_\beta f_{\mathrm{Au}} + w_\beta f_{\mathrm{Cu}}) e^{2\pi i(hx_n + ky_n + lz_n)}\,. \end{aligned} \tag{1.48}$$

Here, (x_n, y_n, z_n) describes the position of the nth site in the summation. The α-sites are located at $\frac{1}{2}\frac{1}{2}0$, $\frac{1}{2}0\frac{1}{2}$, and $0\frac{1}{2}\frac{1}{2}$, while the β-sites are at 000. This leads to the following expression for the structure factor:

$$F = (r_\alpha f_{\mathrm{Cu}} + w_\alpha f_{\mathrm{Au}}) \left[e^{\pi i(h+k)} + e^{\pi i(h+l)} + e^{\pi i(k+l)}\right] + (r_\beta f_{\mathrm{Au}} + w_\beta f_{\mathrm{Cu}})\,. \tag{1.49}$$

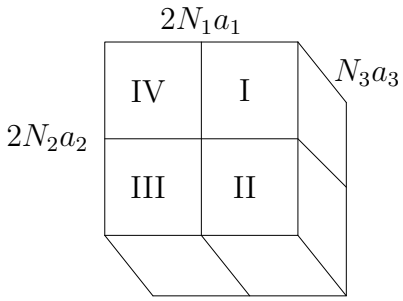

Figure 1.9: Block of Cu_3Au containing four antiphase domains. Two Type I boundaries cut the block into the antiphase domains I, II, III, and IV.

In the case of hkl all-even or all-odd, the structure factor reduces to

$$F = \frac{3}{4} f_{\mathrm{Cu}} + \frac{1}{4} f_{\mathrm{Au}} \,, \tag{1.50}$$

while for mixed even and odd hkl, the structure factor becomes proportional to S:

$$F = S(f_{\mathrm{Au}} - f_{\mathrm{Cu}}) \,. \tag{1.51}$$

The two types of reflections are referred to as fundamental and superstructure, respectively. The long-range ordering within a sample has been measured via the ratio of the strength of a fundamental reflection to that of a superstructure reflection [31].

1.3.2 Reciprocal-Space Structure

The reciprocal-space structure, which describes the complex amplitude of scattering as a function of $\mathbf{q}$, is determined by the system of antiphase domains present in the illuminated volume of a sample. As an illustrative example, we consider an illuminated volume of Cu_3Au measuring $2N_1a_1 \times 2N_2a_2 \times N_3a_3$ and containing two Type I antiphase domain boundaries, in the planes perpendicular to $\mathbf{a}_1$ and $\mathbf{a}_2$. For Cu_3Au, $a_1 = a_2 = a_3 \approx 3.73$ Å. Let the planes cut the block into four equal parts, each of dimensions $N_1a_1 \times N_2a_2 \times N_3a_3$. See Figure 1.9. If the lattice of domain I is considered to have no displacement with the Au atoms at the corners of the unit cell, then the lattice in each of the remaining three domains has the following

displacement:

$$\begin{aligned} \text{II} \quad & \tfrac{1}{2}(\mathbf{a}_1 + \mathbf{a}_3) \\ \text{III} \quad & \tfrac{1}{2}(\mathbf{a}_1 + \mathbf{a}_2) \\ \text{IV} \quad & \tfrac{1}{2}(\mathbf{a}_2 + \mathbf{a}_3)\,. \end{aligned} \tag{1.52}$$

Since $S = 1$ in each of the domains individually, the structure factor for each one has the same magnitude according to Equation 1.49. However, the phase of the structure factor is different for each of the domains. In the region of reciprocal space near the (hkl) reflection, denoted by

$$\begin{aligned} \mathbf{q} &= q_1\mathbf{b}_1 + q_2\mathbf{b}_2 + q_3\mathbf{b}_3 \\ &= (h+\delta h)\mathbf{b}_1 + (k+\delta k)\mathbf{b}_2 + (l+\delta l)\mathbf{b}_3\,, \end{aligned} \tag{1.53}$$

where h, k, and l have integer values, the structure factor for domain I is

$$F_I = f_{\text{Au}} + f_{\text{Cu}}\left[e^{i\pi(q_1+q_2)} + e^{i\pi(q_2+q_3)} + e^{i\pi(q_1+q_3)}\right]\,. \tag{1.54}$$

Because of the shifts in the lattice, the structure factors for the remaining domains are given by

$$\begin{aligned} F_{II} &= F_I e^{\pi i(q_1+q_3)} \\ F_{III} &= F_I e^{\pi i(q_1+q_2)} \\ F_{IV} &= F_I e^{\pi i(q_2+q_3)}\,. \end{aligned} \tag{1.55}$$

Hence, at the (100) reflection, $F_I = F_{IV} = -F_{II} = -F_{III}$, and domains I and IV are in contrast with domains II and III. At the (101) reflection, however, $F_I = F_{II} = -F_{III} = -F_{IV}$, so that domains I and II are in contrast with domains III and IV. The complex amplitude of scattering, or reciprocal space structure, of the whole block is

$$\begin{aligned} A = F_I &\left\{\sum_{m_1=0}^{N_1-1} e^{2\pi i q_1 m_1} + e^{\pi i(q_2+q_3)} \sum_{m_1=N_1}^{2N_1-1} e^{2\pi i q_1 m_1}\right\} \times \\ &\left\{\sum_{m_2=0}^{N_2-1} e^{2\pi i q_2 m_2} + e^{\pi i(q_1+q_3)} \sum_{m_2=N_2}^{2N_2-1} e^{2\pi i q_2 m_2}\right\} \sum_{m_3=0}^{N_2-1} e^{2\pi i q_2 m_2}\,. \end{aligned} \tag{1.56}$$

An experiment measures the intensity:

$$\begin{aligned} I =& I_0 F_I F_I^* \frac{\sin^2 \pi q_1 N_1}{\sin^2 \pi q_1} \frac{\sin^2 \pi q_2 N_2}{\sin^2 \pi q_2} \frac{\sin^2 \pi q_3 N_3}{\sin^2 \pi q_3} \times \\ & \left[1 + e^{\pi i (q_2 + q_3 + 2N_1 q_1)}\right] \left[1 + e^{-\pi i (q_2 + q_3 + 2N_1 q_1)}\right] \times \\ & \left[1 + e^{\pi i (q_1 + q_3 + 2N_2 q_2)}\right] \left[1 + e^{-\pi i (q_1 + q_3 + 2N_2 q_2)}\right] . \end{aligned} \tag{1.57}$$

As long as δh, δk, and δl are small, the expression for the intensity can be approximated by

$$\begin{aligned} I =& I_0 F_I F_I^* \frac{\sin^2 \pi N_1 \delta h}{(\pi \delta h)^2} \frac{\sin^2 \pi N_2 \delta k}{(\pi \delta k)^2} \frac{\sin^2 \pi N_3 \delta l}{(\pi \delta l)^2} \times \\ & 4 \left[1 + (-1)^{k+l} \cos 2\pi N_1 \delta h\right] \left[1 + (-1)^{h+l} \cos 2\pi N_2 \delta k\right] . \end{aligned} \tag{1.58}$$

In the case of $k + l$ even, the intensity can be written

$$I = I_0 F F^* \frac{\sin^2 \pi 2N_1 \delta h}{(\pi \delta h)^2} \frac{\sin^2 \pi N_2 \delta k}{(\pi \delta k)^2} \frac{\sin^2 \pi N_3 \delta l}{(\pi \delta l)^2} \left[1 + (-1)^{h+l} \cos 2\pi N_2 \delta k\right] . \tag{1.59}$$

Now, if $h + l$ is also even, which is the case of a fundamental reflection and occurs only if h, k, and l are all-even or all-odd, the intensity is

$$I = I_0 F F^* \frac{\sin^2 \pi 2N_1 \delta h}{(\pi \delta h)^2} \frac{\sin^2 \pi 2N_2 \delta k}{(\pi \delta k)^2} \frac{\sin^2 \pi N_3 \delta l}{(\pi \delta l)^2} . \tag{1.60}$$

Note that this is the expression for the intensity which would be expected if there were no antiphase domain boundaries at all. So, it is seen that the fundamental Bragg reflections are insensitive to the presence of antiphase domains. However, if $h + l$ is odd, the intensity is

$$I = I_0 F F^* \sin^2 \pi N_2 \delta k \frac{\sin^2 \pi 2N_1 \delta h}{(\pi \delta h)^2} \frac{\sin^2 \pi N_2 \delta k}{(\pi \delta k)^2} \frac{\sin^2 \pi N_3 \delta l}{(\pi \delta l)^2} , \tag{1.61}$$

which has the same form as that of a fundamental reflection, but which is twice as broad in the δk-direction and modulated in the δk-direction. The analogous result for the case of $k + l$ odd and $h + l$ even has the same behavior along the δh-direction, while the case of both $k + l$ and $h + l$ odd has broadening and modulation along both the δh- and δk-directions.

It is shown in Warren [8] that the presence of antiphase domain boundaries in an otherwise perfectly ordered specimen does not affect the integrated intensity of a superstructure reflection. In the limit of many antiphase domain boundaries, however, the lattice begins to resemble one which lacks long-range ordering completely, with $S = 0$, such that the structure factor, and hence the integrated intensity, goes to zero.

A real Cu_3Au specimen is likely to have a complex system of antiphase domains, like that shown in Figure 1.8, with chiefly Type I domain walls. The orientation of the domain walls is only weakly crystallographic on a scale larger than the unit cell, and on a fine scale, all three crystallographic orientations of Type I domain walls are expected to be found in equal numbers. All superstructure reflections have two indices of equal parity and one of the other parity. The directions corresponding to the two indices of equal parity are those in which the superstructure Bragg reflection is broadened, giving each superstructure peak a disk shape. The presence of a small number of Type II domain walls, however, will broaden the reflections in the flattened direction, yielding an oblate-spheroidal shape. The predicted disk-shaped superstructure Bragg reflections have been observed by x-ray diffraction on Cu_3Au crystals with minimal annealing [32; 33]. The modulations to the Bragg peaks due to the antiphase domains would not be expected to be observed in those experiments, for the following two reasons: the modulations occur on an extremely small scale in reciprocal space, and the incoherent addition of signals arising from an illuminated volume far exceeding the spatial coherence length of the beam would cause the modulations to wash out. Under coherent illumination, however, the modulations are visible if measured with high enough reciprocal-space resolution, and the intensity seen is the squared modulus of the Fourier transform of the antiphase domain structure. The goal of this thesis is to measure that intensity by CXD and to reconstruct the real-space arrangement of antiphase domains via computational methods. A simple inverse Fourier transform is insufficient, because in a measurement, the phase of the scattering amplitude is lost.

1.3.3 Sample Preparation

The Cu_3Au sample we used for our measurements was grown by molecular beam epitaxy (MBE) by the group of C. P. Flynn. The substrate was $(11\overline{2}0)$-oriented sapphire (Al_2O_3). Before loading into the MBE chamber, the sample was degreased with TCE, acetone, and ethanol. Then, it was annealed in UHV at 1050°C for two hours, with a base pressure of 8×10^{-10} Torr. Next, a $500 - 1000$Å buffer layer of niobium is grown at 900°C and about 0.2 Å/s. The niobium takes a (110) orientation under these conditions. Pure copper and pure gold are codeposited at a fixed ratio at 330°C to a thickness of about 1000 Å. The Cu_3Au grows in a (111) orientation. The temperature is then increased to 450°C to anneal away any composition gradients in the sample. Finally, the temperature was maintained for eight hours at 360°C, the temperature for which bulk ordering is fastest, and at 300°C for 48 hours [34].

Chapter 2

Experimental Methods

2.1 Introduction

The experimental requirements for successful CXD measurements are very specialized with respect to x-ray source, beam optics, and detection. Several technological advances made in the last decade have made CXD as described here possible. Insertion device beamlines at third generation synchrotrons provide the small source size, high brilliance, and high photon energy necessary to produce a usable coherent x-ray beam and to allow enough momentum transfer to reach Bragg reflections in typical crystals. Developed alongside such sources have been monochromators capable of providing sufficient temporal coherence while surviving the high heat loads involved. High-precision slits create the apertures of only a few micrometers, necessary for acheiving spatial coherence, have become available and convenient to use. Finally, charge-coupled device (CCD) area detectors, having a spatial resolution of less than 25 μm, can be purchased for use with x-rays from several vendors. Without each of these recent developments, CXD as presented here would not be feasible.

This chapter describes the experimental methods which we used to make the measurements of Chapter 3. The undulator, the monochromator, and the diffractometer all are part of the UNICAT beamline 33-ID.

2.2 The Advanced Photon Source Undulator A

The measurements described here were performed at the UNI-CAT beamline 33-ID at the Advanced Photon Source (APS) at Argonne National Laboratory. The insertion device is an undulator, and undulator radiation differs from that of a bending magnet or a wiggler in a fundamental way [35]. For a highly relativistic charged particle, i.e., with $\gamma \gg 1$, radiation is emitted in a cone about the path of the particle with an angular width of order $1/\gamma$. A single bending magnet will cause a beam of x-rays to be radiated from all points in the bend, producing a fan of radiation.

A wiggler causes the particle beam to be deflected multiple times along a straight path, but in such a way that the direction of the particle beam ψ_0 changes by an angle $\Delta\theta$ which is larger than the angular width of the cone of radiation. The resulting beam produced along a straight line consists of a series of flashes with a frequency $c/\lambda_0 \sim 10$ GHz, where λ_0 represents the period of the magnets in the wiggler. A scaled angle parameter K, is often used to describe a synchrotron insertion device, and is defined

$$K \equiv \gamma\psi_0 \,. \tag{2.1}$$

Thus, wigglers are typified by a large K. K can be computed for a given magnetic field in the insertion device, which can be varied by changing the gap between the poles of the magnets:

$$K = \frac{eB_0\lambda_0}{2\pi mc^2} \,. \tag{2.2}$$

The fundamental wavelength of the radiation emitted by a wiggler is

$$\lambda_f = \frac{\gamma\psi_0}{2\pi K} \,, \tag{2.3}$$

and the spectrum of x-rays produced by a wiggler has a broad shape similar to that of a bending magnet.

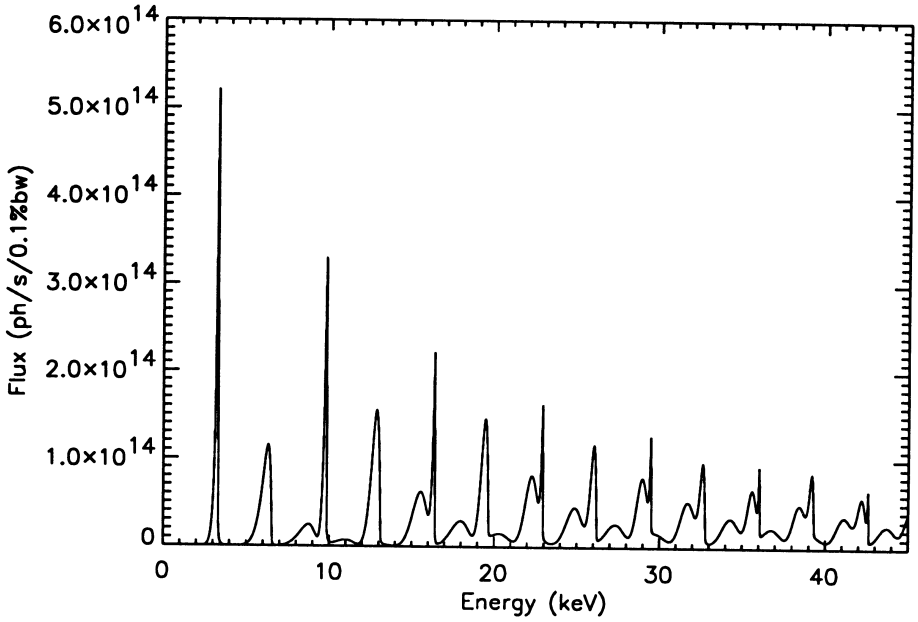

Figure 2.1: APS Undulator A spectrum. The natural APS Undulator A spectrum, as measured through a 2.5 mm×1.0 mm aperture at 30.0 m from the source is presented as shown in Ref. [36]. The curve is computed for the case of a closed gap (10.5 mm, $K_{\text{eff}} = 2.57$), which yields a fundamental energy of 3.25 keV.

Undulators are insertion devices for which $\psi_0 \approx \Delta\theta$. In that case, the cone of radiation is always directed such that the rest of the particle path is inside. For some wavelengths of radiation, a constructive interference is set up. The result is a natural undulator spectrum consisting of a series of relatively sharp peaks located at a fundamental energy and a series of harmonics, as shown in Figure 2.1. The fundamental of the energy spectrum has the wavelength

$$\lambda_f = \frac{2 + K^2 + 2\gamma^2\theta^2}{\gamma^2}\lambda_0\,, \tag{2.4}$$

where the angle θ is the angle off-axis. Here, it will always be the case that $\theta \ll \gamma^{-1}$, so the angular dependence of the beam energy will be ignored. The energy bandwidth of the fundamental is of order $1/N$, where N is the number of periods in the undulator. Often, the end poles are omitted to account for edge effects. The intensity of an undulator x-ray beam is proportional to N^2.

A more convenient figure of merit for undulator radiation output is the brilliance,

B, a measure of the photons emitted by a source per unit of time, per unit of bandwidth, per unit of source area, per unit of solid angle. It can be shown that the brilliance of a particular source is conserved by any focusing beam optics, since the product of the effective source area and the divergence of the source remains constant. Aberrations and absorption in the optics can decrease the brilliance. The total coherent flux of an x-ray source is related to B in a simple way. If the source has an area $d_x \times d_y$, then a distance L_1 away, the coherence lengths are $\xi_x = \lambda L_1/d_x$ and $\xi_y = \lambda L_1/d_y$. The angular acceptance of an aperture measuring $\xi_x \times \xi_y$ is then $\lambda/d_x \times \lambda/d_y$. Hence, the number of photons per unit time passing through the aperture, the coherent flux, is

$$F_{\text{coh}} = B d_x d_y \left(\frac{\lambda}{d_x}\right)\left(\frac{\lambda}{d_y}\right)\frac{\Delta E}{E} = B\lambda^2\frac{\Delta E}{E}\,. \tag{2.5}$$

The brilliance of the APS undulator A is stated to be about 2×10^{18} photons s^{-1} mm^{-2} mrad^{-2} per 0.1% bandwidth [36]. See Figure 2.2 for the dependence of B on the beam energy. Assuming the whole coherent flux could be collected, this would amount to 10^{10} photons/s, in the case of a Si(111) monochromator with $\frac{\Delta E}{E} = 2 \times 10^{-4}$ and a beam energy of 8.5 keV. For experiments with much lower requirements with respect to temporal coherence, the natural undulator beam with a $1/N \approx 2\%$ bandwidth can be used instead, with a gain of two orders of magnitude in coherent flux. Small-angle scattering and surface reflectivity are two examples of experiments which work well with the very short temporal coherence length of an unmonochromated undulator beam.

The source size of the APS storage ring, as described in Table 2.1, yields spatial coherence lengths $\xi_x \approx 5$ μm in the horizontal and $\xi_x \approx 37$ μm in the vertical, at a beam energy of 8.5 keV. Although not implemented for any of the work presented here, a focusing mirror could be used to vary the effective source size and, hence, the spatial coherence lengths. If, for example, a 2μm$\times 2\mu$m square aperture were convenient for the scale of structures of interest for a particular experiment, then

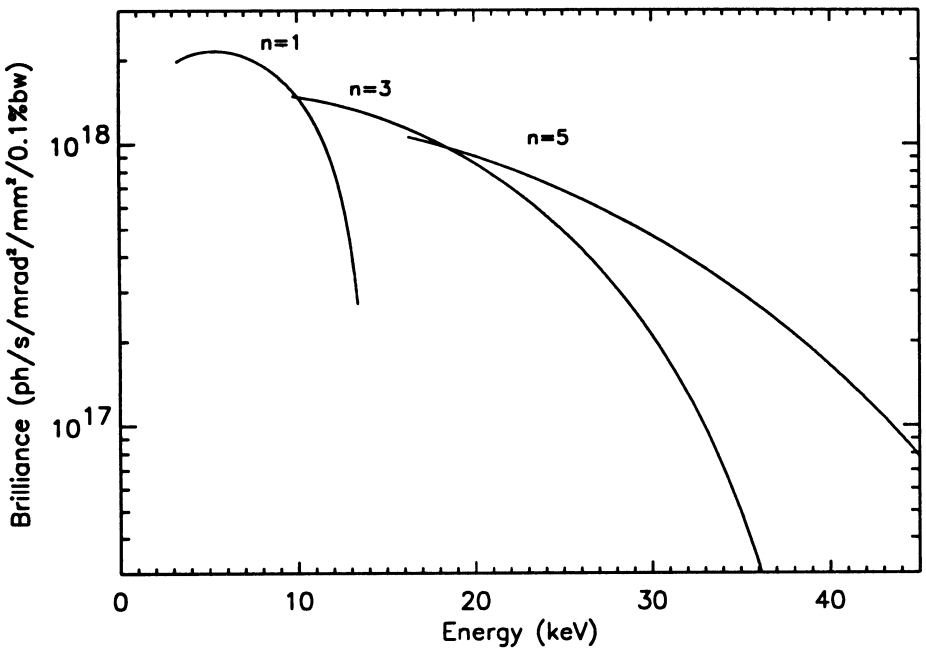

Figure 2.2: APS Undulator A brilliance. Shown are curves of B vs. beam energy for the first three odd-N harmonics of the APS Undulator A, assuming a 100 mA stored particle beam at 7 GeV, from Ref. [36].

coherence could be traded for intensity by demagnification of the source, for a gain of $\sim 45\times$ in photon flux.

2.3 Double-Crystal Si(111) Monochromator

We selected beam energy with a vertically deflecting double-crystal Si(111) monochromator. The bandwidth passed by such an optic can be analyzed in terms of the successive reflections from two nearly perfect thick crystals. The reflection of a divergent, polychromatic beam from a nearly perfect thick crystal is dispersive; by differentiating Bragg's law,

$$\lambda = 2d_{hkl} \sin \theta_B \,, \tag{2.6}$$

Table 2.1: APS and Undulator A parameters. Data taken from Ref. [36] and Ref. [37]. Parameters marked with * are evaluated at minimum gap setting.

Magnet material		Nd-Fe-B
Pole material		Vanadium permendur
Undulator period	λ_0	3.3 cm
Number of periods	N	72
Undulator length		2.4 m
Minimum gap*		10.5 mm
Deflection parameter*	K_{eff}	2.57
Peak deflection parameter*	K_{peak}	2.62
Maximum effective field*		0.835 T
Maximum peak field*		0.849 T
First harmonic energy*		3.2 keV
Horizontal source size	σ_x	≈ 350 μm
Vertical source size	σ_y	≈ 50 μm
Horizontal beam divergence	σ'_x	25 μrad
Vertical beam divergence	σ'_y	5 μrad
Distance to experiment station	L_1	40 m

Table 2.2: APS storage ring parameters. Data taken from Ref. [37].

Nominal energy	7.0 GeV
Nominal current	100 mA
Circumference	1104 m
Revolution time	3.683×10^{-6} s
Revolution frequency	271.5 kHz
Relativistic parameter γ	14,000

where θ_B is the "Bragg angle," or scattering angle, with respect to λ, we obtain the following:

$$\frac{\Delta\lambda}{\lambda} = \Delta\theta_B \cot\theta_B \,. \tag{2.7}$$

The range in exit angle, $\Delta\theta_B$, is the sum of two contributions. The first is the natural Darwin width of the reflecting crystal, ω_s, which depends on the Bragg angle, the wavelength, and the structure factor of the reflection [8]:

$$\omega_s = \frac{r_e N \lambda^2 \left|F\right|}{\pi \sin\theta_B} \,, \tag{2.8}$$

where N is the number of unit cells per unit volume. This relation is applicable for the case of a purely σ-polarized beam, as in the configuration of the beamline described here. Also, the Debye-Waller factor for the effect of temperature vibration, e^{-M}, has been neglected. That the Darwin width is nonzero should be expected on the grounds that by extinction and by absorption, only a finite thickness of the sample is illuminated. Since an infinite crystal is required for delta-function sharpness of reflections in reciprocal space, the finite illuminated thickness gives rise to a reflection with nonzero width. The second contribution to $\Delta\theta_B$ is from the beam divergence, in the vertical direction in this case. Since no focusing optics are present in the beam path leading from the source to the monochromator, the input divergence is simply $D_i = 2\sigma'_y$, and has the value 10 μrad for the APS Undulator A. The range of wavelengths passed by a single nearly perfect thick crystal is then

$$\frac{\Delta\lambda}{\lambda} = (\omega_s + D_i) \cot\theta_B \,. \tag{2.9}$$

The exit divergence of the single crystal is given by

$$D_e = D_i + \omega_s \left| 1 + \frac{\sin(\alpha + \theta_B)}{\sin(\alpha - \theta_B)} \right| \,, \tag{2.10}$$

where α is the angle between the Bragg planes of the reflection and the plane of the reflecting face of the crystal. For the Si(111) reflections in the monochromator in use, $\alpha = 0$, so that the output divergence is the same as the input divergence.

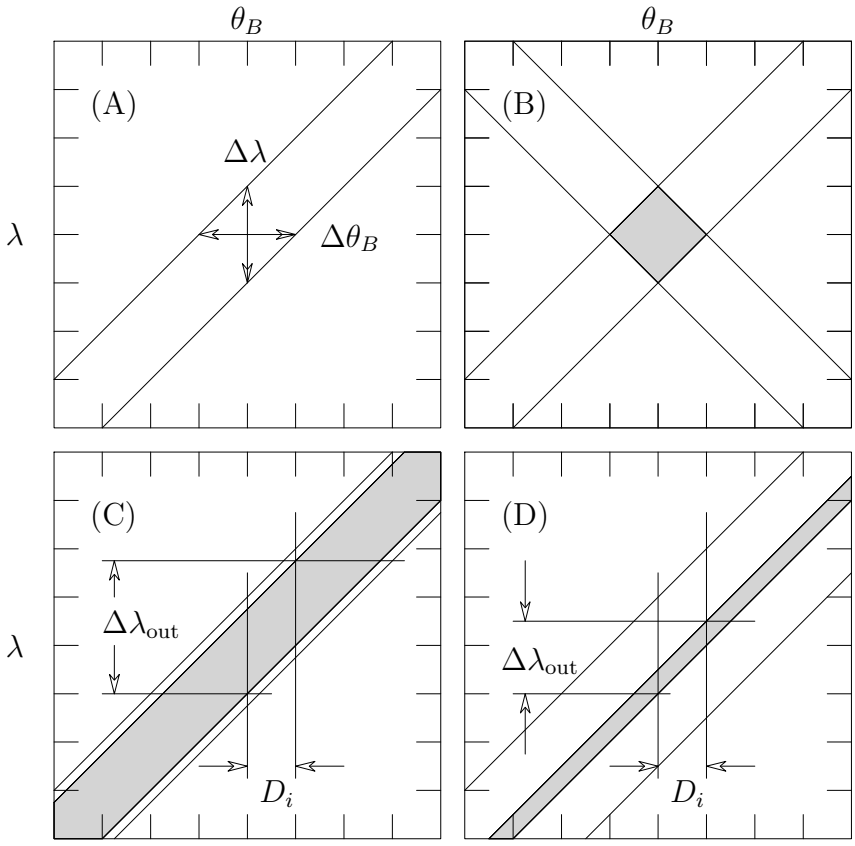

Figure 2.3: DuMond diagrams. (A) Single-crystal reflection for a colimated beam (vertical arrow) or for a monochromatic beam (horizontal arrow). (B) Double-crystal monochromator with both crystals scattering upward (or downward). (C) Double-crystal monochromator with crystals scattering in opposite directions and nearly parallel. (D) Double-crystal monochromator as in (C), but with differing scattering angles. Only a small region with a slope of $d_{hkl}\cos\theta_B$ is shown in each panel.

An illustrative construction which can be an aid for the analysis of single- and multiple-reflection monochromators was put forth by DuMond in a 1937 paper [38]. See Figure 2.3. The DuMond diagram for reflection from a single crystal consists of a plot of $\lambda = d_{hkl}\sin\theta_B$ and a plot of the same function displaced by the Darwin width, ω_s, along the θ_B-axis. The region between the two plots then describes the combinations of λ and θ_B which are reflected from the crystal. In panel (A) of Figure 2.3, the vertical arrow represents the reflection of a perfectly collimated beam, i.e. one having no spread in θ_B. The range of λ is then indicated by the length of the arrow. The horizontal arrow, however, represents the reflection of a monochromatic

beam with a divergence greater than the Darwin width of the crystal; it's reflected beam will of course remain monochromatic, but the beam will be spread with a divergence equal to the Darwin width. The radiation from the APS Undulator A has a divergence smaller than the Darwin width of typical monochromator crystals, so that the situation is best represented by the vertical arrow in panel (A) of Figure 2.3.

Panel (B) of Figure 2.3 shows the DuMond diagram drawn for a double-crystal monochromator arranged such that both crystals reflect in the same sense. The DuMond diagram for the first crystal is drawn just as in Panel (A), while the diagram for the second crystal is drawn with its θ_B-axis reversed and offset by the angle by which the orientations of the two crystals differ. The filled region of Panel (B) represents the set of scattering angles and wavelengths which are reflected by the two-crystal system. As the angular offset of the second crystal with respect to the first crystal is varied, the range of reflected wavelengths is shifted up and down, while the angular width of the reflection remains constant.

Panels (C) and (D) are DuMond diagrams drawn for the case of a double-crystal monochromator in which the second crystal scatters in the opposite sense as the first. In this case, the DuMond diagram for each crystal is drawn with θ_B-axis increasing to the right, and the offset is again equal to the difference in orientation of the two crystals. Panel (C) shows the case in which the two crystals are very nearly parallel. The reflected λ, θ_B combinations are nearly the same as those in the case of a single crystal monochromator; however, the reflecting power of the system is the product of the reflecting power of each crystal, so that the tails of the wavelength or angular distributions are suppressed. The key result is that, in the parallel case of Panel (C), the bandwidth passed by the two-crystal system is the same as that for a single-crystal monochromator. By orienting the second crystal in a direction differing from that of the first crystal by an angle less than the Darwin width, as shown in Panel (D), a somewhat smaller range of wavelength will be passed by the

monochromator. Of course, a smaller flux will be passed as well. As a result, a double-crystal monochromator in such an arrangement can be set to trade photon flux for a smaller bandwidth, such that the beam possesses a much sharper dependence of wavelength on angle than it does after a reflection from only one of the crystals. The beam can thus be used to measure the diffraction of a third crystal with very high precision.

The Darwin width of the Si(111) reflection used in the APS beamline monochromatar is sufficiently small for the measurements described here, and hence the second crystal of the monochromator was always oriented to maximize flux. The fine adjustment of the scattering angle of the second crystal relative to that of the first is done by a piezoelectric actuator. The motion of the actuator can be coupled to a beam intensity monitor downstream from the monochromator in a feedback loop. The reason for such a design is that, after the white-beam shutter has been closed for a time, such as during a fill of the ring, the crystals cool considerably and their orientation changes as a result of thermal distortion. The control system driving the feedback loop updates in intervals of less than a second, and can be set to hold a constant intensity level or to seek the peak intensity level.

Asymmetrically cut crystals have been explored for use as optical elements for preparing a beam with a small effective source size [39]. Since reflection from a set of Bragg planes inclined from the reflecting surface a crystal can spatially compress the beam, such an asymmetrically cut crystal would make it possible to create a smaller effective source size. However, it was shown via DuMond diagrams and demonstrated experimentally that a kind of chromatic aberration is inherent in such systems, and as a result, the divergence of the beam is much increased, discouraging the use of such crystals as optical elements for preparing coherent x-ray beams.

2.4 Roller Blade Slits

The construction of an aperture with openings on the 1 μm to 5 μm scale and with the necessary properties for producing a coherent beam of hard x-rays, i.e., with beam energy higher than about 6 keV, poses several difficulties. First, the requirement that the aperture material be opaque to the beam precludes the use of very thin material or some low-Z elements. Typical slit blades used for conventional, incoherent x-ray experiments meet this requirement with brass blades. Additionally, the edges of the aperture must be smooth and have a well-defined shape. Some apertures which have been used by other investigators consisted of a metallic film which was evaporated and laser-drilled repeatedly to form a series of pinholes ranging in size from 5 μm to 200 μm. These pinholes have the drawback that their edges are not particularly well-defined, so that the Fraunhofer diffraction patterns produced by them deviate significantly from the Airy function shape one would predict for a circular aperture. Also, the pinholes do not allow the selection of a continuously variable size as do adjustable slits.

We have used a novel roller-blade slit design, shown in Figure 2.4, which is capable of continuous gap settings from zero to 200 μm [40]. Each slit consists of two polished molybdenum cylinders of 1 cm diameter, which are clamped together with steel shim spacers of either 50 μm or 250 μm thickness. The slits are tipped about their mutual axis to pinch off the beam. With these slits, we are able to select horizontal and vertical gaps from zero to about 100 μm and to position the slits with a precision of 0.25 μm. The reproducability of the gap setting and the postioning is quite good, due to the flexural-pivot design, the sizable mechanical reduction in the movements, and the 1 μm precision of the computer-controlled actuators themselves. We found the ability to position the slits reproducably on such a fine scale to be invaluable in searching the grains of the Cu_3Au specimen. Figure 2.5 shows the crossed pair of roller-blade slits in the configuration used for the experiment.

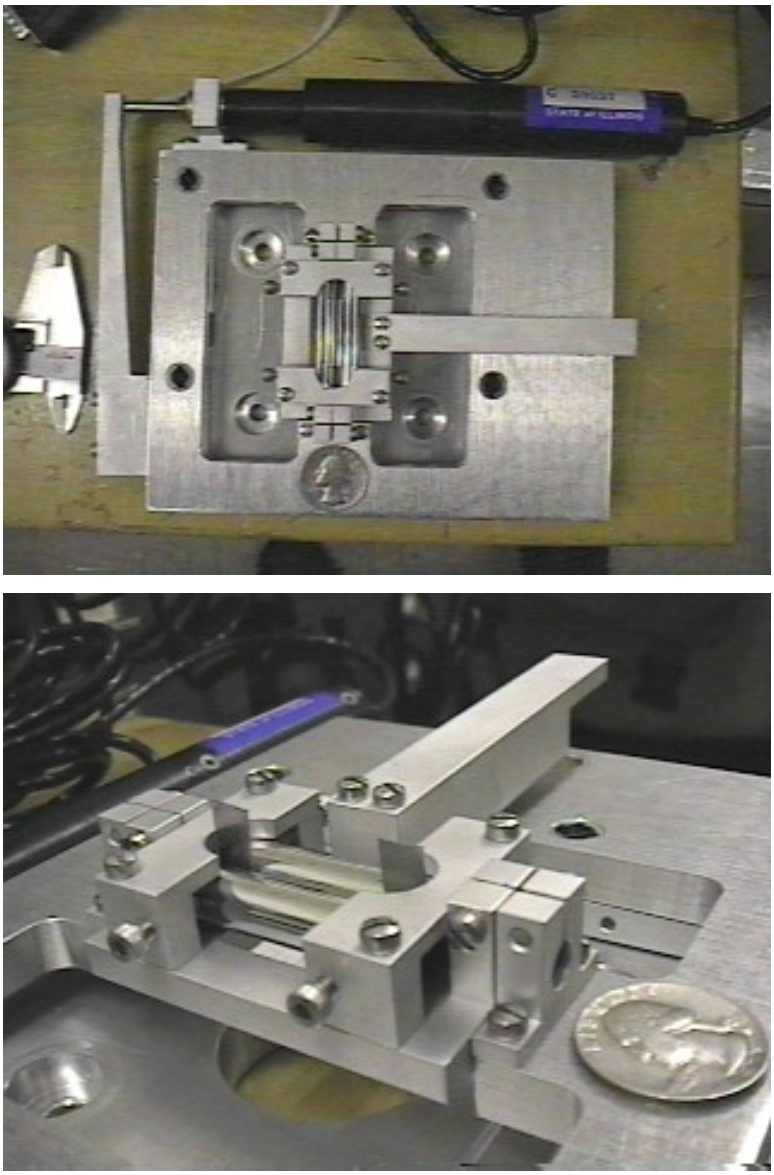

Figure 2.4: Roller-blade slits. Polished molybdenum cylinders, separated by 200 μm shims, are mounted on flex pivots to allow them to be rotated by an actuator at the end of a lever arm. A second actuator allows translation of the slit assembly on another set of flexural pivots with a 4:1 reduction.

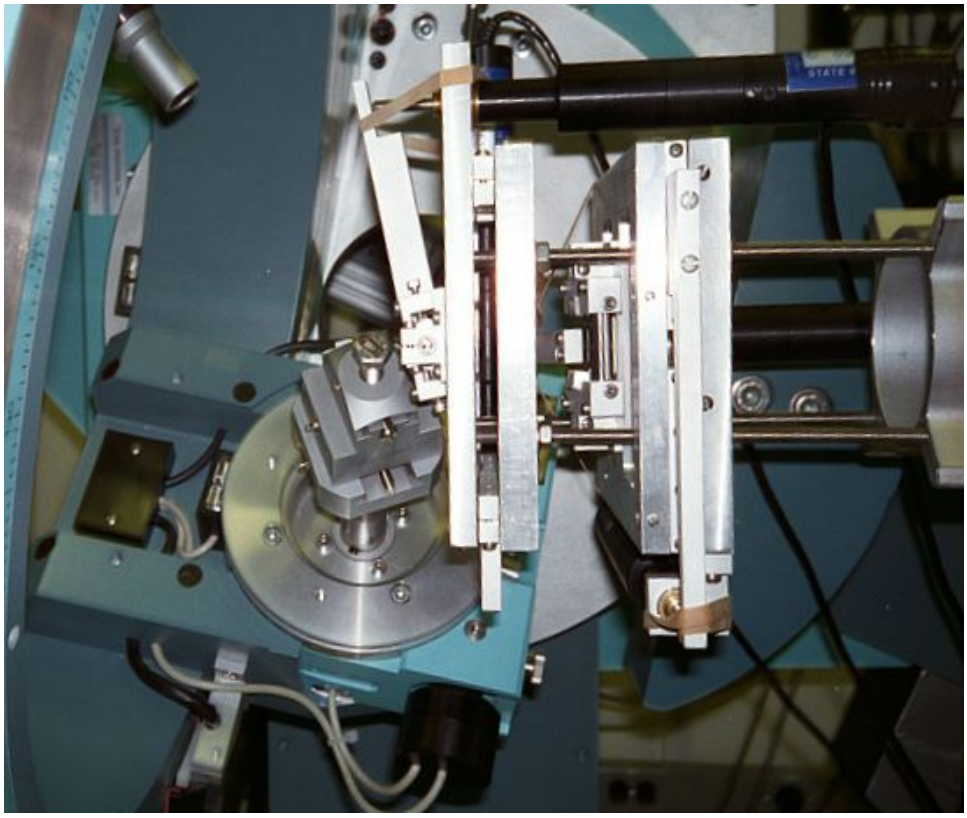

Figure 2.5: Roller-blade slits as mounted for CXD experiment. A crossed pair of roller-blade slits, forming the micrometer-scale aperture needed for preparing a coherent x-ray beam, is shown mounted to the end of an X95 structural rail. The beam passes through the center of the rail from the right, enters the slits, then propagates to the sample, which can be seen mounted to the goniometer.

The tipping roller-blade design does have a notable characteristic: the effect of the slits becomes very asymmetric when the gap is nearly closed. This property is clearly seen in Figure 2.6. The reason for the asymmetry is straightforward. Consider viewing the vertically closing slit from the detector position. Let the slit be oriented such that it closes by tipping the upper cylinder toward the detector. Now, above the centerline of the beam, the slit appears to be tipped by a larger angle than it does from below the centerline of the beam. As a result, the slit appears to have a narrower gap when viewed from the upper part of the observation plane and a larger gap when viewed from the lower part.

To test this picture of the parallax effect of the roller-blade slits, I have generated horizontal and vertical traces of the image from Figure 2.6 by summing 100-pixel wide strips. Then, I fit these to the familiar Fraunhofer sinc-function diffraction pattern, but at each point computing the intensity assuming a slit d-spacing which was linearly related to the position in the pattern. Since the slits do not pass any beam for negative values of d, I forced points with negative d to have zero intensity. Also, the intensity at a given point is scaled by d, because a larger slit accepts a larger area of the incident beam. Finally, a constant background term was added to the intensity at each point. See Figure 2.7 and Figure 2.8 for the results of the fit. The resulting fits are seen to deviate significantly from the observed intensity. As the effective d-spacing would be expected to have a more complicated dependence on the angle from which the slit is viewed, I switched to a piecewise-linear fitting function for d and fit to the observed intensity again. The results of those fits are shown in Figure 2.9 and Figure 2.10. The piecewise-linear fits capture the behavior of the Fraunhofer patterns fairly well. The fringes are more modulated in the fit than in the observations, however. Partial coherence would have the effect of washing out the fringes; however, if this were the dominating contribution to the loss of contrast, one would expect the vertical and horizontal contrasts to differ due to the difference in

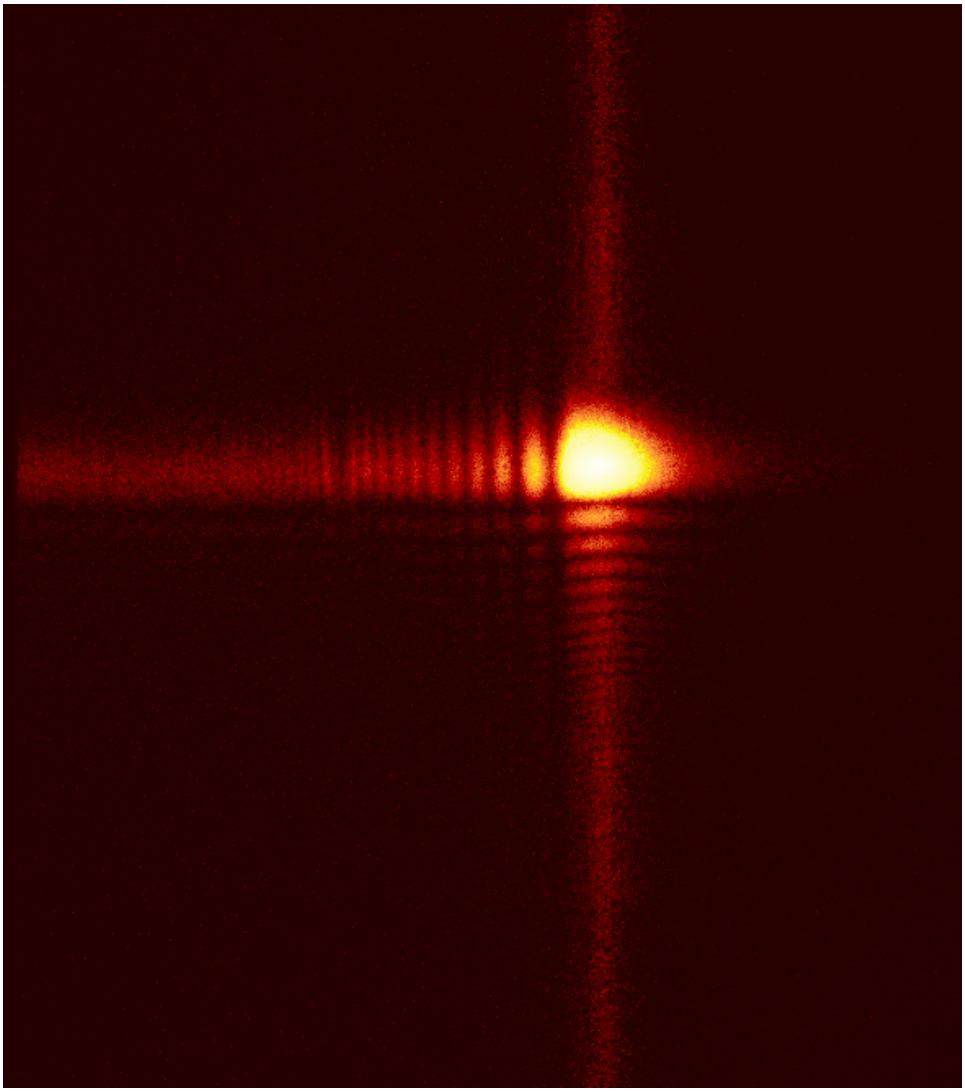

Figure 2.6: Asymmetric Fraunhofer diffraction from the roller-blade slits. The image shows a 588 × 664 pixel region of a CCD image, acquired in 10 accumulations of 2 seconds each and with a beam energy of 6.875 keV. The gray levels are mapped to a log scale of intensity. The raw image is cataloged as `J99_63.SPE`.

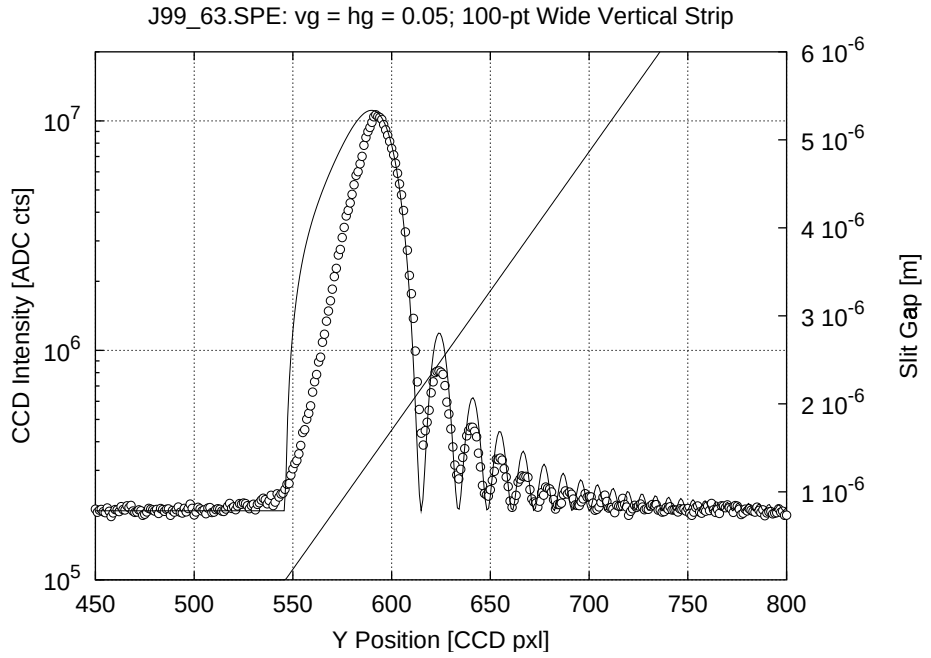

Figure 2.7: Fit to vertical Fraunhofer pattern using linear effective-d approximation. The position axis is numbered according to the indexing scheme of the Princeton Instruments software, with positive y running from top to bottom. At the peak position, the effective slit gap, or d-spacing, is close to 1 μm. The data are taken from the image cataloged as `J99_63.SPE`.

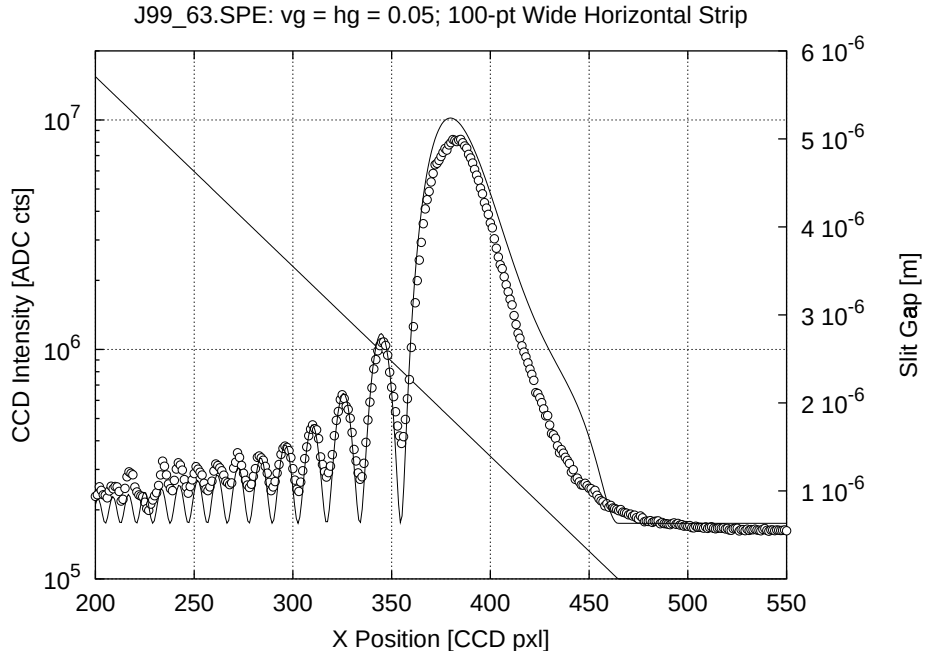

Figure 2.8: Fit to horizontal Fraunhofer pattern using linear effective-d approximation. The data are taken from the image cataloged as `J99_63.SPE`.

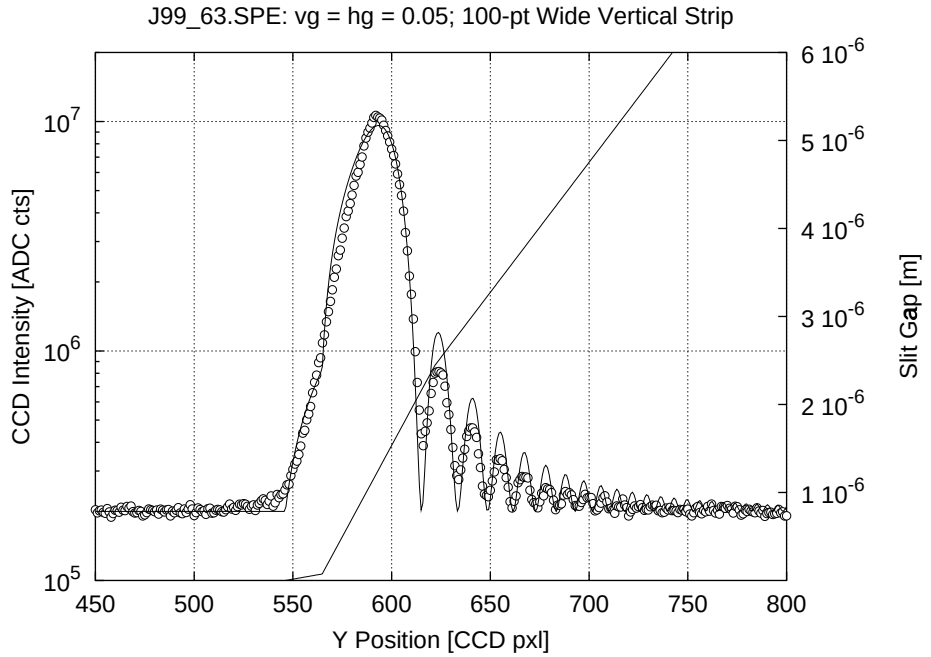

Figure 2.9: Fit to vertical Fraunhofer pattern using piecewise linear effective-d approximation. Compare this fit with that of Figure 2.7. The data are taken from the image cataloged as `J99_63.SPE`.

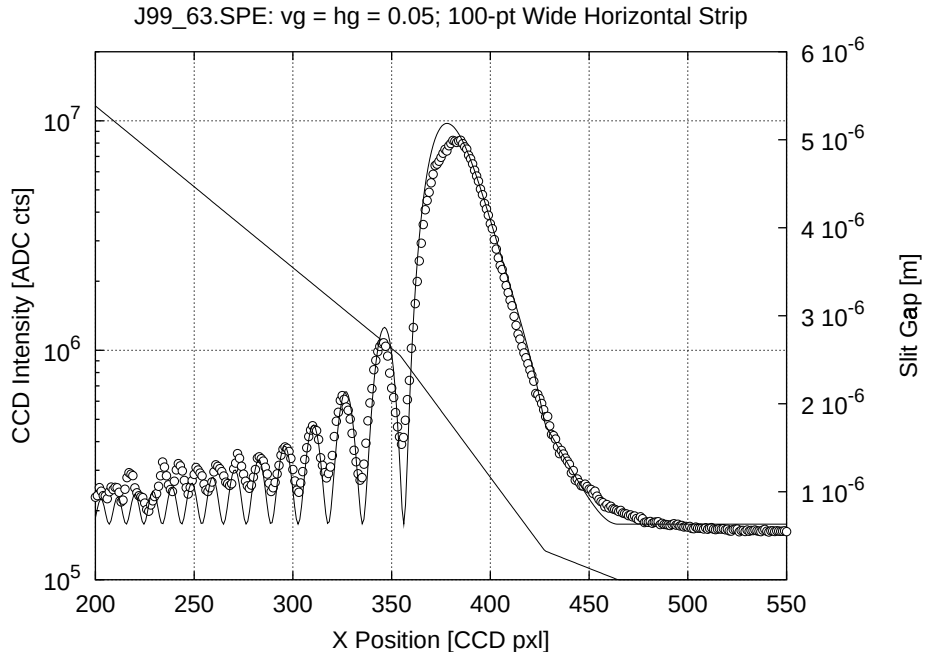

Figure 2.10: Fit to horizontal Fraunhofer pattern using piecewise linear effective-d approximation.Compare this fit with that of Figure 2.8. The data are taken from the image cataloged as `J99_63.SPE`.

ξ_x and ξ_y. The measurements do not show a considerable difference in the contrast along the vertical and horizontal directions. The beam here is propagating through some 2.95 m of air and two Kapton windows, so a bit of scattered radiation may be falling on the detector at the positions of the minima. Also, the detector pixels actually integrate an area of 22 μm $\times$ 22 μm, so some intensity gets counted in the positions where zero values are expected.

The importance of measuring the Fraunhofer diffraction pattern for a given setting of the slits will become more clear in Chapter 4. In short, far-field measurements like that of Figure 2.6 are the best means of calibrating the effective d-spacing of the slits, as there is no absolute reference for the size of the slits available directly. Also, the far-field measurements can be used as a guide while constructing the near-field illumination of the the sample, which has too fine a structure to be measured with the detection system in place at the current time. The amplitude shape of the wavefront illuminating the sample plays a crucial role in the phase retrieval techniques to be discussed later.

2.5 Four-Circle Diffractometer

Sample orientation and detector positioning was accomplished with a standard Huber four-circle diffractometer scattering upward, with the instrument axis horizontal. See Figure 2.11.

A widely used standard system of definitions for the diffractometer angles is derived from that of Busing and Levy [41; 42]. Refer to Fig. 2.12 for the definition of the angles. The angle the detector arm makes with the primary beam is defined '2θ'. Fixing '2θ' also fixes the magnitude of the momentum transfer, $\mathbf{q}$, as follows:

$$|\mathbf{q}| = 2\,|\mathbf{k}| \sin\left(\frac{\text{`}2\theta\text{'}}{2}\right) . \tag{2.11}$$

The second diffractometer axis, which lies along the '2θ' axis and causes the χ circle

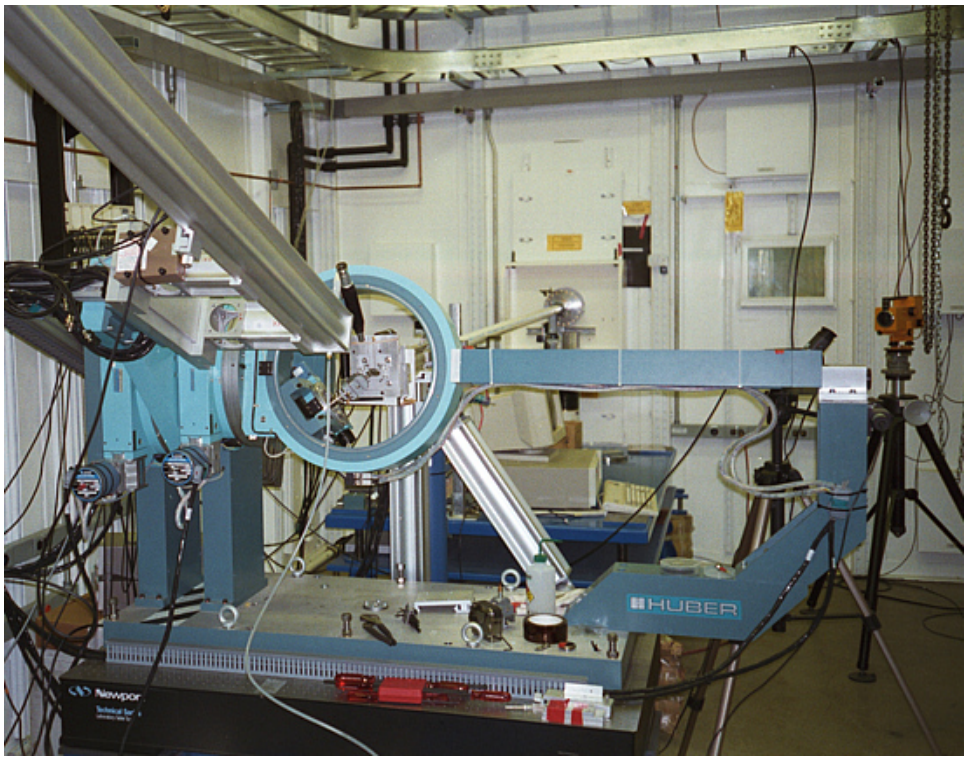

Figure 2.11: Huber diffractometer as installed in APS hutch 33-ID-D. The '2θ' rotation stage at the far left moves the detector, which is attached to the end of the 2.5 m X95 rail at the upper-left corner of the image, in the vertical plane. The next rotation stage from the left gives the θ motion. Attached to the θ stage is the χ circle, which in turn rotates the ϕ stage. The beam enters the hutch through the transport pipe in the far wall.

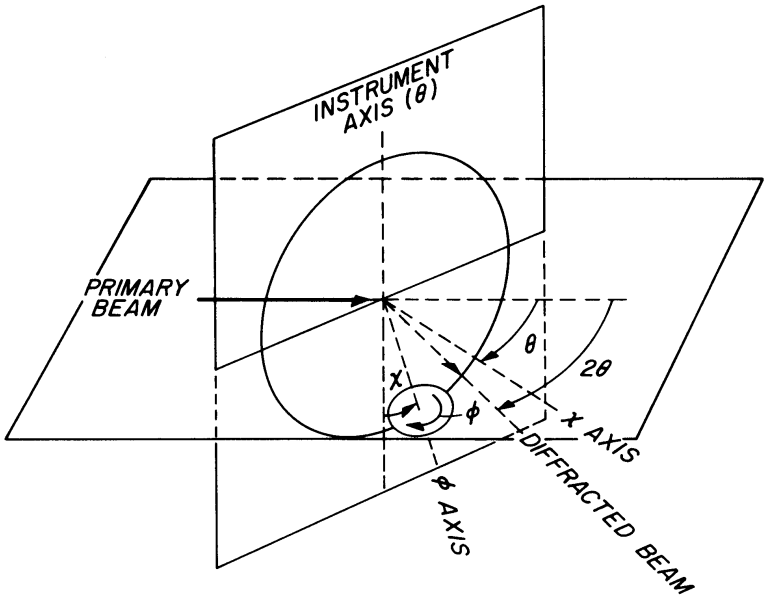

Figure 2.12: Standard four-circle diffractometer angle definitions. Note that the instrument axis is typically horizontal at synchrotron installations, so that the beam is scattered vertically. Figure taken from Ref. [42].

to rotate, is commonly labeled the θ-axis. The angle θ is defined to increase in the same sense as does '2θ'. In practice, θ and '2θ' are considered to be independent variables, and a third angle, ω, is defined

$$\omega \equiv \theta - \frac{\text{`}2\theta\text{'}}{2}\,. \tag{2.12}$$

Accordingly, the χ-axis makes an angle $\theta = \omega + $ '2θ'$/2$ with the primary beam. This differs from the definition shown in the Busing and Levy paper, where θ is not considered independent of '2θ', and the angle of the χ-axis with the primary beam is defined $\theta + \omega$. The present definition for θ, however, has the advantage that it represents an actual mechanical motion of the instrument. The χ and ϕ motions of the instrument are as shown in Figure 2.12. Note that the zero of ϕ is arbitrary, but that the direction in which ϕ increases is as shown in the figure.

The three reference frames which must be considered are the following: the sample frame, the diffractometer (or ϕ-stage frame), and the laboratory frame. The sample frame is considered fixed to the sample itself, which in general can have any orientation relative to the ϕ stage and depends on the sample mounting and on the setting of

the goniometer head if present. Usually, it is most convenient to have the reflecting surface of the sample facing upward. Note that the surface normal of the sample need not have any particular relationship with the crystal axes of a sample.

The reciprocal-space structure of the sample is probed via $I(\mathbf{q})$, so that $\mathbf{q}$ is naturally defined relative to the sample frame; however, the momentum transfer $\mathbf{q}$ is constructed as a difference of the incident and final wavevectors, $\mathbf{k}_i$ and $\mathbf{k}_f$, which are naturally described in the laboratory frame. Hence, a method for converting from one frame to the other is required. The orientation matrix, U, maps the sample frame onto the diffractometer frame, according to the relation

$$\mathbf{h}_\phi = \mathsf{U}\mathbf{q}\,, \tag{2.13}$$

where $\mathbf{h}_\phi$ is now a vector in the frame attached to the ϕ stage of the diffractometer. The diffractometer rotation matrix, $\mathsf{R}(\theta, \chi, \phi)$, maps the coordinate frame attached to the ϕ stage into the laboratory frame. If we define the x direction in the lab frame to be along the momentum transfer, then the equation

$$\begin{pmatrix} |\mathbf{q}| \\ 0 \\ 0 \end{pmatrix} = \mathsf{R}\mathbf{h}_\phi = \mathsf{R}\mathsf{U}\mathbf{q} \tag{2.14}$$

must be solved for a given $\mathbf{q}$ to obtain a suitable set of the diffractometer angles (θ, χ, ϕ). The orientation matrix U can be obtained by aligning the instrument on two known points in reciprocal space when the crystal lattice parameters are known or by aligning on more than two known reflections to obtain the orientation matrix and the lattice parameters by least-squares refinement [41].

Since Equation 2.14 reduces to only two equations in the three variables (θ, χ, ϕ), an infinite set of solutions usually exists. This redundancy can be easily demonstrated by allowing the sample to rotate about an axis parallel to the momentum transfer, $\mathbf{q}$. During the rotation, the same point in reciprocal space is being probed. Typically,

such a rotation involves motion of all of the (θ, χ, ϕ) axes. A practical limitation on the range of rotation is that the primary beam must be directed into the surface and that the diffracted beam must exit through the surface. In terms of the surface normal, $\hat{\mathbf{n}}$, these conditions mean

$$\mathbf{k}_i \cdot \hat{\mathbf{n}} < 0, \text{ and } \mathbf{k}_f \cdot \hat{\mathbf{n}} > 0\,. \tag{2.15}$$

It is often convenient to define the angle of incidence, relative to the surface normal,

$$\alpha_i = -\arcsin\left(\mathbf{k}_i \cdot \hat{\mathbf{n}}\right)\,, \tag{2.16}$$

and the angle of exit,

$$\alpha_f = \arcsin\left(\mathbf{k}_f \cdot \hat{\mathbf{n}}\right)\,. \tag{2.17}$$

Then, the conditions of 2.15 are equivalent to the requirement that both α_i and α_f be positive.

The case of α_i approaching zero corresponds to the grazing incidence condition. Because of the very small penetration depth, grazing incidence x-ray diffraction (GIXD) has been applied in measurements requiring surface sensitivity [43]. The penetration depth in the case of GIXD is given by Equation 1.16 with a correction for refraction at the sample surface:

$$w_z = \left(\sum_{j=1}^{N} \rho_j \mu_j\right)^{-1} \frac{\sin\alpha_f \sqrt{\sin^2\alpha_i + n^2 - 1}}{\sin\alpha_f + \sqrt{\sin^2\alpha_i + n^2 - 1}}\,, \tag{2.18}$$

where n is the index of refraction of the material, and the sum runs over the N types of atom in the material, each with mass density ρ_j and mass attenuation coefficient μ_j. Of course, the above expression for w_z is valid only when the quantity within the radical is positive; otherwize, w_z is imaginary with magnitude giving the penetration depth of the evanescent (non-propagating) wave into the sample. An analogous expression for the grazing exit condition also exists. From electron theory, the index of

refraction for a substance with N_e electrons per unit volume, is [8]

$$n = 1 - \frac{r_e \lambda^2 N_e}{2\pi} \,. \tag{2.19}$$

Since n is less than unity for x-rays, total external reflection is possible, giving GIXD surface sensitivity down to a few atomic layers. The value of $1 - n$ typically is of order 10^{-6} or 10^{-5}.

The Huber diffractometer we used is stated by the manufacturer to have a sphere of confusion of 10 μm, which results from the lack of perfect sphericity in the ball bearings. As we regularly use a beam only 5 μm in size at the sample position for CXD measurements, such a sphere of confusion means that reorienting the sample also translates the sample by a distance larger than the beam size. Thus, the sample cannot be rotated with any of the diffractometer axes with the expectation that the beam will still illuminate the same region of the sample, unless some measures are taken to adjust the position of the beam by translating the slits.

2.6 CCD Area Detector

For detecting CXD speckle patterns as well as Fraunhofer diffraction patterns such as that of Figure 2.6, we used a commercially available charge-coupled device (CCD) from Princeton Instruments. The model LCX-TE/CCD-1242EHR CCD was equipped with an EEV CCD-05-30 Grade 2 CCD chip, which makes use of a special deep depletion manufacturing process to increase the densitive depth of the silicon for x-rays in the 4 keV to 10 keV range. The format of the CCD is 1152 $\times$ 1242 pixels measuring 22.5 μm $\times$ 22.5 μm [44]. A somewhat smaller region than the 25.9 mm $\times$ 27.5 mm CCD area is sensitive to x-rays, due to some protective masking near the edges. Instead of coupling to the x-rays via a phosphor screen, the CCD is mounted to detect the x-ray photons directly. This has a marked advantage in spatial resolution over typical phosphor screen designs; however, some new detectors have phosphor screens

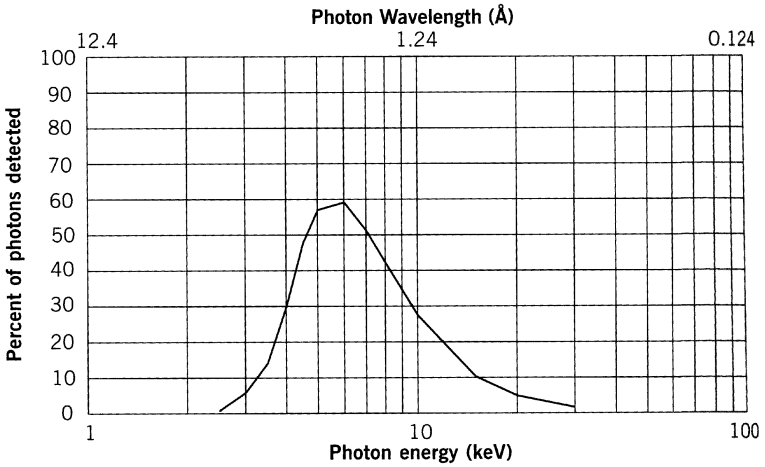

Figure 2.13: CCD quantum efficiency with direct detection and special silicon. The absorption of x-rays by the beryllium window is taken into account. Reproduced from Ref. [44].

that are coupled to the CCD via a microscope objective and can achieve a spatial resolution near 1 μm. The full well capacity of each pixel is 500,000 electrons, or about 250 8.5 keV photon events. The readout noise is 4 to 10 electrons per pixel with 100 kHz readout.

The CCD is thermoelectrically cooled to $(-50 \pm 0.05)^{\circ}$C with water circulation, with the temperature controlled by the Princeton Instruments ST-138 camera controller. The typical dark charge at this temperature is six to eight electrons per pixel per second for normal pixels, while absorption of an 8.5 keV photon produces about 2000 electrons in a pixel.

The quantum efficiency of the detector, accounting for its beryllium window, is stated by the manufacturer to be 55% at 6.5 keV, as shown in Figure 2.13. Our own estimates based on comparison with the counts detected by a Bicron scintillation detector indicated a quantum efficiency between 20% and 30% at 6.5 keV. Since lower energy photons are more efficiently absorbed by the detector, but are also more likely to be absorbed in the air path in the experiment, the beam energy must be optimized with both effects taken into consideration.

We mounted the CCD at the end of a 2.5 m long X95 structural rail. The ends

of the rail were capped with Kapton windows, and the inside of the rail was pumped down to provide a low-pressure flightpath for the diffracted beam. At atmospheric pressure, the transmission through 2.5 m of air is 0.5% for 6.5 keV x-rays and about 10% for 8.5 keV x-rays, so clearly a large gain in measured intensity results from pumping out the flightpath.

The Grade 2 specification means that some number of defects in the chip exist, which typically have the result of a larger dark current for some number of pixels, clusters of pixels, or columns of pixels. A Grade 1 CCD, with a smaller number of defects, is available at a higher cost. Since photon events produce such a large number of electrons in the CCD, dark current is only a concern for very long exposure times.

With the powerful beam present at the undulator beamline, a major concern is beam damage to the CCD. The output amplifier and shift register are protected from the beam by a mask. The first stage of failure is that the dark current begins to increase in the pixels where exposure has been high. According to the manufacturer, this effect can be observed after the lifetime exposure exceeds about 10^6 detected (or detectable) 8 keV photons per pixel, corresponding to about 4,000 acquired images with the same pixel saturated each time. The second stage of failure begins with the formation of a charge trap, which prevents charge from other pixels in the same column as the affected pixel from shifting through during readout. The resulting image is similar to one having a partial bad column defect. Other columns will continue to operate, unaffected by the trap. The onset of this stage of failure occurs after around 5×10^7 detected 8 keV photons per pixel, or about 200,000 images having the same pixel saturated each time. The real risk, however, is accidental exposure of the CCD to the direct undulator beam, where each pixel accepts of order 10^9 photons per second. In the direct beam, traps would be expected to form in the CCD in less than a second. Direct-beam measurements such as in Figure 2.6 are performed using very small slit settings and usually with some attenuation in the beam.

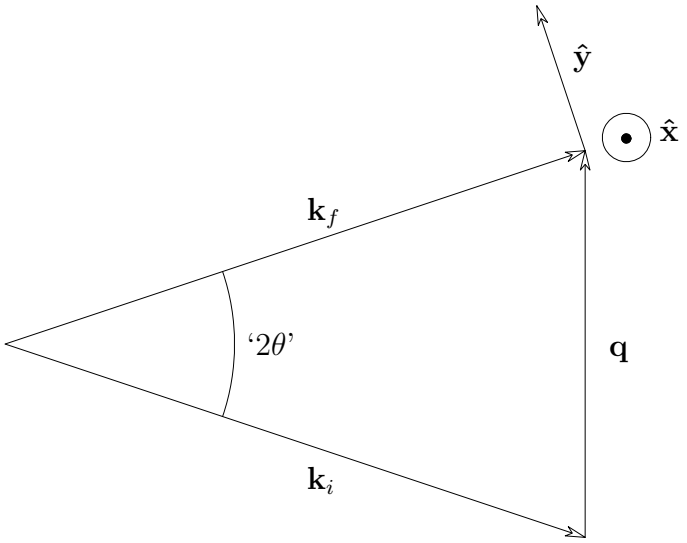

Figure 2.14: Definition of CCD axes. The scattering plane in reciprocal space is shown. $\hat{\mathbf{y}}$ is directed in the plane and perpendicular to $\mathbf{k}_f$, while $\hat{\mathbf{x}}$ is formed by $(\mathbf{k_f} \times \hat{\mathbf{y}})/\left|\mathbf{k}_f\right|$.

The sampling of reciprocal space by an area detector can be described through the use of the Ewald construction. The pixels on the CCD measure intensities at angular deviations about the $\mathbf{k}_f$ direction. Thus, the pixels map onto a patch on the Ewald sphere, with some particular pixel sampling precisely the point $\mathbf{q}$ in reciprocal space determined by the diffractometer angles and the beam energy. If the diffractometer is very accurately aligned, then the point at the center of the CCD can be taken to lie at $\mathbf{q}$. Define two unit vectors, $\hat{\mathbf{x}}$ and $\hat{\mathbf{y}}$, attached to the frame of reference of the detector and oriented as shown in Figure 2.14. As mounted, such that the top of the CCD points in the direction of increasing '2θ', the $\hat{\mathbf{y}}$-direction corresponds to "up" on the CCD, while the $\hat{\mathbf{x}}$-direction corresponds to "right" on the CCD as viewed from the sample position. Since the angular width of the detector is small, less than 10 mrad., the spherical patch sampled by the CCD can be approximated by a plane with its normal oriented along $\mathbf{k}_f$. For a perfectly monochromatic beam, the image seen on the CCD would be the scattering intensity of the sample, $I(\mathbf{q})$, evaluated on this plane.

The situation is more complicated when the beam is only quasi-monochromatic.

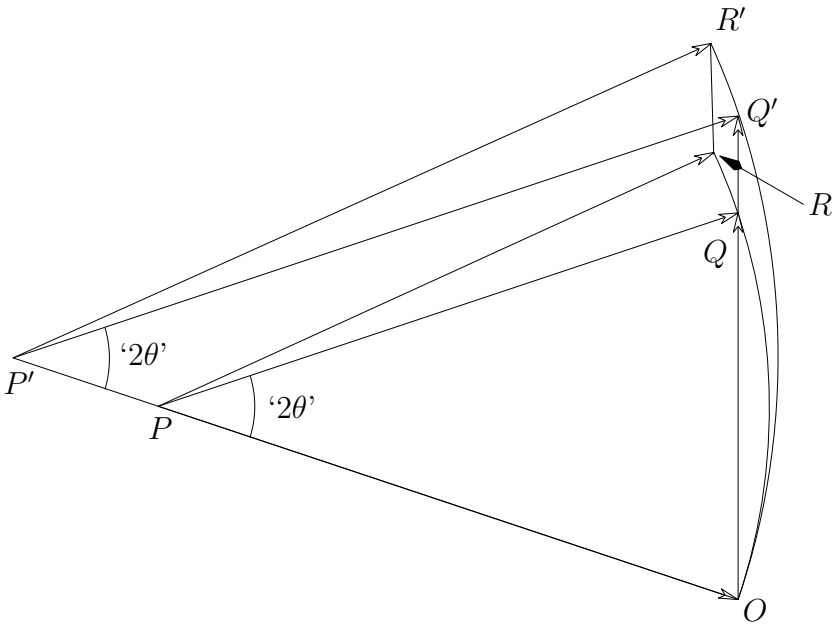

Figure 2.15: Quasi-monochromatic Ewald construction. The Ewald construction can be extended to represent the scattering of a quasi-monochromatic beam comprised of a range of wavenumber from k to $k + \Delta k$. The points P and Q lie at $-\mathbf{k}_i$ and $\mathbf{q}$, respectively, while the points P' and Q' are at $-(1 + \Delta k/k)\mathbf{k}_i$ and $(1 + \Delta k/k)\mathbf{q}$. Also, $PQ = PR$, $P'Q' = P'R'$, and $\angle QPR = \angle Q'P'R'$ (shown greatly exaggerated).

Such a description is necessary in our case, because the reciprocal-space structure of Cu_3Au, the resolution of the CCD, and the bandwidth of the beam are all of about the same order of magnitude in size. The reciprocal space structure of Cu_3Au will have modulation on a size scale given by the inverse of the size of the illuminated region, which is approximately $2\pi/\left(5\mu\text{m}\right) = 1.3 \times 10^{-4}$ Å^{-1}. The step size in reciprocal space corresponding to one pixel spacing, l_p, is $kl_p/L_2 \approx 3.3 \times 10^{-5}$ Å^{-1}, where L_2 is the distance from the sample to the detector, and $k = |\mathbf{k}_i| = |\mathbf{k}_f|$ is the wavenumber of the beam. The bandwidth of the beam yields a distribution in k of $\Delta k \approx 6.0 \times 10^{-4}$ Å^{-1}.

To illustrate which point in reciprocal space are probed by the pixels of a CCD in the case of a quasi-monochromatic beam, we consider the construction in Figure 2.15. A portion of the Ewald sphere for each of two wavenumbers, k and $k + \Delta k$, is drawn in the scattering plane. Note that the direction of $\mathbf{k}_i$, and the angle '2θ', are the same for both constructions since they are set by the diffractometer angles only. Hence, the intensity $I(\mathbf{q})$ will be summed with the intensity $I((1 + \Delta k/k)\mathbf{q})$ at the

same pixel, if both wavenumbers are present in the beam. Of course, the summation here is *incoherent* summation, since waves of different frequencies do not interfere on the time scale of any measurement. Since the pixels on the CCD map to angular deviations about the diffracted wavevector, the intensity of the points R and R' sum together at a different pixel than the one which samples the points Q and Q'. If all wavenumbers between k and $k + \Delta k$ are present, then the intensity from all points in reciprocal space from Q to Q' will be summed into a single CCD pixel, and all points from R to R' will be summed into another pixel.

In general, the energy spectrum of the beam gives rise to a distribution in k, which we will call $f_k(k)$. Let us define $I(\mathbf{q}_0, k, x, y)$ to represent the intensity measured at the CCD pixel (x, y), when the diffractometer angles are configured for momentum transfer $\mathbf{q}_0$ at the mean wavenumber, k_0, and a monochromatic beam of wavenumber k is present. This expression is equal to $I(\mathbf{q}')$, where

$$\mathbf{q}' = \left(\frac{k}{k_0}\right)\mathbf{q}_0 + \frac{kxl_p}{L_2}\hat{\mathbf{x}} + \frac{kyl_p}{L_2}\hat{\mathbf{y}}. \tag{2.20}$$

In other words, $I(\mathbf{q}_0, k, x, y)$ is only the intensity distribution in reciprocal space, evaluated on a patch of the Ewald sphere of radius k. If the width of the distribution $f_k(k)$ is so sharp that $I(\mathbf{q})$ has no structure on that scale, then what is seen on the detector is very nearly $I(\mathbf{q}_0, k_0, x, y)$. However, if, as will be demonstrated to be the case in the next chapter, $I(\mathbf{q})$ does have structure on the scale of the width of $f_k(k)$, then to model the diffraction pattern seen on the detector, $I(x, y)$, requires a convolution such as the following:

$$I(\mathbf{q}_0, x, y) = \int f_k(k) I(\mathbf{q}_0, k, x, y)\, dk\,. \tag{2.21}$$

This type of convolution was used for the model streak images to be presented in the next chapter.

Chapter 3

Cu_3Au CXD Measurements

3.1 Introduction

The first CXD experiment with Cu_3Au was reported in 1991 [45], and those measurements, performed at the X25 wiggler beamline of the National Synchrotron Light Source (NSLS) at Brookhaven National Laboratory, demonstrated the feasibility of CXD and XIFS in the hard x-ray regime. It was pointed out in an earlier article that the speckle pattern obtained by CXD contains relatively complete structural information about the local configuration of the scatterers [46]. We sought to make measurements on Cu_3Au from which the antiphase domain structure could be obtained. In this chapter we report an experimental verification of the Cu_3Au antiphase domain characteristic size, studied the effect of slit gap settings on speckle contrast, and observed a marked change in the shape and orientation of the speckles while varying the diffraction geometry.

3.2 Characteristic Size of the Antiphase Domains

The characteristic size of the antiphase domains in the Cu_3Au sample was obtained from incoherent diffuse x-ray scattering measurements. The sample was illuminated

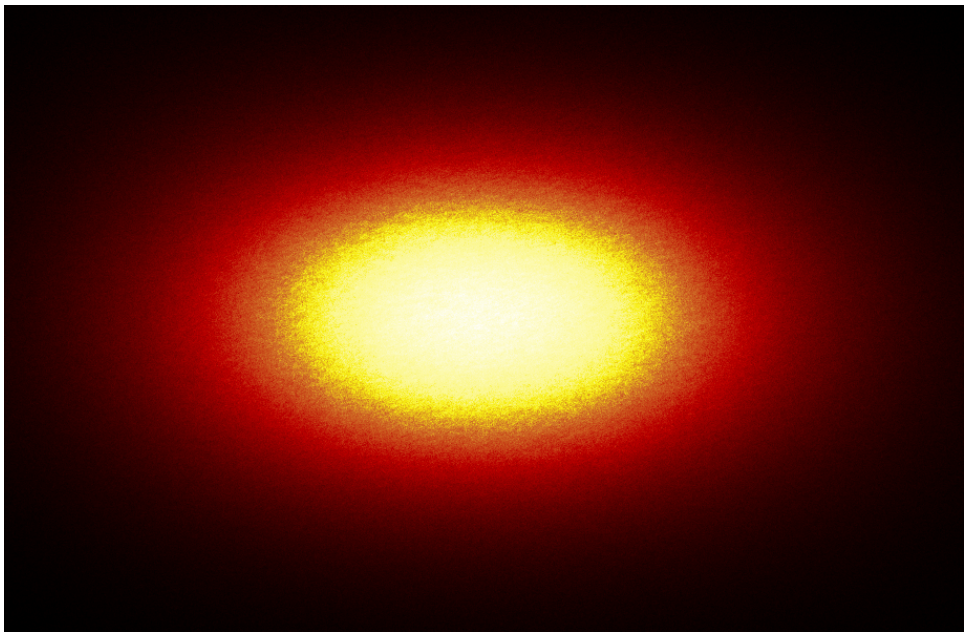

Figure 3.1: (100) reflection under nearly incoherent illumination obtained with the entrance slits fully open From the angular extent of this reflection, a measure of the characteristic size of the antiphase domains is made. The image was obtained in 10 accumulations of 8 s each; a 915 × 597 pixel region is shown. In this and following CCD images, the top of the image corresponds to the upward direction, or the direction of increasing '2θ'. The raw image is cataloged as `ID33_B75.SPE`.

by an incoherent beam, since the roller-blade slits were set near their maximum opening, which is far beyond the coherence length of the beam in both the horizontal and vertical directions. The absence of speckles in the diffraction spot under such illumination confirmed that the beam was not very coherent. See Figures 3.1 and 3.2 for images of the diffraction spot for the (100) and the (101) reflection, respectively.

Incidentally, the elliptical shape of the reflections is explained by the peak shape discussion of Subsection 1.3.2. The (100) reflection should have its long axis running along the CCD x-axis, which is horizontal in the figure, since $\mathbf{q}$ is near (100), the reflection is compressed along the (100)-direction. The x-axis of the CCD runs across the long diameter of the oblate spheroid of reflection, while the y-axis cuts through the short dimension of the reflection. By symmetry, the orientation of the observed ellipse should not depend on scattering geometry for the (100) reflection. However, at the (101) reflection, the same symmetry does not exist, and the orientation of the

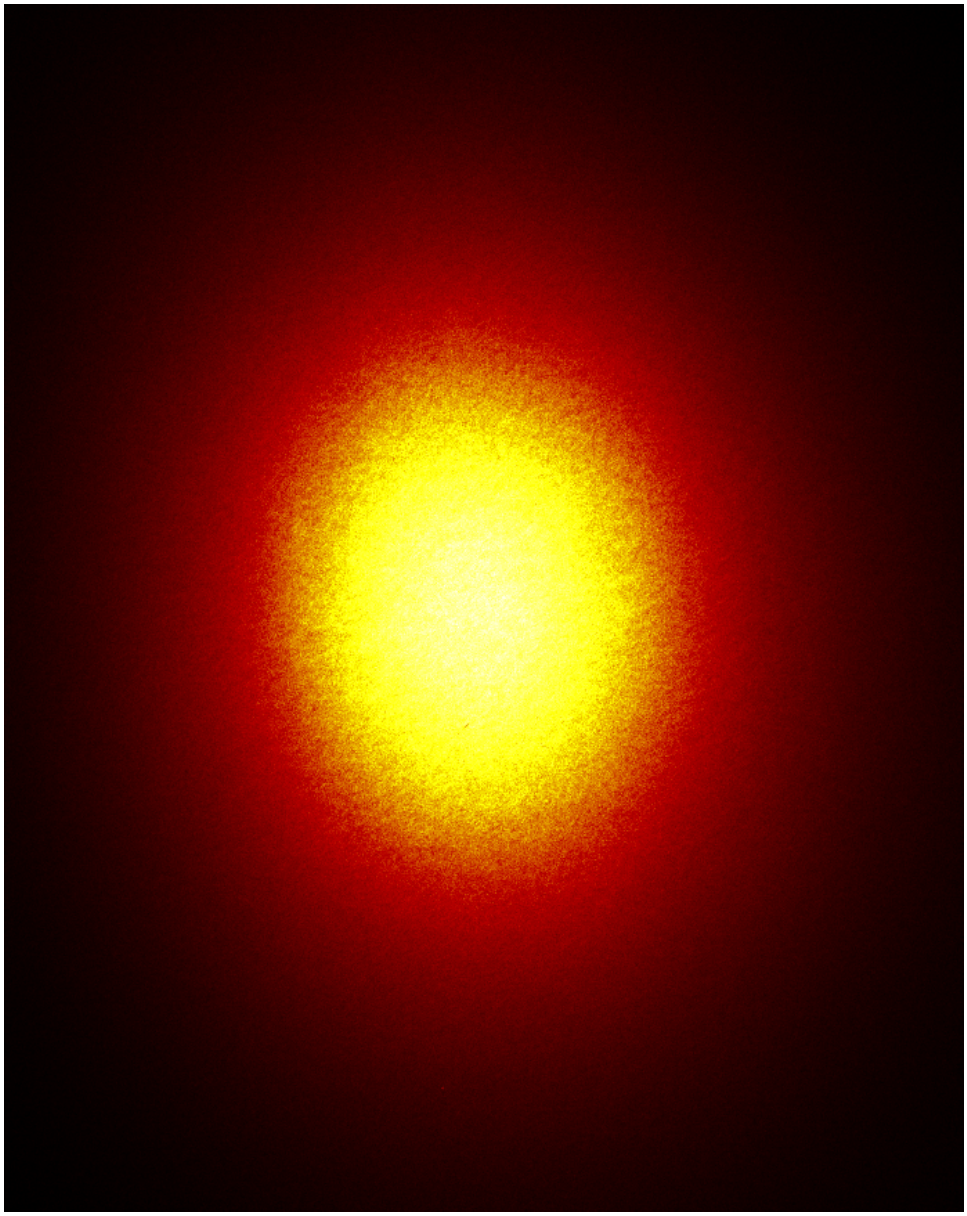

Figure 3.2: (101) reflection under nearly incoherent illumination. The image was obtained in 10 accumulations of 15 s each; a 694 × 873 pixel region is shown. The raw image is cataloged as `ID33_B76.SPE`.

observed spot should change with the reflection geometry as the $\mathbf{k}_i$ and $\mathbf{k}_f$ vectors revolve around an axis through $\mathbf{q}$. The images from Figures 3.1 and 3.2 bear out this qualitative description.

The characteristic particle size of a powder diffraction sample can be estimated by the Scherrer formula [8]:

$$L = \frac{\lambda}{B(\text{`}2\theta\text{'})\cos\left(\text{`}2\theta\text{'}/2\right)}\,, \tag{3.1}$$

where L is the characteristic size and $B(\text{`}2\theta\text{'})$ is the angular FWHM of the powder pattern peak. Here, we will take the characteristic size from the Scherrer formula to represent the domain size of the Cu_3Au sample. Note that there is a weak dependence on the scattering angle which predicts that the (101) peak should be slightly wider than the (100) peak for a given wavelength and particle size distribution. Even though the Cu_3Au specimen we measured was not a powder sample, but rather was a single crystal consisting of antiphase domains, the particle-size broadening effect is approximately the same.

To obtain the angular width of the incoherent spots, I have used a fitting function which includes an elliptical gaussian:

$$g(x,y) \equiv \exp\left(-\frac{1}{2}\left\{\frac{\left[x'(x,y,\theta_2)\right]^2}{\sigma_{x'2}^2} + \frac{\left[y'(x,y,\theta_2)\right]^2}{\sigma_{y'2}^2}\right\}\right)\,, \tag{3.2}$$

where the primed coordinates denote a counterclockwise rotation of x and y, according to

$$\begin{aligned} x'(x,y,\theta_2) &= x\cos\theta_2 + y\sin\theta_2 \\ y'(x,y,\theta_2) &= -x\sin\theta_2 + y\cos\theta_2\,. \end{aligned} \tag{3.3}$$

Without loss of generality, I have chosen to restrict $\sigma_{x'2} \geq \sigma_{y'2}$, so that the major axis of the ellipse lies along the x'-axis. The full form of the fitting function is

$$f_2(x,y) = I_{02}g(x-x_0, y-y_0) + I_B\,, \tag{3.4}$$

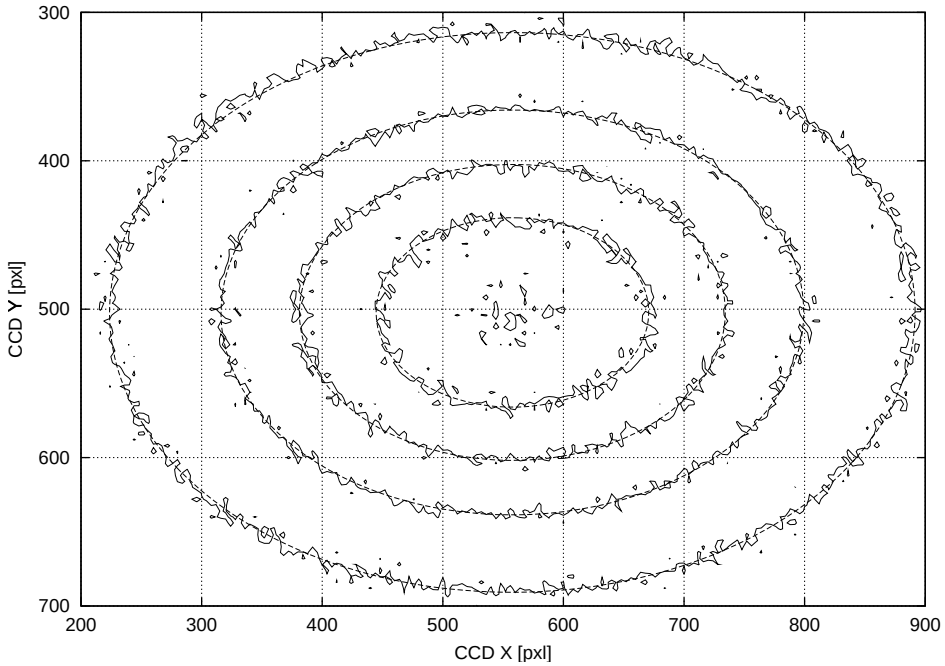

Figure 3.3: Fit to (100) incoherently illuminated Bragg reflection.The contour levels are 1×10^5, 2×10^5, 3×10^5, 4×10^5, and 5×10^5 ADC units, where ∼1000 ADC units corresond to a single photon. The data are from the image shown in Figure 3.1.

where I_{02} is the height of the gaussian, I_B is a constant background term, and (x_0, y_0) is the CCD pixel where the center of the spot lies. The fits were computed using gnuplot version 3.7, which employs a Marquardt-Levenberg algorithm [47]. Unit weights were assumed in the fit. Refer to Figures 3.3 and 3.4 for the fits and to Table 3.1 for the resulting fit parameters.

The fit suggests values of L around 500 Å for our Cu_3Au specimen. This can be used to estimate the number of speckles that would appear in a CXD measurement. If the beam footprint is 5 μm × 5 μm, and the thickness of the illuminated volume is 2000 Å or less, then the reflecting volume consists of a disordered structure of ∼100 × ∼100 antiphase domains in the in-plane directions, and from one to about five in the surface normal direction. In the case of either α_i or α_f small, we would expect the illuminated volume to be only one antiphase domain thick, so that the phase-modulating structure of the Cu_3Au would be approximately two-dimensional.

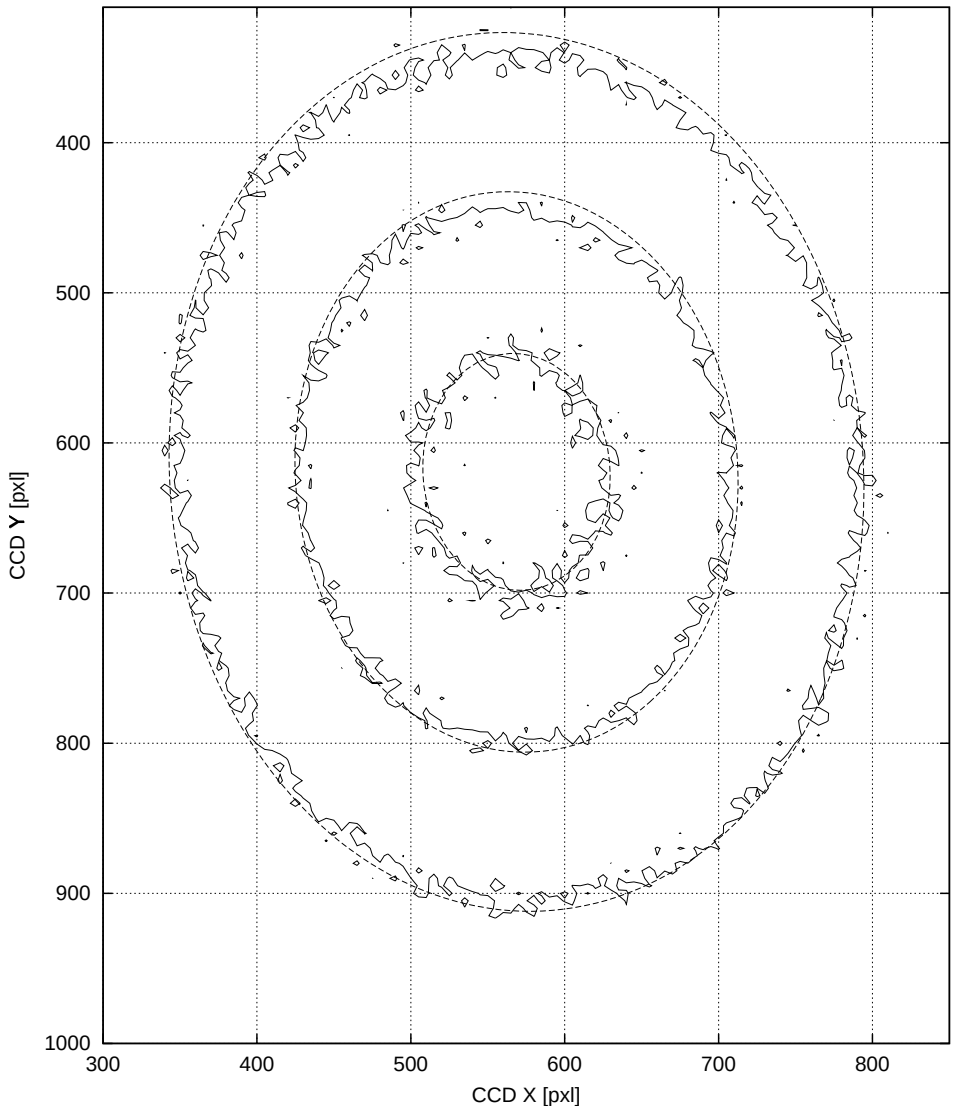

Figure 3.4: Fit to (101) incoherently illuminated Bragg reflection. The contour levels are 1×10^5, 2×10^5, and 3×10^5 ADC units. The data are from the image shown in Figure 3.2.

Table 3.1: Results of fitting the (100) and (101) incoherent Bragg reflections. The error estimates are the so-called "standard errors" and tend to greatly underestimate the actual uncertainty in the fits, but they provide some information on the variance-covariance matrix at the end of the fit [47]. The values of the characteristic size of the antiphase domains, L, were obtained from Equation 3.1. The fits are plotted in Figures 3.3 and 3.4.

Parameter	(100)	(101)
x_0 (pixels)	557.719 ± 0.0645	568.67 ± 4.008
y_0 (pixels)	502.191 ± 0.0516	619.313 ± 4.421
I_B (ADC cts.)	34030.7 ± 122.9	11406.6 ± 249.7
I_{02} (ADC cts.)	456894 ± 284.2	316654 ± 4637
θ_2 (degrees)	-0.087 ± 0.037	85.90 ± 0.32
σ_{x2} (pixels)	$169.7 \pm 8.36 \times 10^{-2}$	183.6 ± 1.07
σ_{y2} (pixels)	$95.82 \pm 4.8 \times 10^{-2}$	141.2 ± 1.51
L (Å)	490	470

3.3 Variation of Speckle Contrast with Slit Gap Setting

We investigated the dependence of the speckle contrast on the size of the aperture used to obtain a coherent beam. Speckle contrast measurements have been used by others recently for characterizing the coherence properties of x-ray sources at the ESRF [48] and at the NSLS [49]. In those experiments, it was the small-angle scattering from a 95%-void aerogel sample which provided the speckles. Aerogel is a highly porous form of silica which was selected as a static, highly disordered, strongly scattering medium. The sample was assumed to give rise to a phase modulation in the beam which is uniformly distributed on the whole interval $[0, 2\pi]$. This has certain implications for the statistical distribution of the intensity of the speckle pattern. If the sample is under completely coherent illumination, the distribution of intensity in the speckle

pattern is approximately [50]

$$p_{I_0}(I_0) = \frac{1}{\langle I_0 \rangle} \exp\left(-\frac{I_0}{\langle I_0 \rangle}\right) , \tag{3.5}$$

for $I_0 \geq 0$, and zero otherwise. Here, $\langle I_0 \rangle$ denotes the average of the speckle intensity over a region of the speckle pattern chosen to be flat except for the effects of coherent interference. For the case of small-angle coherent x-ray scattering, this region is an annulus centered at the position of the direct (unscattered) beam, since this describes the region having a reasonably uniform structure factor.

The origin of the expression for p_{I_0} is clear if one considers the speckle amplitude as the coherent sum over discrete secondary sources within the sample. If the relative phase of the secondary sources is indeed uniformly distributed over $[0, 2\pi]$, then the complex amplitude sum has the same form as that of a random walk in the two-dimensional complex plane. Thus, the total amplitude in the speckle pattern will have a circular Gaussian distribution in the complex plane. By a change of variables from the real and imaginary parts of the complex amplitude to the real-valued intensity and the phase, Equation 3.5 is obtained.

As discussed by Goodman in Ref. [50], the incoherent sum of N statistically independent speckle patterns, each one individually having mean intensity $\langle I_0 \rangle$, has an intensitity distribution

$$p_I(I) = \frac{I^{N-1}}{(N-1)!\,\langle I_0 \rangle^N} \exp\left(-\frac{I}{\langle I_0 \rangle}\right) . \tag{3.6}$$

This is a gamma distribution with mean $\langle I \rangle = N \langle I_0 \rangle$ and standard deviation $\langle I_0 \rangle$. Such an incoherent sum of speckle patterns could arise if the beam were considered to be made up of beams from N separate apertures, each one passing a fully coherent beam but each one incoherent with respect to the others, are arranged so that the beam from each one interacts with a collection of scatterers, and the resulting speckle patterns are observed together.

The above expression can be generalized to one allowing a non-integer number of independent speckle patterns $\mathcal{M}$ in the following way:

$$p_I(I) = \mathcal{M}^{\mathcal{M}} \left(\frac{I}{\langle I \rangle} \right)^{\mathcal{M}-1} \frac{e^{\mathcal{M}I/\langle I \rangle}}{\langle I \rangle \, \Gamma(\mathcal{M})} \, . \tag{3.7}$$

This expression becomes a negative exponential distribution in the limit $\mathcal{M} \to 1$, and a Gaussian in the limit $\mathcal{M} \to \infty$. From this probability density, it is seen that the speckle contrast is related to the number of speckle patterns by

$$\frac{1}{\mathcal{M}} = \frac{\sigma_I}{\langle I \rangle} \, . \tag{3.8}$$

Thus, for a perfectly-coherent sample illumination, one would expect unit contrast, and the contrast should decline to zero as the illumination becomes incoherent.

We made measurements of the speckle from the Cu_3Au (101) reflection with a series of slit settings to study the variation in the observed speckle contrast with slit size. See Figure 3.5 for example images from this series and Figure 3.6 for a plot of the contrast vs. horizontal slit aperture.

The speckle contrast, $\sigma_I / \langle I \rangle$, was calculated using the Princeton Instruments software for several small regions for each image in the series. The regions were chosen to be small enough that the contribution to σ_I from the broad peak shape was small compared with that from the speckles, yet the regions were large enough to contain a reasonable sampling of speckles. Each region yielded a somewhat different value for the contrast, and all the values are plotted in Figure 3.6. These data were then fit to the function $ae^{-bd_x} + c$ to obtain the curve shown. The result of the fit was that $a \approx 0.446$, $b \approx 0.072 \, \mu\text{m}^{-1} \approx 1/(14 \, \mu\text{m})$, and $c \approx 0.090$.

One might expect that as d_x and d_y together approach zero, that the coherence-related contrast should approach unity instead of the observed value $a \approx 0.446$. There are a few mechanisms which might degrade the contrast at very small slit openings. The first is the effect of limited temporal coherence; if the optical path length difference between reflection from the sample surface and from deep within

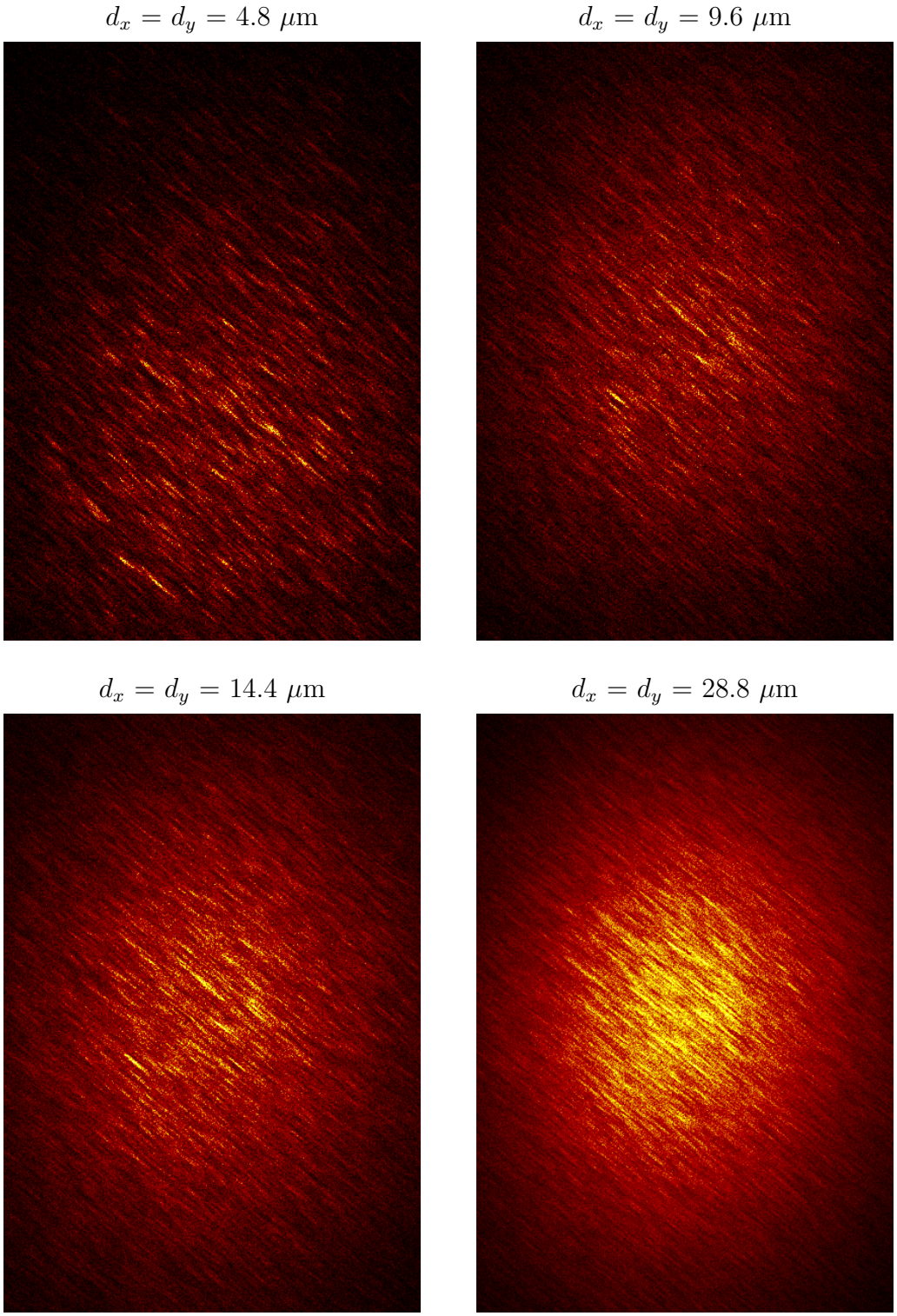

Figure 3.5: $Cu_3Au(101)$ reflections with varied slit openings d_x and d_y. Shown is a 412 $\times$ 592 pixel region of each image. The raw data are cataloged in the files `ID33_B50.SPE`, `ID33_B52.SPE`, `ID33_B53.SPE`, and `ID33_B56.SPE`.

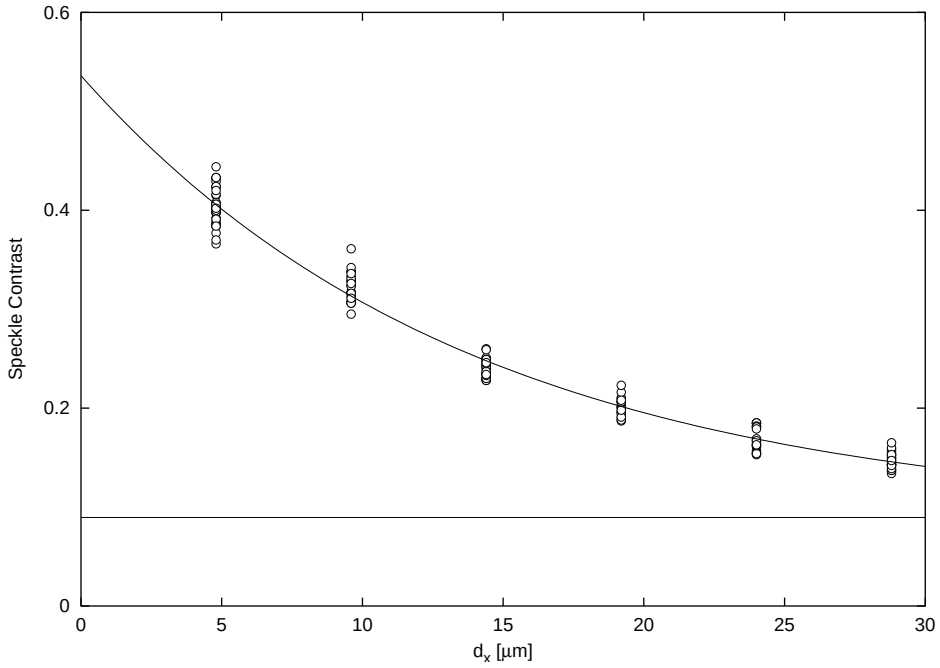

Figure 3.6: Speckle contrast vs. horizontal slit opening for the Cu_3Au (101) Bragg reflection. The speckle contrast was defined to be $\sigma_I / \langle I \rangle$ and calculated for several small patches for each image, resulting in a spread of values. The data were fit to the function $ae^{-bd_x} + c$, and the line $\sigma_I / \langle I \rangle = c$ is plotted.

the sample is not much less than the temporal coherence length, the speckle contrast will not reach unity even in the case of perfect spatial coherence associated with a very small aperture. To decrease this effect, one might increase the temporal coherence by altering the monochromator configuration, choose a diffraction condition which results in a smaller optical path length difference, or make the measurements with a smaller sample thickness.

A second effect concerns the detection mechanism. The speckles in the series possess the streaked character which will be discussed further in another section, and the correlation length of the speckles across their short dimension measures only a few CCD pixels. In effect, each pixel of the image represents an integration over its area, resulting in a box-car approximation to the true intensity distribution, and the result is the suppression of sharp local extrema in the speckle pattern, hence a decrease in contrast. For a more extensive discussion of the impact of finite measurement

area on a speckle pattern of given correlation area, see Ref. [50]. To reduce the effect of the pixel resolution on contrast, one would simply have to increase the ratio of the speckle correlation area to the CCD pixel area; this can be acheived by a few different methods: operate with a longer-wavelength beam, use a smaller slit aperture, or reduce the angular acceptance of each pixel.

The third contrast-reducing mechanism which may be present is the scattering of the beam during propagation from the sample to the detector. If the Kapton windows or the air in the flightpath scatter the beam appreciably, then bright speckles will have some of their intensity redistributed into the surrounding region. However, the use of thin Kapton films and the evacuation of air from 2.5 m of the 2.95 m sample-to-detector distance should make the scattering a small contribution to the loss of contrast in our measurements.

If the aperture area were to increase to infinity, one would expect the contrast to approach zero. The fit suggests a value of c somewhat above zero, and there are some possible reasons for this observation. Each image in the series is subject to a simliar level of noise due to counting statistics. The result is an artificial contribution to the contrast which is independent of aperture size. In addition, the area of each region over which $\sigma_I / \langle I \rangle$ was calculated has some contribution to the variance due only to the overall shape of the reflection. This effect cannot be easily avoided, since to make the reflection uniform over a large area would also increase the counting noise in the measurement. Some portion of the constant 9% contrast can be attributed to response nonuniformity of the CCD, which is claimed by the manufacturer to be $\leq$3%, excluding blemish regions [44].

The vertical slit size was consistently smaller than the coherence length in the vertical in this series, so the drop in contrast with increasing aperture area is predominantly due to the horizontal slit size exceeding the coherence length in that direction, which is approximately 5 μm.

3.4 Change in Speckle Shape and Orientation for Varying Diffraction Geometry

While measuring the coherent diffraction at the Cu_3Au (100) and (101) reflections, we had some freedom in choosing the diffraction geometry. As discussed in Section 2.5, this amounts to a rotation of the scattering plane about an axis parallel to the momentum transfer. When the momentum transfer vector, $\mathbf{q}$, is not parallel to the surface normal, $\hat{\mathbf{n}}$, it becomes possible to vary the incidence and exit angles, α_i and α_f. There are two consequences of such a variation. First, the active depth of the sample becomes small when either α_i or α_f approach zero. Second, the region of reciprocal space sampled by the CCD changes as the final scattering vector $\mathbf{k}_f$ is reoriented. The diffractometer program Spec was used to compute the diffractometer angles, and since those calculations are based on a user-specified azimuthal reference, there may be some error in setting the angles α_i and α_f. We specified an azimuthal reference of $\hat{\mathrm{n}} = (111)$, and thus the uncertainty in the incidence and exit angles is approximately 0.3°, which corresponds to the uncertainty of the miscut of the sample.

A striking feature of the series of CXD patterns for both (100) and (101) reflections was that the speckles became elongated into streaks as we approached the grazing exit condition. Also, the orientation of the streaks on the CCD varied as the diffraction geometry was changed. See Figures 3.7-3.14 and Figures 3.15-3.20. To change the diffraction geometry to vary α_i and α_f, the diffractometer angles θ, χ, and ϕ must be changed, which causes the sample to translate a few micrometers due to the irregularity of the ball bearings. As a result, the part of the sample which is illuminated for each of the measurements is not the same; therefore, the specific detail of the speckles in one measurement is not expected to be related to that of any other image. Since the statistical properties of the sample should not vary over the distance by which the sample translated, the statistical properties of the speckle

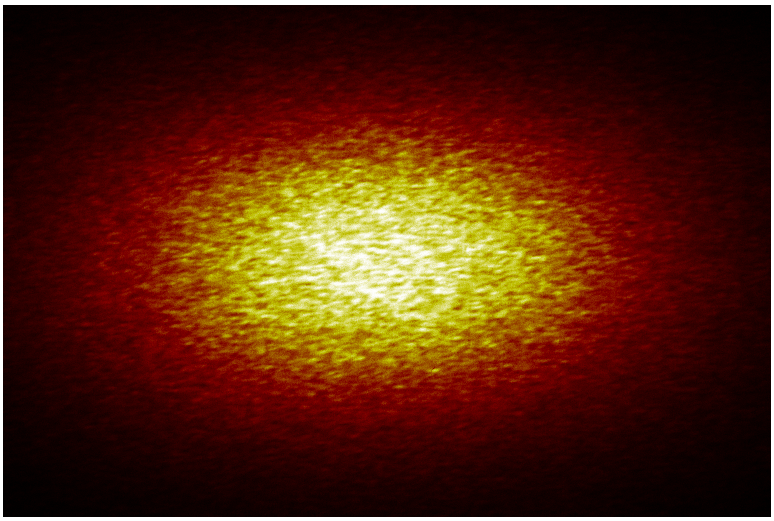

Figure 3.7: Cu_3Au (100) Bragg reflection at $\alpha_i = 1°$, $\alpha_f = 12.1°$. Shown is a 768×512 pixel region; the image is cataloged as `ID33_B57.SPE`, frame 1.

patterns can still be compared.

In order to analyze the shape and orientation of the speckles quantitatively, I computed the autocorrelation function for each frame. The two-dimensional autocorrelation function $f(\Delta x, \Delta y)$ of the (real-valued) intensity $I(x, y)$ with respect to the CCD x and y axes is defined

$$f(\Delta x, \Delta y) \equiv \int_{-\infty}^{\infty} \int_{-\infty}^{\infty} I(\xi, \eta) I^*(\xi - \Delta x, \eta - \Delta y)\, d\xi\, d\eta\,. \tag{3.9}$$

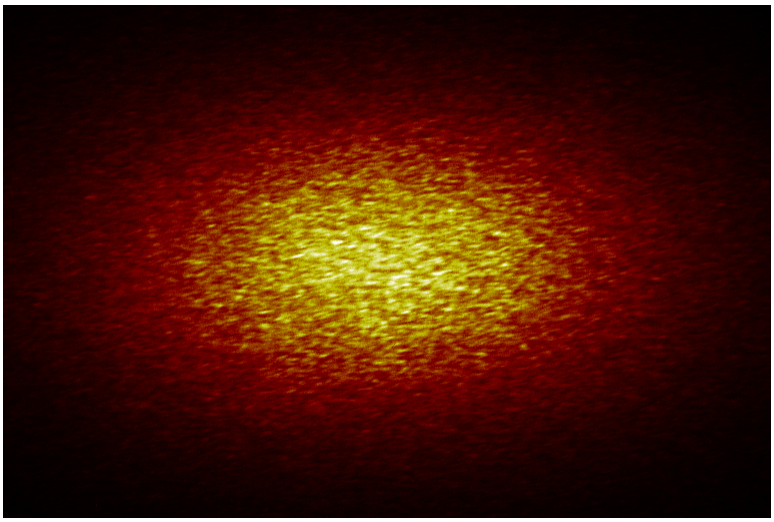

Figure 3.8: Cu_3Au (100) Bragg reflection at $\alpha_i = 2°$, $\alpha_f = 11.1°$. Shown is a 768×512 pixel region; the image is cataloged as `ID33_B57.SPE`, frame 2.

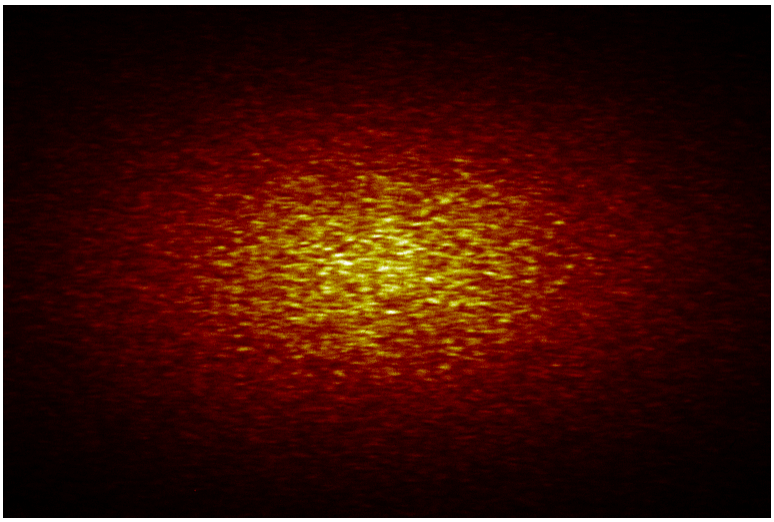

Figure 3.9: Cu_3Au (100) Bragg reflection at $\alpha_i = 4°$, $\alpha_f = 9.1°$. Shown is a 768×512 pixel region; the image is cataloged as `ID33_B57.SPE`, frame 3.

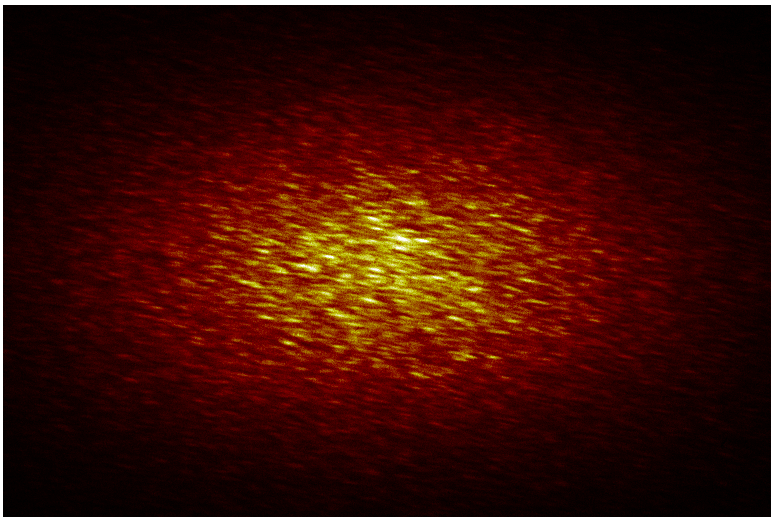

Figure 3.10: Cu_3Au (100) Bragg reflection at $\alpha_i = 6°$, $\alpha_f = 7.1°$. Shown is a 768×512 pixel region; the image is cataloged as `ID33_B57.SPE`, frame 4.

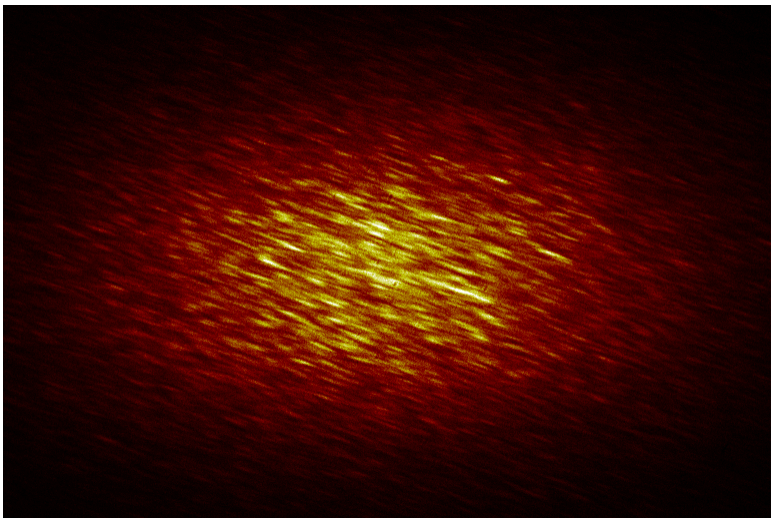

Figure 3.11: Cu_3Au (100) Bragg reflection at $\alpha_i = 8°$, $\alpha_f = 5.1°$. Shown is a 768×512 pixel region; the image is cataloged as `ID33_B57.SPE`, frame 5.

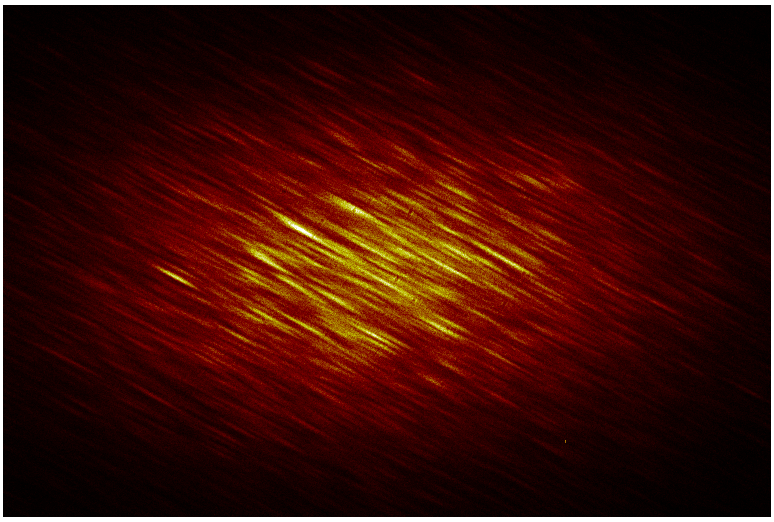

Figure 3.12: Cu_3Au (100) Bragg reflection at $\alpha_i = 10°$, $\alpha_f = 3.1°$. Shown is a 768×512 pixel region; the image is cataloged as `ID33_B57.SPE`, frame 6.

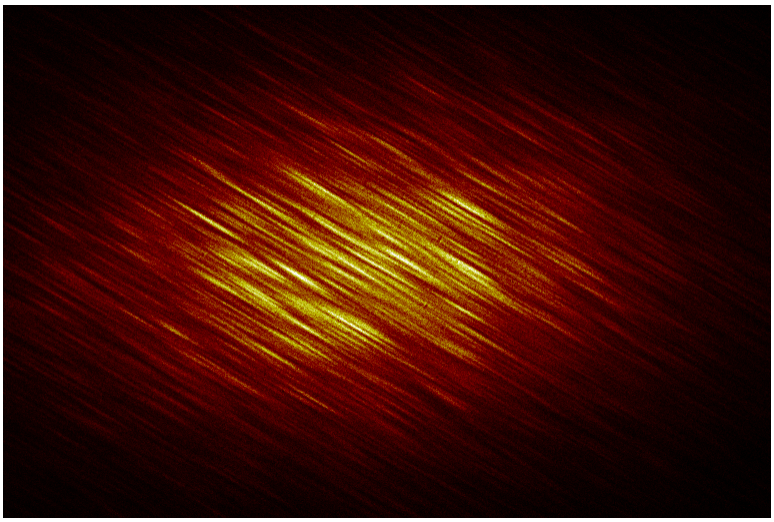

Figure 3.13: Cu_3Au (100) Bragg reflection at $\alpha_i = 11°$, $\alpha_f = 2.1°$. Shown is a 768×512 pixel region; the image is cataloged as `ID33_B57.SPE`, frame 7.

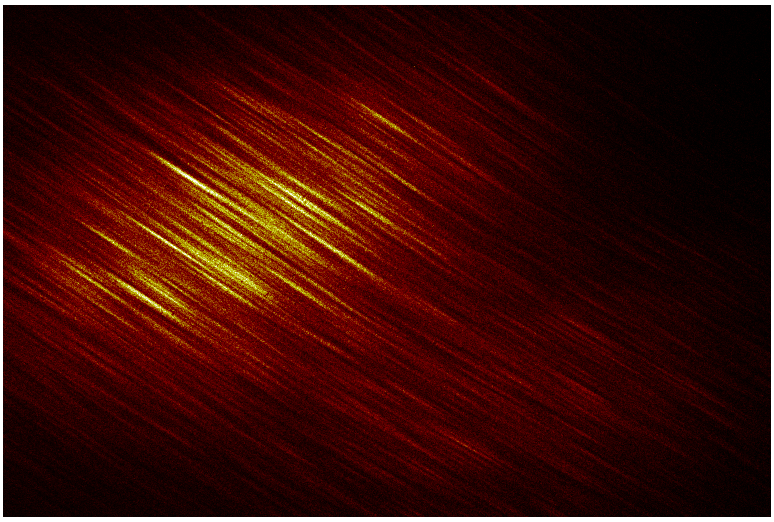

Figure 3.14: Cu_3Au (100) Bragg reflection at $\alpha_i = 12°$, $\alpha_f = 1.1°$. Shown is a 768×512 pixel region; the image is cataloged as `ID33_B57.SPE`, frame 8.

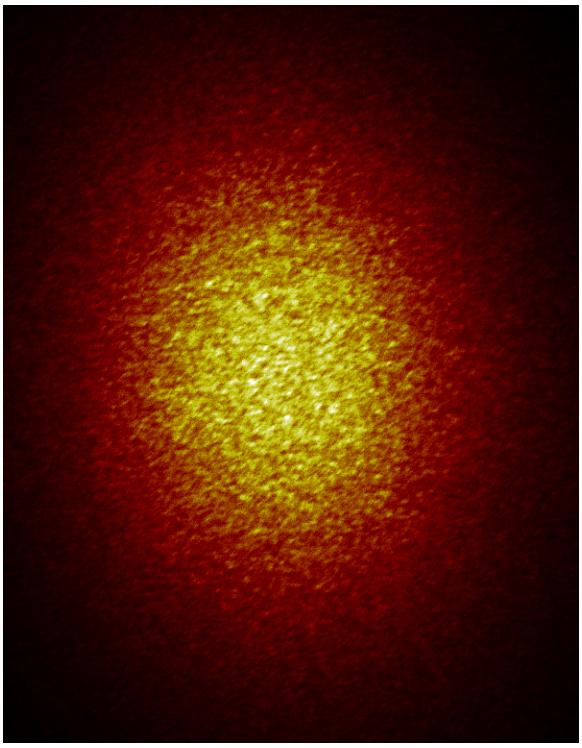

Figure 3.15: Cu_3Au (101) Bragg reflection at $\alpha_i = 3°$, $\alpha_f = 23.6°$. Shown is a 600×768 pixel region; the image is cataloged as `ID33_B59.SPE`, frame 18.

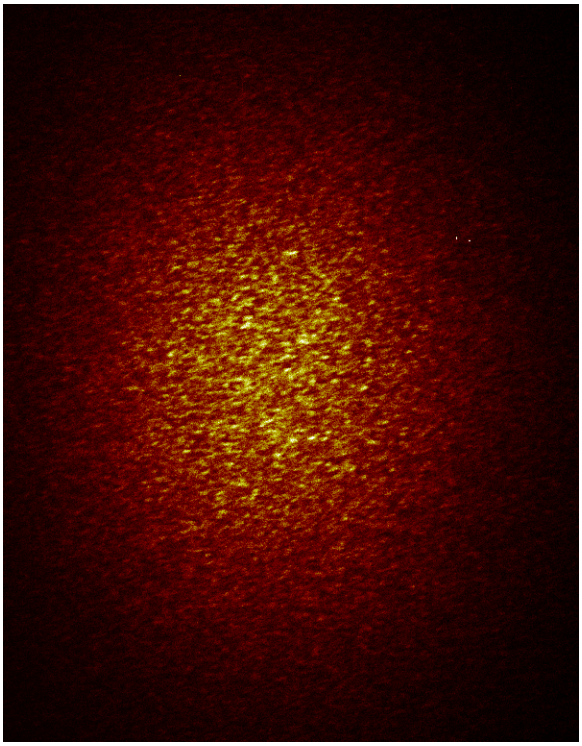

Figure 3.16: Cu_3Au (101) Bragg reflection at $\alpha_i = 7°$, $\alpha_f = 19.3°$. Shown is a 600×768 pixel region; the image is cataloged as `ID33_B59.SPE`, frame 12.

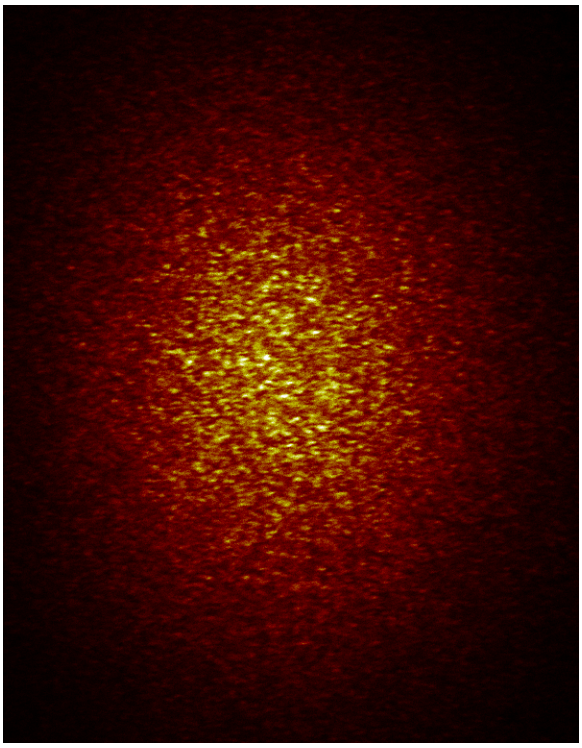

Figure 3.17: Cu_3Au (101) Bragg reflection at $\alpha_i = 9°$, $\alpha_f = 17.2°$. Shown is a 600×768 pixel region; the image is cataloged as `ID33_B59.SPE`, frame 7.

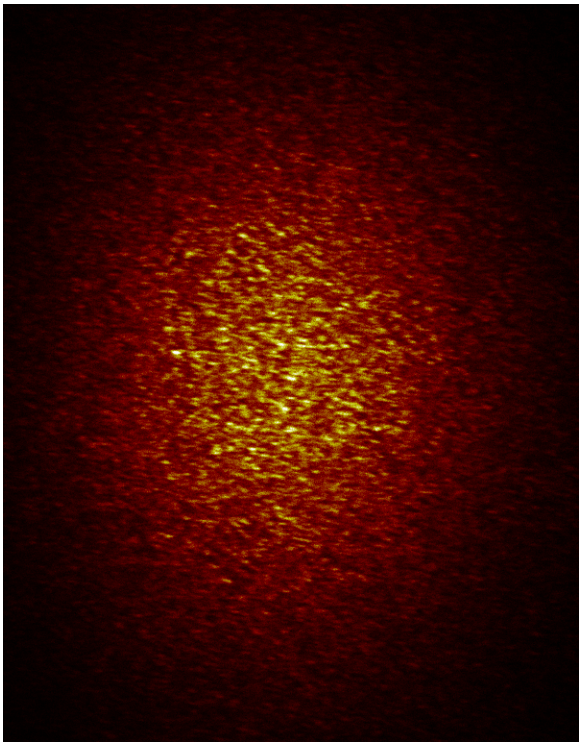

Figure 3.18: Cu_3Au (101) Bragg reflection at $\alpha_i = 11°$, $\alpha_f = 15.1°$. Shown is a 600×768 pixel region; the image is cataloged as `ID33_B59.SPE`, frame 6.

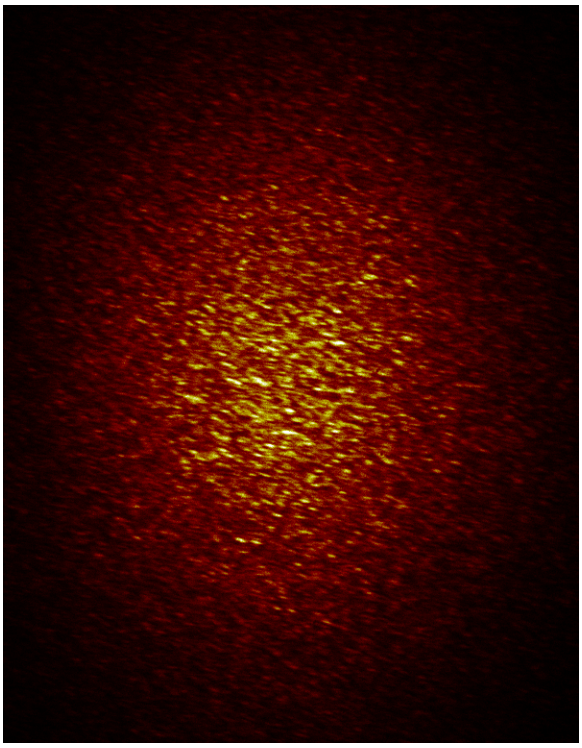

Figure 3.19: Cu_3Au (101) Bragg reflection at $\alpha_i = 13°$, $\alpha_f = 13.1°$. Shown is a 600×768 pixel region; the image is cataloged as `ID33_B59.SPE`, frame 1.

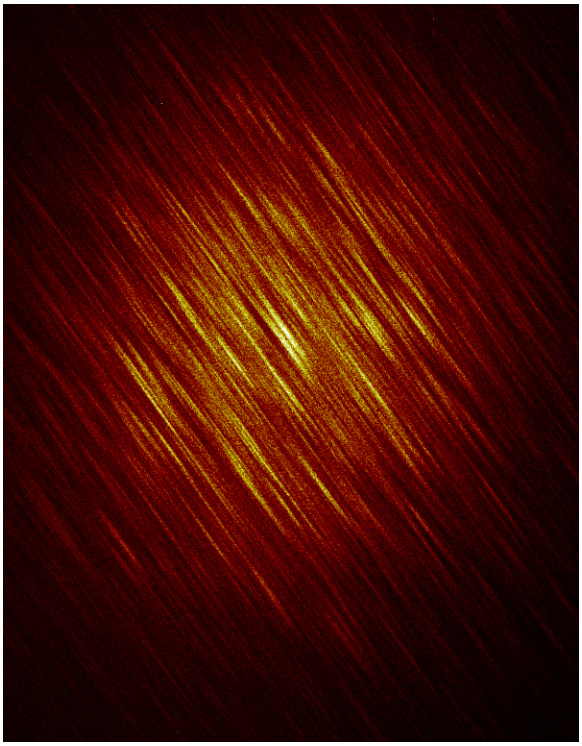

Figure 3.20: Cu_3Au (101) Bragg reflection at $\alpha_i = 25°$, $\alpha_f = 1.7°$. Shown is a 600×768 pixel region; the image is cataloged as `ID33_B60.SPE`, frame 1.

The autocorrelation function for discrete data is conveniently computed using the FFT because of the autocorrelation theorem, which states that for any analytic function $h(x, y)$,

$$\mathcal{F}\left[\int_{-\infty}^{\infty}\int_{-\infty}^{\infty} h(\xi,\eta)h^*(\xi-\Delta x,\eta-\Delta y)\,d\xi\,d\eta\,.\right] = |H(q_x,q_y)|^2\ , \tag{3.10}$$

where $H = \mathcal{F}(h)$ and the q_x and q_y are the reciprocal-space variables corresponding to x and y. The autocorrelation functions consisted of two peaks, both centered at the origin. The first, very broad and approximately the same shape as the incoherently illuminated peaks of Figures 3.1 and 3.2, results from the random correlations of separated speckles and from the incoherent contribution to the intensity. These broad peaks do have some structure, most notably the long "trenches" in the frames obtained at grazing exit where the speckles are very elongated. The reason for such structure could be that the speckles are not completely random in position, or the structure may simply result from the finite size of the whole speckle pattern over which the autocorrelation function is computed. The second peak, of a size and orientation characteristic of the speckles in the image, arises from the internal correlations within each speckle. This second peak is taken to represent a "typical" speckle in the following discussion. Since the speckles themselves encode information about the specific arrangement of antiphase domains in the sample, their shapes, sizes, and orientations are expected to vary somewhat within a given speckle pattern. The "typical" speckle obtained from the autocorrelation function is thus to be regarded as representative of the whole speckle pattern, and all speckles do not have precisely the same properties.

In a way similar to that of Section 3.2, the autocorrelation functions were fit to a sum of two elliptical Gaussians, with no constant background term. As shown in Figures 3.21-3.34, the two-elliptical-Gaussian model reproduces the behavior of the autocorrelation functions well. It is clear from the plots that the shape and orientation of the small central peak changes systematically with α_i and α_f.

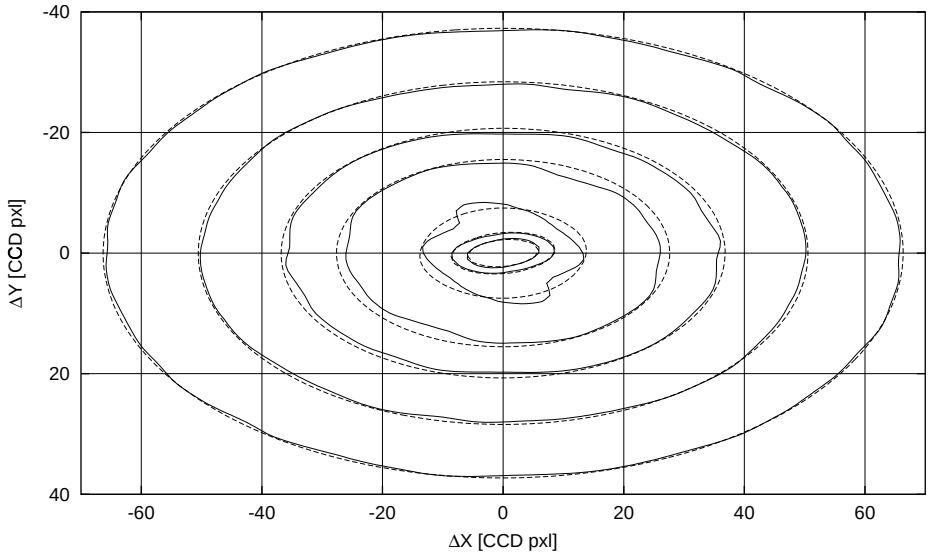

Figure 3.21: Fit to unscaled autocorrelation function of Figure 3.7. The contour levels are 5.1×10^5, 5.25×10^5, 5.35×10^5, 5.4×10^5, 5.45×10^5, 5.475×10^5, and 5.5×10^5 (ADC units)^2. In this plot and the following, the autocorrelation functions are plotted with solid lines, and the elliptical Gaussian fits are plotted with dashed lines.

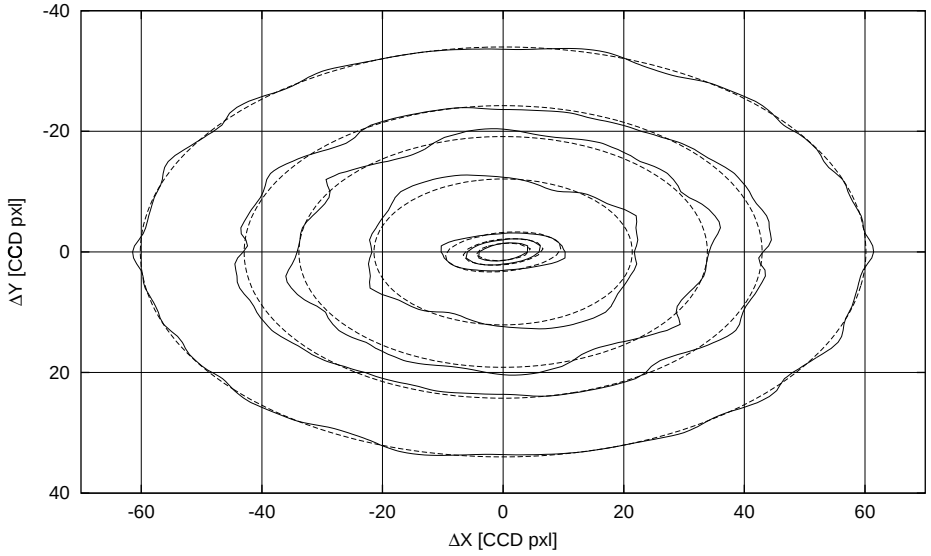

Figure 3.22: Fit to unscaled autocorrelation function of Figure 3.8. The contour levels are 8.75×10^4, 9×10^4, 9.1×10^4, 9.2×10^4, 9.3×10^4, 9.4×10^4, and 9.5×10^4 (ADC units)^2.

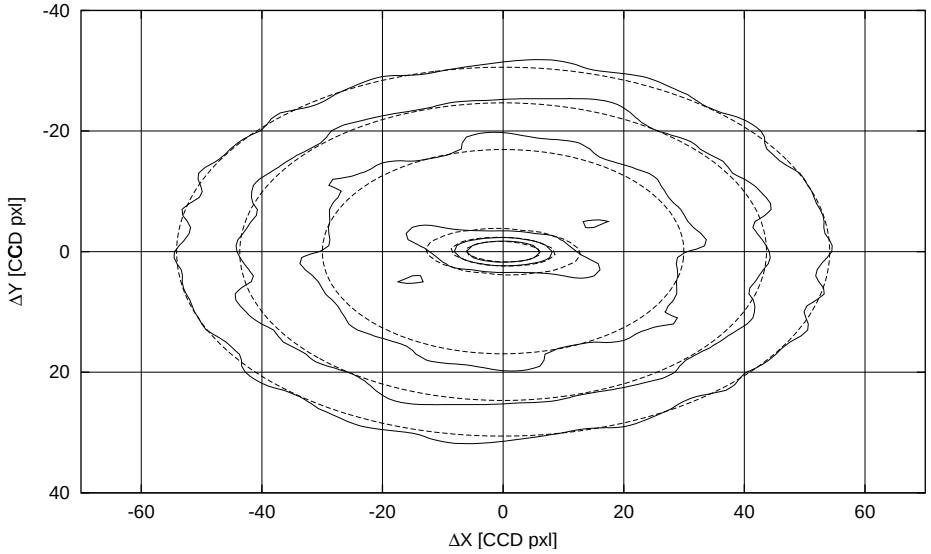

Figure 3.23: Fit to unscaled autocorrelation function of Figure 3.9. The contour levels are 6100, 6200, 6300, 6400, 6500, and 6600 (ADC units)^2.

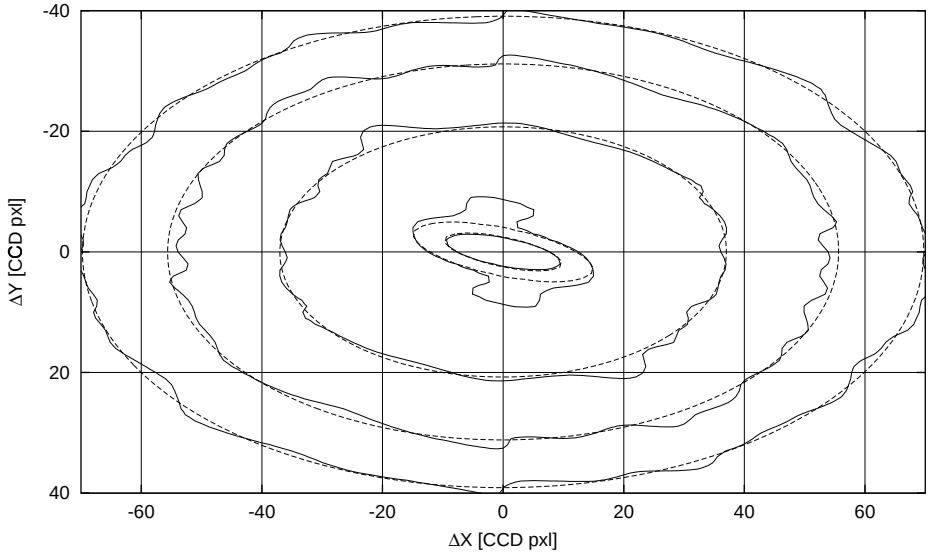

Figure 3.24: Fit to unscaled autocorrelation function of Figure 3.10. The contour levels are 925, 950, 975, 1000, and 1025 (ADC units)^2.

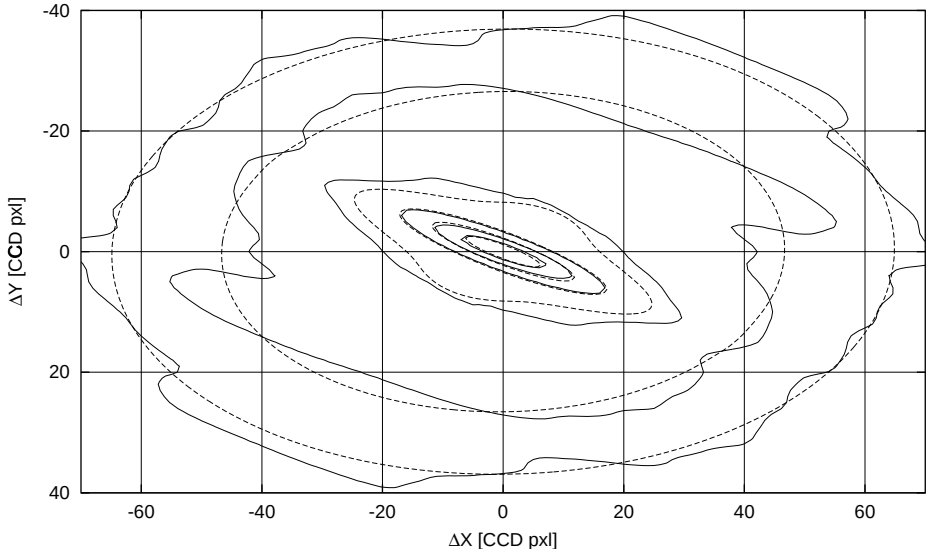

Figure 3.25: Fit to unscaled autocorrelation function of Figure 3.11. The contour levels are 350, 360, 370, 380, 390, and 400 (ADC units)^2.

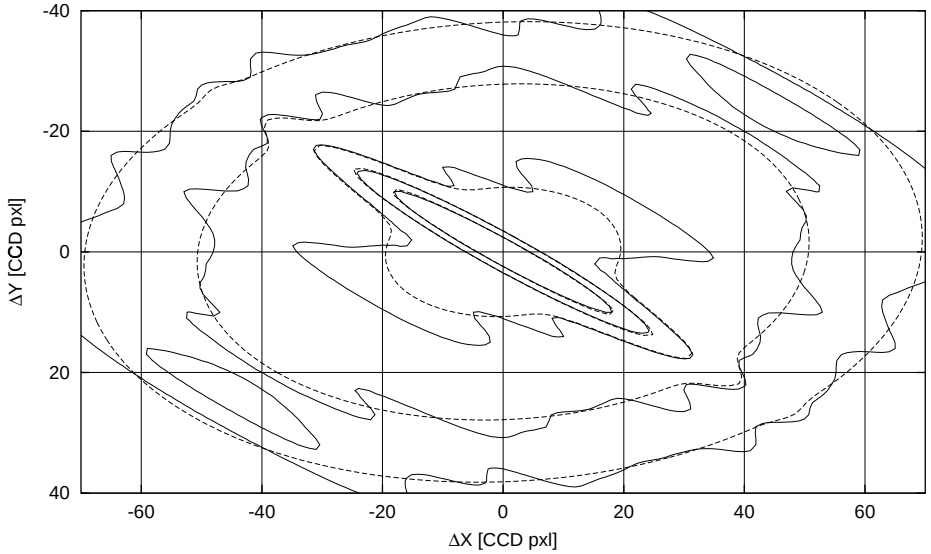

Figure 3.26: Fit to unscaled autocorrelation function of Figure 3.12. The contour levels are 170, 175, 180, 185, and 190 (ADC units)^2.

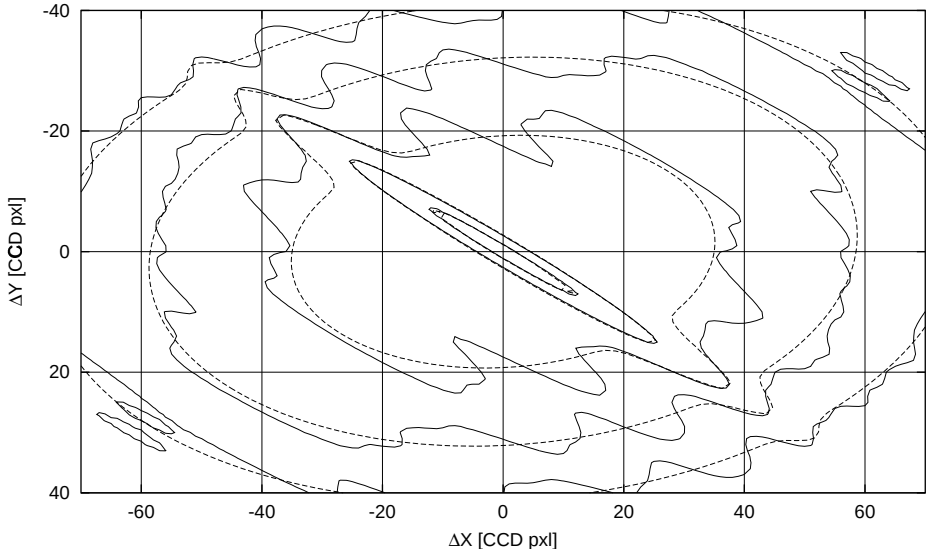

Figure 3.27: Fit to unscaled autocorrelation function of Figure 3.13. The contour levels are 54, 55.5, 57, 60, and 63 (ADC units)^2.

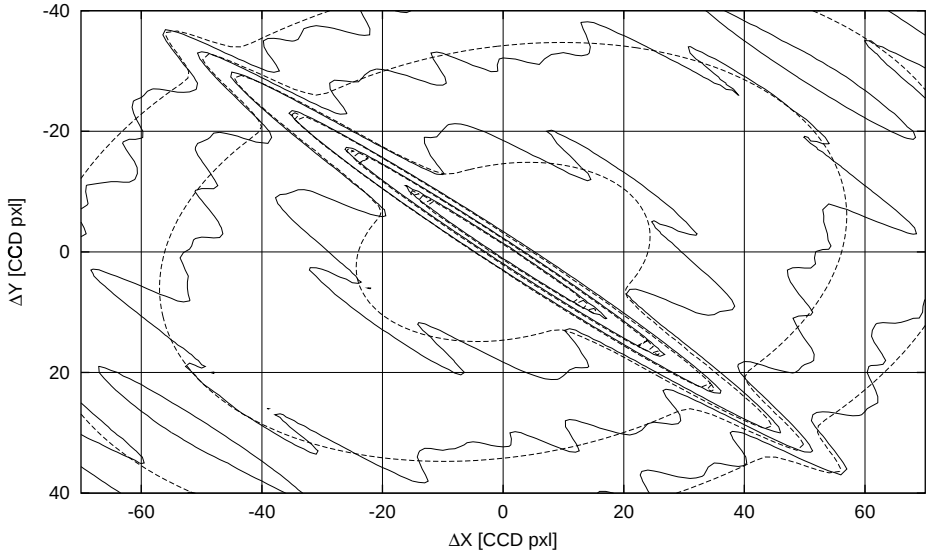

Figure 3.28: Fit to unscaled autocorrelation function of Figure 3.14. The contour levels are 2.2, 2.25, 2.3, 2.4, 2.5, and 2.6 (ADC units)^2.

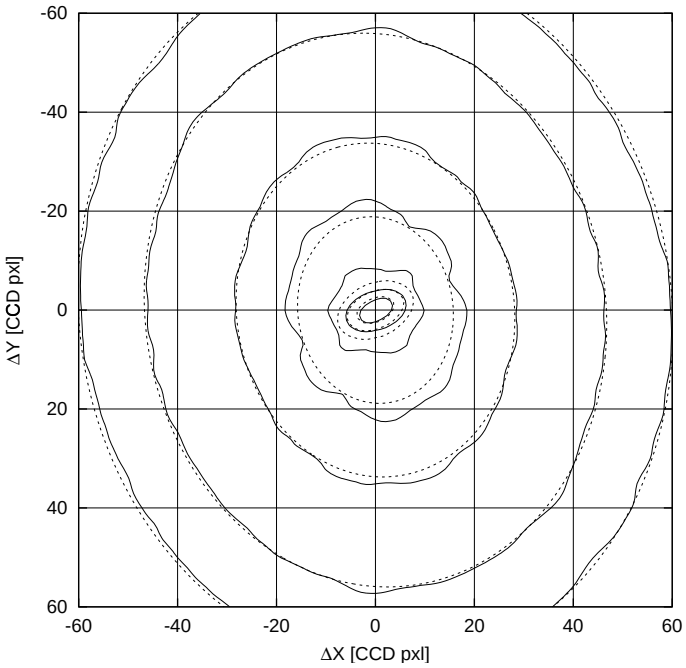

Figure 3.29: Fit to unscaled autocorrelation function of Figure 3.15. The contour levels are 17000, 17500, 18000, 18200, 18300, 18400, and 18600 (ADC units)^2.

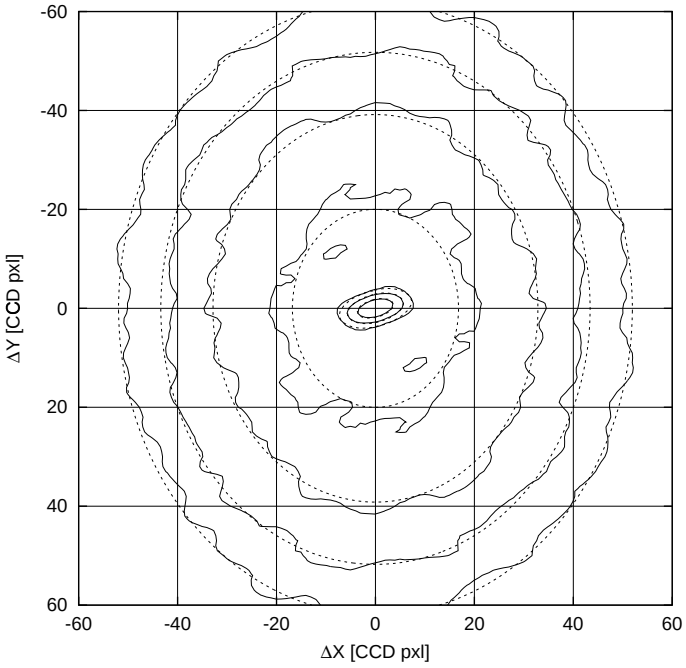

Figure 3.30: Fit to unscaled autocorrelation function of Figure 3.16. The contour levels are 9.9, 10, 10.1, 10.2, 10.3, 10.4, and 10.6 (ADC units)^2.

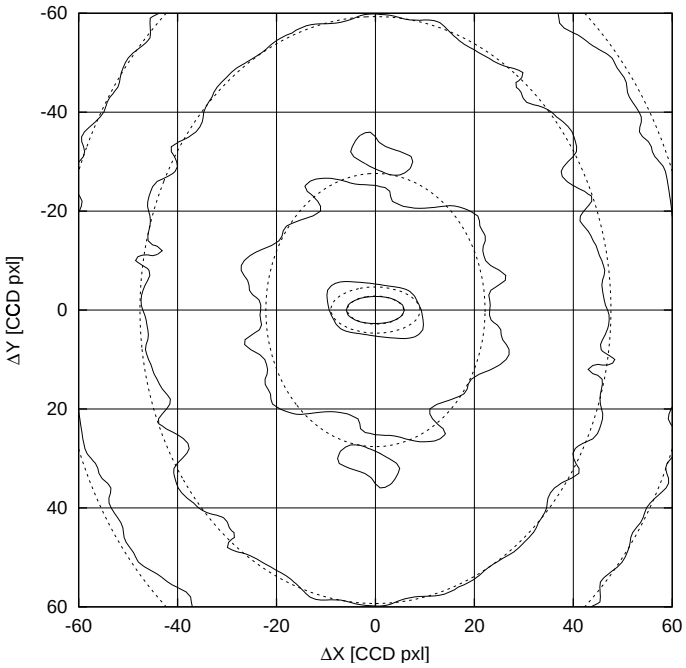

Figure 3.31: Fit to unscaled autocorrelation function of Figure 3.17. The contour levels are 675, 700, 725, 735, and 755 (ADC units)^2.

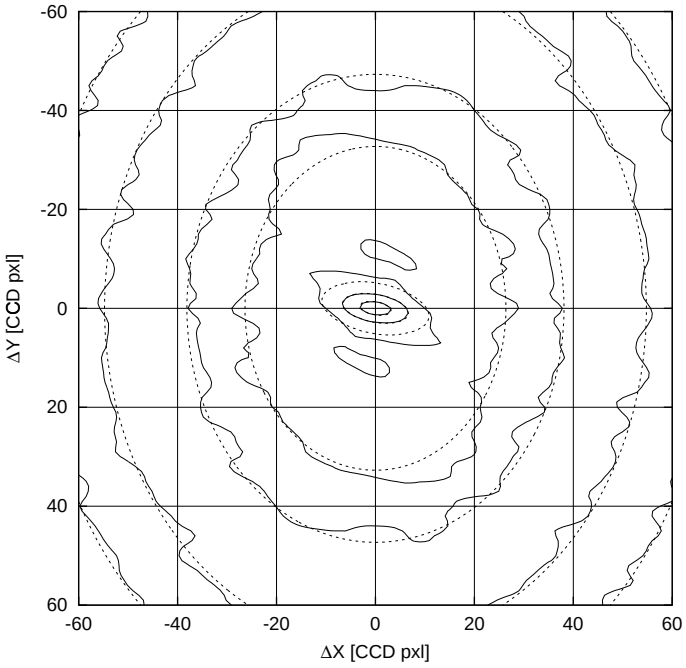

Figure 3.32: Fit to unscaled autocorrelation function of Figure 3.18. The contour levels are 290, 300, 310, 320, 330, 340, 350, 355, 360, 370, and 390 (ADC units)^2.

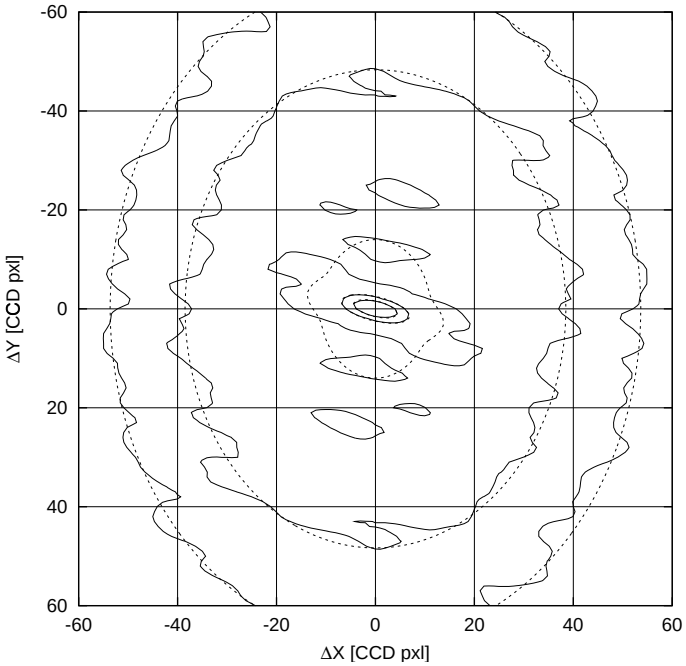

Figure 3.33: Fit to unscaled autocorrelation function of Figure 3.19. The contour levels are 850, 875, 900, 950, and 1000 (ADC units)^2.

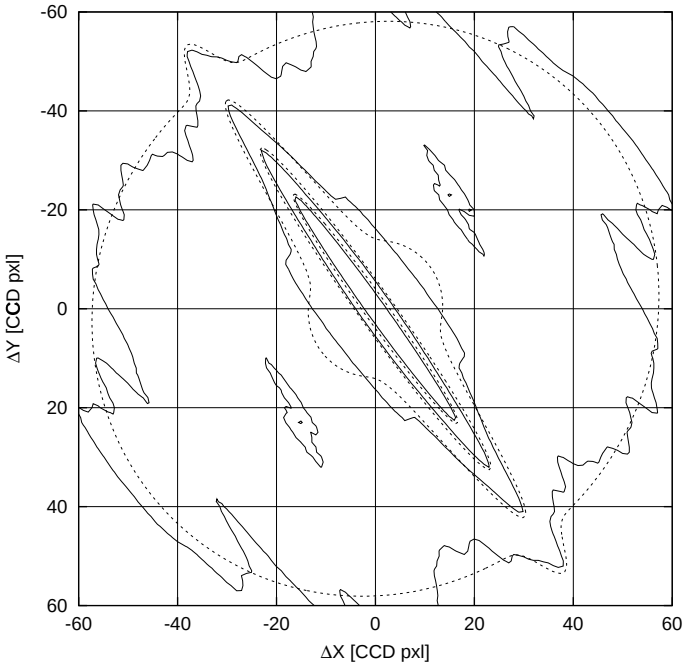

Figure 3.34: Fit to unscaled autocorrelation function of Figure 3.20. The contour levels are 4.8, 4.9, 5, and 5.1 (ADC units)^2. This plot clearly shows the "trenches" in the broad peak of the autocorrelation function.

To understand the behavior we observed, one must have a clear picture of the reciprocal-space intensity structure of the illuminated volume of Cu_3Au and of the sampling of this structure under quasi-monochromatic conditions by an area detector. The sample had a (111) orientation, and the effective illuminated depth of the sample was of a much smaller scale than the size of the beam footprint. According to the discussion of Subsection 1.3.2, the intensity should then have very little modulation in the surface normal direction $\hat{\mathbf{n}}$ and much more structure in the in-plane directions. As a result, the superstructure Bragg reflection takes on the form of a bundle of rods oriented along $\hat{\mathbf{n}}$. This structure is then sampled on a patch of the Ewald sphere approximated by a plane with its surface normal along $\mathbf{k}_f$. As the exit angle $\mathbf{k}_f$ approaches zero, $\mathbf{k}_f$ becomes nearly perpendicular to $\hat{\mathbf{n}}$, and the sampling amounts to cutting the rods along their length, resulting in the long streaks seen at the detector. Away from grazing exit, another effect becomes important. The size of the rods in reciprocal-space units is of the same order of magnitude as the spread in the beam wavenumber k. As a result, to model the image formed on the detector requires convolution of the monochromatic image with the beam spectrum, as discussed in Section 2.6.

In order to confirm the above interpretation of the observed behavior of the speckles, I calculated the formation of an image of an ideal rod of intensity passing through the reciprocal-space point $\mathbf{q}_0$ with its axis along $\hat{\mathbf{n}}$. The rod was taken to have the form of a cylindrical Gaussian:

$$I(\mathbf{q}) \equiv \exp\left\{-\frac{1}{2\sigma_{\text{rod}}^2}\left|\mathbf{q}-\mathbf{q}_0-\left[\hat{\mathbf{n}}\cdot(\mathbf{q}-\mathbf{q}_0)\right]\hat{\mathbf{n}}\right|^2\right\}, \tag{3.11}$$

where the quantity $|\mathbf{q}-\mathbf{q}_0-[\hat{\mathbf{n}}\cdot(\mathbf{q}-\mathbf{q}_0)]\,\hat{\mathbf{n}}|$ is the distance from the point $\mathbf{q}$ to the axis of the rod. Then, using *Mathematica* [51], I solved for the scattering vectors $\mathbf{k}_i$ and $\mathbf{k}_f$ under a set of conditions. The first condition,

$$|\mathbf{k}_i| = |\mathbf{k}_f| = k\,, \tag{3.12}$$

enforces elastic scattering with a wavenumber k. The second condition,

$$\mathbf{k}_f - \mathbf{k}_i = \left(\frac{k}{k_0}\right)\mathbf{q}_0\,, \tag{3.13}$$

requires that the scattering of the beam from the incident wavevector to the final wavevector imparts a momentum transfer which lies along the same direction as the $\mathbf{q}_0$ set by the diffractometer for the wavenumber k_0 but is scaled by the ratio k/k_0. The final two conditions are that the incident beam enters the surface at an angle α_i and that the scattered beam exits the surface at an angle α_f:

$$\mathbf{k}_i \cdot \hat{\mathbf{n}} = -k\sin\alpha_i, \quad \mathbf{k}_f \cdot \hat{\mathbf{n}} = k\sin\alpha_f\,. \tag{3.14}$$

Since we have two equations from 3.12, three from 3.13, and two from 3.14, but only the six unknowns making up $\mathbf{k}_i$ and $\mathbf{k}_f$, the problem is overdetermined. By combining the above conditions, one can find α_f for a given α_i:

$$\alpha_f = \arcsin\left[\frac{1}{k_0}\left(\mathbf{q}_0 \cdot \hat{\mathbf{n}}\right) - \sin\alpha_i\right]\,. \tag{3.15}$$

At a given reflection, $\mathbf{q}_0$ and $\hat{\mathbf{n}}$ are both constants. The relationship between α_i and α_f for the (100) and (101) reflections, for the case of an 8.5 keV beam, is shown in Figure 3.35. Some error in the experimental values of α_i and α_f is possible due to diffractometer misalignment, miscut of the sample, or uncertainty in the beam energy.

After obtaining $\mathbf{k}_i$ and $\mathbf{k}_f$ for a set of α_i, I then computed the unit vectors associated with the axes of the CCD:

$$\begin{aligned}\hat{\mathbf{y}} &= \frac{k^2\mathbf{q}_0 - \left(\mathbf{k}_f \cdot \mathbf{q}_0\right)\mathbf{k}_f}{\left|k^2\mathbf{q}_0 - \left(\mathbf{k}_f \cdot \mathbf{q}_0\right)\mathbf{k}_f\right|} \\ \hat{\mathbf{x}} &= \frac{\mathbf{k}_f \times \hat{\mathbf{y}}}{k}\,.\end{aligned} \tag{3.16}$$

Note that the expression for $\hat{\mathbf{y}}$ is independent of k, since $|\mathbf{k}_f| = k$. Using the set of $\mathbf{k}_i$, $\mathbf{k}_f$, $\hat{\mathbf{x}}$, and $\hat{\mathbf{y}}$ obtained by solving the system of diffractometer equations, I constructed a function $I(x, y; k)$ which models the intensity recorded on a simulated CCD array at pixel (x, y) at a given wavenumber k. The convolution of $I(x, y; k)$ with a Gaussian

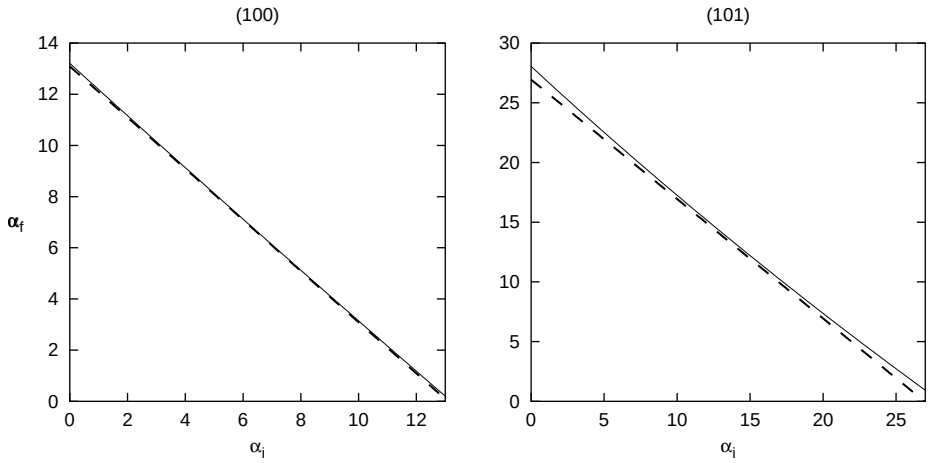

Figure 3.35: α_f vs. α_i for the (100) and (101) reflections. The relation according to Equation 3.15 is plotted with the solid curve; the dashed line in each plot is $(\mathbf{q}_0 \cdot \hat{\mathbf{n}})/k_0 - \alpha_i$.

k distribution was performed in *Mathematica* using a weighted sum of images with 17 values of k. The resulting images were then treated as "data" and fit to a single elliptical Gaussian, yielding a set of simulated speckle dimensions and orientations for comparison with the observations.

After some optimization to best reproduce the dimensions of the observed speckles, I obtained a rod radius $\sigma_{\text{rod}} \approx 2.5 \times 10^{-5}$ Å^{-1}, which corresponds to a beam footprint size of ~ 11 μm. Manual optimization was necessary, since the calculations were too lengthy for fitting. The energy spectrum of the beam was modelled as a Gaussian, and the best results were found with a FWHM of $(1.9 \times 10^{-4})k_0$, where k_0 is the mean wavenumber of the distribution. This agrees well with the known Δk spread of a Si(111) monochromator, which is usually stated to be about $(2 \times 10^{-4})k_0$. Figure 3.36 compares the characteristics of the model speckles with the observed speckle autocorrelation functions. The simulation clearly agrees very well with the observed streak orientation at grazing exit (near $\alpha_f = 0$). In this regime, the geometrical effect of sampling reciprocal space dominates, and the model is not as sensitive to the shape of the rod or to the form of the beam energy spectrum as it is away from grazing exit. The sigma-widths of the major and minor axes of the simulated speckles agree well

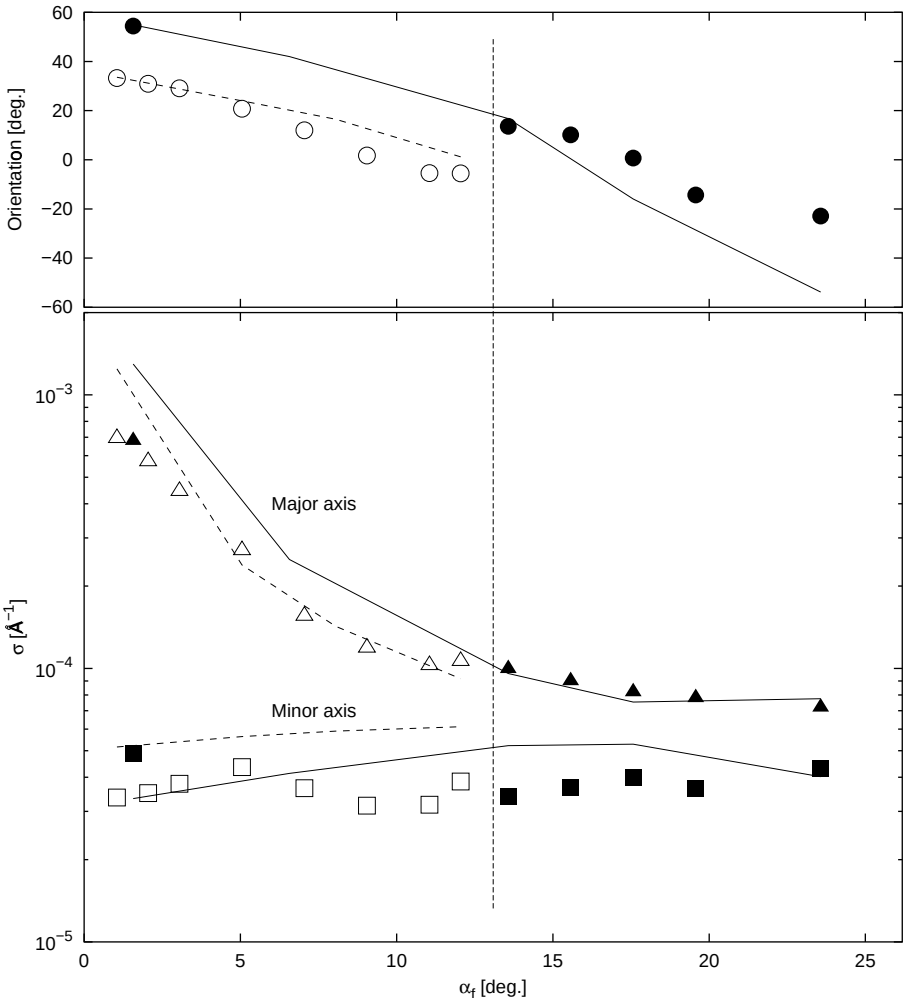

Figure 3.36: Variation of the simulated speckles with diffraction geometry compared to observation. Open symbols and dashed lines represent the (100) reflection, while filled symbols and solid lines correspond to the (101) reflection. The upper panel shows the angular orientation of the fitted elliptical Gaussians, and the lower panel shows the sigma-width of the major and minor axes. The left and right edges of the plot correspond to perfectly grazing exit and incidence, respectively, for the (101) reflection. The dashed line at $\alpha_f = 13.09°$ indicates the grazing incidence condition for the (100) reflection.

with those of the autocorrelation functions of the measured speckles. The agreement on the orientation angle is not as good approaching grazing incidence (large α_f) for the (101) reflection. This might be due to the limitations of the Gaussian model used for the energy distribution. The model tends to overestimate the major-axis length of the speckles near grazing exit; the likely cause is that the model consists of rods of infinite length, while the true structure may have modulation along the rod direction and certainly will have a limited extent. The flat behavior of the minor-axis length is well reproduced by the model.

The model presented here has only two fitting parameters, σ_{rod} and the FWHM of the energy distribution, yet it does reproduce the orientation and shape of the observed speckles well. This makes a strong confirmation that the CXD patterns we measured are well described by the bundle-of-rods model for the reciprocal-space structure of a thin slab of Cu_3Au along with the Ewald construction modified for the case of a quasi-monochromatic beam and an area detector. According to this model, it is in principle possible to measure the entire three-dimensional reciprocal-space structure of the scattering volume by sweeping the energy only—without any movement of the sample, source, or detector as is done in tomography.

If the intensity can be characterized as rods along the surface normal direction, then the scattering can be described by an alternative picture, that of a phase-modulating mirror. The streaked character of the speckles near grazing exit can still be explained by noting that the diffracted beam is compressed in the surface normal direction as it exits the sample. This wavefront, which subsequently propagates to the detector via the Fourier transform after interaction with the sample, has an envelope with a much smaller extent in the surface normal direction than in the direction lying in the plane of the surface. Thus, the smallest features in the diffraction, the speckles, will be much longer along the surface normal direction than along the direction perpendicular. It can be seen that near grazing exit, the orientations of

the streaks on the CCD do lie along the projected surface normal direction. At the (100) reflection the surface normal makes an angle

$$90^\circ - \arccos\left[\frac{\mathbf{b}_1 \cdot (\mathbf{b}_1 + \mathbf{b}_2 + \mathbf{b}_3)}{\sqrt{b_1^2}\sqrt{b_1^2 + b_2^2 + b_3^2}}\right] \approx 35.3^\circ \tag{3.17}$$

with the horizontal; at the (101) reflection, this angle is

$$90^\circ - \arccos\left[\frac{(\mathbf{b}_1 + \mathbf{b}_3) \cdot (\mathbf{b}_1 + \mathbf{b}_2 + \mathbf{b}_3)}{\sqrt{b_1^2 + b_3^2}\sqrt{b_1^2 + b_2^2 + b_3^2}}\right] \approx 54.7^\circ. \tag{3.18}$$

Clearly, according to this view, streaks do not appear unless the diffracted beam is made smaller in one direction than in the other.

Another type of measurement which can be interpreted in terms of a phase-modulating mirror is coherent x-ray specular reflectivity, or surface speckle [52–55]. Figure 3.37 shows a series of example images of surface speckle. The phase modulation in this type of experiment results from dips in the morphological height of the surface advancing the phase relative to a reference phase from some average surface and retarding the phase where the surface has a mound. Surface speckle, in contrast to CXD from a Bragg reflection at much larger q, has an envelope which is very nearly one-dimensional. This happens because the phase modulation, assumed to be isotropic in the plane of the surface, is foreshortened as viewed from the detector, causing a phase modulation in the beam on a much smaller length scale in one direction than in the direction perpendicular. The Fourier transform of such a system has a large number of speckles splayed out in the foreshortened direction. Such speckle patterns can be treated as one-dimensional in nature, which contrasts with the two-dimensional character of the thin-slab Cu_3Au CXD shown here, or the three-dimensional information obtained in CXD with samples having structure in three dimensions. We gained much of our experience with phase retrieval techniques by applying them to one-dimensional speckle patterns of this kind [52–55]. Reconstructing real-space information from the measured one-, two-, or three-dimensional speckle measurements described here requires some means of retrieving the phase of

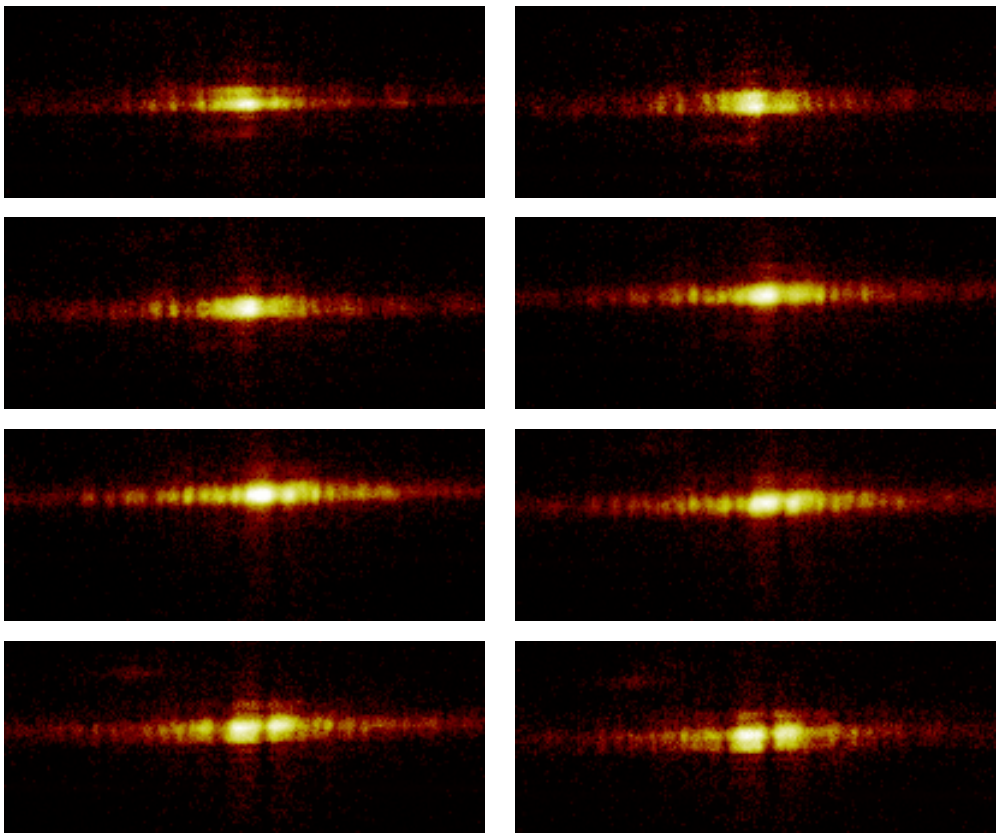

Figure 3.37: Speckle in coherent reflectivity of a SiGe surface at $q = 0.060$ Å^{-1}. The images show an 80×200 pixel region from a series in which the horizontal position of the roller-blade slits was stepped by 5 μm between acquisitions. The scattering was vertical, and the images are shown here rotated by 90° counterclockwise. Each frame results from three accumulations of 40 s each. The data are cataloged as frames 2, 4, ..., 16, in the file `J99_108.SPE`.

the diffracted beam. The most successful iterative methods for phase retrieval form the basis for Chapter 4.

Chapter 4

Phase Retrieval

4.1 Introduction

CXD leads naturally to a classic inverse problem: given an intensity measurement in reciprocal space, $|F(\mathbf{q})|^2$, possibly along with some additional information, reconstruct its real-space inverse Fourier transform $f(\mathbf{x})$. The reconstruction of f would be trivial if both the amplitude and phase of F were measured, as a simple inverse Fourier transform would yield f directly; however, in CXD experiments it is not generally possible to measure the phase of F. This "phase problem" has been addressed by a large number of investigators in such diverse fields as protein crystallography, radio astronomy, radar, computer vision, and optics. The classic way to solve the phase problem, holography, is to interfere the diffracted beam with a reference wave [56]. This has been applied to x-ray diffraction by using the fluorescence of an atomic species within the sample as the reference wave [57–59]. Some methods used regularly by protein crystallographers, such as isomorphous replacement [60; 61] and anomalous dispersion [62], do provide some partial phase information. Solving structures using data obtained with these techniques still typically requires *a priori* information regarding the molecular structure, which is subsequently refined iteratively subject to the measurement. A more recent development is the two-beam diffraction inter-

ference method, which arranges for two coherent non-colinear incident x-ray beams diffracting into a common exit direction to interfere and thus make the difference in their phases measureable. This method is applicable to two-dimensional periodic structures such as the surfaces and interfaces of crystalline materials and to systems with unit cells larger than about 80 Å [63; 64].

The phase retrieval methods of this chapter can be applied to systems in which the sample modulates the amplitude or the phase of the incident beam. In general, the algorithms work by asserting the reciprocal-space amplitude obtained experimentally and also enforcing some known real-space properties. Because, in our case, the sample is illuminated by a well-defined set of slits, the amplitude and phase of the illumination envelope at the sample can be calculated. This must be done using Fresnel integrals, as the slit-to-sample distance does not place the sample in the far field. The calculation could be further guided by direct-beam measurements of the Fraunhofer diffraction from the slits, as shown in Figure 2.6, so that the asymmetry of the slits can be modelled. The beam, having propagated from the slits to the sample according to Fresnel diffraction, interacts with the sample and, as a result, the wavefront of the beam just after interaction with the sample is modified. For the case of specular reflection from a surface or of superstructure Bragg reflection from Cu_3Au, the amplitude of the wavefront is unmodified by the sample, but the phase of the beam is changed.

If the beam impinging on the sample has a wavefront of the form

$$\tilde{a}_0(x,y) = a(x,y)e^{i\phi_0(x,y)}\,, \tag{4.1}$$

where x and y are the horizontal and vertical coordinates of the beam, $a(x,y) = |\tilde{a}(x,y)|$ is the real-valued amplitude of the wavefront, and $\phi_0(x,y)$ is the phase due to the Fresnel diffraction from the slits, then the wavefront after reflecting from the

sample is described by the function

$$\tilde{a}(x,y) = a(x,y)e^{i[\phi_0(x,y)+\phi(x,y)]}\,. \tag{4.2}$$

Here, the function $\phi(x,y)$ is the contribution to the phase of the beam due to the sample. According to the model of the sample as a phase object, the amplitude $a(x,y)$ is unchanged. Finally, the beam propagates to the detector via the Fourier transform to give the complex amplitude

$$\tilde{A}(q_x,q_y) = A(q_x,q_y)e^{i\Phi(x,y)} = \int_{-\infty}^{\infty}\int_{-\infty}^{\infty} a(x,y)e^{i[\phi_0(x,y)+\phi(x,y)]}e^{i(q_x x+q_y y)}dx\,dy\,. \tag{4.3}$$

Speckle measurements give the intensity $I(q_x,q_y) = [A(q_x,q_y)]^2$. Iterative phase retrieval methods, such as the Gerchberg-Saxton algorithm and the Hybrid Input-Output (HIO) algorithm, seek to recover the phase $\Phi(q_x,q_y)$, so that by an inverse Fourier transform, the real-space phase $\phi(x,y)$ due to the sample interaction can be obtained. We are aided by the *a priori* knowledge of the real-space illumination $a(x,y)$ and the Fresnel phase $\phi_0(x,y)$.

4.2 Uniqueness

A critical issue to address regarding the phase problem is the uniqueness of the solution. For example, if f is a solution to the phase problem such that $\mathcal{F}(f) = F$ and the measured intensity I has the value $|F|^2$, then the solution f is unique if and only if no other function g exists such that $|\mathcal{F}(g)|^2 = I$. In other words, uniqueness of the solution f requires that no other function g exists which cannot be distinguished from f based on observation of I. If, as is the case under consideration here, there is *a priori* knowledge of the amplitude $|f|$, then any alternate solution g must satisfy $|g| = |f|$.

An infinite set of alternate solutions can in fact be constructed from any solution $f(x,y)$ in the following ways, some of which are trivial. First, a constant phase shift $e^{i\theta}$

gives a solution $\left|\mathcal{F}[e^{i\theta}f(x,y)]\right|^2 = I(q_x,q_y)$. Thus, a measurement of speckle intensity cannot distinguish between two solutions related by a constant phase shift. A second class of alternate solutions is found by noting that $|\mathcal{F}[f^*(-x,-y)]|^2 = I$. Alternate solutions of this form are referred to as "duals" or "twin images." Dual solutions have been associated with stagnation problems for phase retrieval algorithms in the literature and in holography in general; intermediate image estimates can take on features of both a solution and its dual, and cause the algorithms to fail to converge or to converge very slowly [65]. Note that a linear combination, $t\,f(x,y) + (1-t)\,f^*(-x,-y)$, is not a solution because superposition does not apply to the square modulus, so that the error metric for such a function remains higher than that for f or its dual. The problem of dual solutions can be avoided by ensuring that the illumination of the sample is not centrosymmetric in the experiment. Another possible ambiguity in the phase retrieval problem arises when the origin of reciprocal space is not precisely known in the measurement. An offset of $(\delta q_x, \delta q_y)$ in reciprocal space,

$$F(q_x,q_y) = \int_{-\infty}^{\infty}\int_{-\infty}^{\infty} f(x,y)e^{i[(q_x+\delta q_x)x+(q_y+\delta q_y)y]}dx\,dy\,, \tag{4.4}$$

is equivalent to adding a sloping contribution to the phase of $f(x,y)$:

$$F(q_x,q_y) = \int_{-\infty}^{\infty}\int_{-\infty}^{\infty} f(x,y)e^{i[(\delta q_x)x+(\delta q_y)y]}e^{i(q_x x+q_y y)}dx\,dy\,. \tag{4.5}$$

As a result, centering the speckle pattern by placing its centroid at the origin of reciprocal space tends to remove the first moment of the reconstructed phase function. Measurements done by STM, AFM, or profilometry typically also have the slope removed by software.

The presence of the dual solution suggests a whole class of alternate solutions, as described by Barakat and Newsam in Ref. [66]. Let $f(x,y)$ and $F(q_x,q_y)$ be a solution pair to the phase problem. Note that the Fourier transform of the dual is

given by

$$\mathcal{F}\left[f^*(-x,-y)\right] = F^*(q_x, q_y)\,, \tag{4.6}$$

and that if $F(\tilde{q_x}, \tilde{q_y})$ is an analytic function of the complex variables $\tilde{q_x}$ and $\tilde{q_y}$, then so is the function $F^*(\tilde{q_x}^*, \tilde{q_y}^*)$, and both have the same modulus for real values of $\tilde{q_x}$ and $\tilde{q_y}$. If the reciprocal-space function F can be factored such that $F(q_x, q_y) = F_1(q_x, q_y)F_2(q_x, q_y)$, then the function $H(q_x, q_y) = F_1(q_x, q_y)F_2^*(q_x, q_y)$ and its inverse Fourier transform $h(x, y) = \mathcal{F}^{-1}[H(q_x, q_y)]$ also form a solution pair to the phase problem, since $|H(q_x, q_y)|^2 = I(q_x, q_y)$. The correct reconstructed image f will not in general resemble closely the alternate image h. Barakat and Newsam also claim to show that *all* alternate solutions to the phase problems can be mapped one-to-one with the factorizations of F. They further state that, while the existence of multiple solutions is actually a problem for one-dimensional phase retrieval, multiplicity of solutions in two or more dimensions is "pathologically rare." The difference between the one-dimensional case and that of two or more dimensions is topological; zeroes in a complex function of one real variable separate the real domain of the function into disjoint regions on which the function can be either "flipped" to its conjugate or left unchanged. In two or more dimensions, the zeroes of F must form closed loops or closed surfaces, within which F is flipped, and this is said to be unlikely [66]. Other articles also address the difference between the cases of one-dimensional phase retrieval and multi-dimensional phase retrieval [67–69], and in particular the case of radial symmetry in two dimensions, which reduces the problem to one dimension [70].

Even if speckle patterns $I(q_x, q_y)$ with multiple real-space solutions are pathologically rare, the problem would still be intractable if a small amount of noise in the measurement of I made it indistinguishable from another speckle pattern which does have multiple solutions. Monte Carlo simulations have been performed to establish the level of noise at which ambiguity in the phase retrieval problem ensues [71]. That work focussed on images of only 2×2 and 3×2 pixels, and it is uncertain how the

results would apply to images of practical resolution.

In the usual case of discretely sampled data, the question of uniqueness of solutions can be examined by counting the number of unknowns and the number of equations in the problem. The discrete Fourier transform on the M by N array relating $F(q_x, q_y)$ and $f(x, y)$ is

$$F(q_x, q_y) = \sum_{x,y} f(x, y) \exp\left[\frac{2\pi i}{N}\left(q_x x + q_y y\right)\right], \tag{4.7}$$

where the sum runs over the discretized coordinates x and y in the array, and q_x and q_y are coordinates in the discrete reciprocal-space array. The physical sizes of discrete steps in x and y are related to the physical sizes of steps in q_x and q_y by

$$\Delta x\, \Delta q_x = \frac{2\pi}{M}, \text{ and } \Delta y\, \Delta q_y = \frac{2\pi}{N}. \tag{4.8}$$

Since we actually have only $|F(q_x, q_y)|$ from the experiment, the system of equations necessary to solve for phase retreival is

$$|F(q_x, q_y)| = \left|\sum_{x,y} f(x, y) \exp\left[\frac{2\pi i}{N}\left(q_x x + q_y y\right)\right]\right|. \tag{4.9}$$

In general, this yields MN equations, one for each point (q_x, q_y) in the reciprocal-space array. There are, however, $2MN$ unknowns, the real and imaginary parts of each of the MN values of $f(x, y)$ on the grid. If, however, the reciprocal-space measurements oversample the continuous speckle intensity by a factor of two or more, then the number of equations in Equation 4.9 becomes $\geq 2MN$, but the number of unknowns remains $2MN$, so the problem is possibly overdetermined. Oversampling in reciprocal space is equivalent to padding the real-space array with a known set of zero values. Thus, the region over which f is nonzero, called the support of f, can be made to contain less than half of the whole array. Miao *et al.* introduce the ratio σ, defined as [72]

$$\sigma = \frac{\text{number of total pixels}}{\text{number of unknown pixels}}, \tag{4.10}$$

which characterizes the degree of oversampling in reciprocal space. The proceeding argument suggests that the problem becomes overdetermined, in any number of dimensions, when $\sigma > 2$. The argument neglects, however, the possibility of redundancy in the equations, which could in principle still leave the problem underdetermined even with $\sigma > 2$. Also, these equations are nonlinear, and thus the relationship of the number of equations with the number of variable does not necessarily have the same implications as in the case of a system of linear equations. A computer experiment which bears out the $\sigma > 2$ threshold in the case of simulated Cu_3Au CXD in two dimensions is presented in Section 4.6.

The autocorrelation of f is given by the Fourier transform of $|F|^2$, which is the experimentally measured intensity. The support of the autocorrelation of f is twice the support of f itself in any direction; thus, a useful upper bound on the size of the the support of f can be computed directly from an intensity measurement. Methods for determining the support of an object from the support of its autocorrelation, in the cases of objects with convex supports and of objects consisting of collections of distinct points, were described by Fienup *et al.* in Ref. [73].

4.3 Gerchberg-Saxton Algorithm

The Gerchberg-Saxton algorithm was developed to solve the problem of reconstructing the phase from two intensity measurements, one in real space and one in reciprocal (or Fourier) space [74–76]. The algorithm for finding a solution pair $f(x, y)$ and $F(q_x, q_y)$ from a given real-space modulus $B(x, y)$ and reciprocal-space intensity $I(q_x, q_y) = |F(q_x, q_y)|^2$ is made up of four steps: (1) Fourier transform an estimate of the real-space function $f(x, y)$; (2) replace the modulus of the resulting estimate of $F(q_x, q_y)$ with the observed modulus $\sqrt{I(q_x, q_y)}$; (3) compute the inverse Fourier transform; and (4) replace the modulus of the computed function with that of the given real-space

modulus $B(x,y)$. The kth iteration of the algorithm takes the form

$$\begin{aligned} F_k(q_x,q_y) &= \mathcal{F}(f_k(x,y)) && (4.11)\\ F'_k(q_x,q_y) &= \sqrt{I(q_x,q_y)}\exp\{i\arg[F_k(q_x,q_y)]\} && (4.12)\\ f'_k(x,y) &= \mathcal{F}^{-1}(F'_k(q_x,q_y)) && (4.13)\\ f_{k+1}(x,y) &= B(x,y)\exp\{i\arg[f'_k(x,y)]\}\ . && (4.14) \end{aligned}$$

To show that this algorithm converges, let us define the reciprocal-space error metric

$$R_{Fk} \equiv \frac{\sum\limits_{q_x,q_y}\left[|F_k(q_x,q_y)| - \sqrt{I(q_x,q_y)}\right]^2}{\sum\limits_{q_x,q_y} I(q_x,q_y)}\,. \tag{4.15}$$

Since $F'_k(q_x,q_y)$ satisfies the reciprocal-space constraint, as indicated by Equation 4.12, it has the modulus of $I(q_x,q_y)$. The phases of $F_k(q_x,q_y)$ and $F'_k(q_x,q_y)$ are the same; thus, the error metric can also be expressed by

$$R_{Fk} = \frac{\sum\limits_{q_x,q_y}|F_k(q_x,q_y) - F'_k(q_x,q_y)|^2}{\sum\limits_{q_x,q_y} I(q_x,q_y)}\,. \tag{4.16}$$

After noting that $\mathcal{F}(F_k - F'_k) = f_k - f'_k$, Parseval's theorem implies

$$R_{Fk} = \frac{\sum\limits_{x,y}|f_k(x,y) - f'_k(x,y)|^2}{\sum\limits_{q_x,q_y} I(q_x,q_y)}\,. \tag{4.17}$$

Now, let the real-space error metric after the kth iteration be defined in the following manner:

$$R_{fk} \equiv \frac{\sum\limits_{x,y}|f_{k+1}(x,y) - f'_k(x,y)|^2}{\sum\limits_{x,y}[B(q_x,q_y)]^2}\,. \tag{4.18}$$

Another application of Parseval's theorem shows that

$$\sum_{x,y}[B(q_x,q_y)]^2 = \sum_{q_x,q_y} I(q_x,q_y)\,. \tag{4.19}$$

The last step of the kth iteration, as shown in Equation 4.14, and of the previous iteration guarantee that both $f_k(x,y)$ and $f_{k+1}(x,y)$ satisfy the real-space constraint that their magnitudes are equal to $B(x,y)$. The phases of $f_{k+1}(x,y)$ and $f'_k(x,y)$ are the same, and the amplitudes of $f_k(x,y)$ and $f_{k+1}(x,y)$ are equal. Thus,

$$|f_{k+1}(x,y) - f'_k(x,y)| \leq |f_k(x,y) - f'_k(x,y)| \,, \tag{4.20}$$

from which we obtain

$$R_{fk} \leq R_{Fk} \,. \tag{4.21}$$

A completely analogous argument can be used to show that

$$R_{F,k+1} \leq R_{fk} \,. \tag{4.22}$$

Therefore, we see that

$$R_{F,k+1} \leq R_{fk} \leq R_{Fk} \,, \tag{4.23}$$

and the Gerchberg-Saxton algorithm either reduces the error metric or leaves it unchanged after each iteration. A serious problem with the Gerchberg-Saxton algorithm, however, is that the error metric very often reaches plateaus over which many iterations fail to reduce the error substantially.

4.4 Hybrid Input-Output Algorithm

A method which has been found to succeed in alleviating the phase retrieval stagnation problem is the "input-output" algorithm invented by Fienup [77]. I have implemented an adaptation of the hybrid input-output (HIO) algorithm, as described by Millane and Stroud [78; 79]. This algorithm differs from the Gerchberg-Saxton algorithm in two important ways. First, it tolerates some error in the fit, so that the constraint is not imposed on areas of the reconstructed image which differ from

the constrained version of the image estimate by a small value ϵ. Second, instead of completely enforcing the real-space constraint, the HIO algorithm gradually drives the image estimates toward one which satisfies the constraint. The constraint may be chosen in a rather general way, so that it is a modification of the image estimate having the properties known to be true of the correct image; examples of constraints which have been applied are positivity [72] and noncrystalline symmetry [78]. Both articles also report enforcement of a real-space support constraint.

We have implemented the HIO algorithm following the manner reported by Millane [78]. It differs from the Gerchberg-Saxton algorithm by replacing the step of Equation 4.14 with the following:

$$f_{k+1}(x,y) = \begin{cases} f'_k(x,y) & \text{if} \quad |f'_k(x,y) - c_k(x,y)| < \epsilon \\ f_k(x,y) + \beta\left[c_k(x,y) - f'_k(x,y)\right] & \text{if} \quad |f'_k(x,y) - c_k(x,y)| \geq \epsilon \end{cases} . \tag{4.24}$$

Here, $c_k(x,y)$ represents a modification of $f'_k(x,y)$ which satisfies the real-space constraints, which will be described below. The quantity $c_k(x,y) - f'_k(x,y)$ is the amount by which the image estimate $f'_k(x,y)$ differs from the constraint, so the parameter β governs how quickly the system is driven toward the constraint. The value used for β requires some tuning; it was typically set to a value between 0.3 and 0.7. The other parameter, ϵ, permits a small deviation from the constraint to be tolerated. While using a nonzero value for ϵ may have beneficial effects regarding computational speed, I did not observe any benefit to the convergence of the algorithm that could be attributed to having a nonzero ϵ.

In utilizing the HIO algorithm for the special case of CXD from Cu_3Au, I have introduced a new type of real-space constraint which greatly improves the performance of the algorithm by introducing more *a priori* information about the form of the reconstructed image. The amplitude and phase of the wavefront incident on the sample is taken to be known from the geometry of the experimental setup and Fres-

nel diffraction. The phase modulation due to a superstructure reflection from Cu_3Au antiphase domains is known to give rise to a phase in Equation 4.2 of

$$\phi(x,y) = \begin{cases} 0 & \text{if } (x,y) \text{ lies in domain I or II} \\ \pi & \text{if } (x,y) \text{ lies in domain III or IV} \end{cases} , \tag{4.25}$$

where the definition of which of the four antiphase domain types are I and II or III and IV depends on whether the reflection is the (100), the (101), or another superstructure reflection. The real-space structure of the Cu_3Au antiphase domains is contained in the function $\phi(x,y)$. We wish to reconstruct $\phi(x,y)$ by inverting the diffraction data.

The constrained version $c_k(x,y)$ of the kth-iteration image estimate $f'_k(x,y)$ is constructed in the following manner:

$$c_k(x,y) = \begin{cases} |f'_k(x,y)| \cos\left[\eta(x,y)\right] e^{i\phi_F(x,y)} & \text{if } |f'_k(x,y) \cos\left[\eta(x,y)\right]| \leq B(x,y) \\ B(x,y) \text{sgn} \cos\left[\eta(x,y)\right] e^{i\phi_F(x,y)} & \text{otherwise} , \end{cases} \tag{4.26}$$

where

$$\eta(x,y) \equiv \{\phi_F(x,y) - \arg\left[f'_k(x,y)\right]\} \tag{4.27}$$

is the difference in phase between the image estimate and the Fresnel phase at the point (x,y). If there were no distortion of the phase due to the Fresnel diffraction of the slits, this constraint would be a compression of complex values onto a line segment on the real axis from $-B(x,y)$ to $B(x,y)$. This mapping of $f'_k(x,y)$ to $c_k(x,y)$ is illustrated in Figure 4.1.

In contrast to the Gerchberg-Saxton algorithm, each iteration of the HIO algorithm does not necessarily reduce the error metrics. In fact, the first several iterations of the HIO algorithm typically "inflate" the error metric significantly; however, the HIO algorithm often does find solutions to the phase retrieval problem when the Gerchberg-Saxton algorithm fails. Experience shows that the optimal approach is to combine the two algorithms with several iterations of one followed by several iterations of the other, possibly repeating the sequence a number of times.

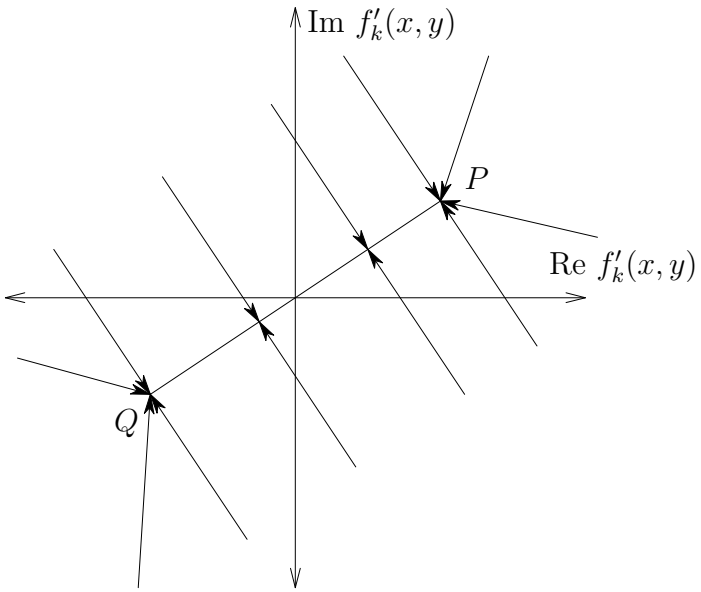

Figure 4.1: HIO constraint for Cu_3Au which maps $f'_k(x,y)$ to $c_k(x,y)$. Values of $f'_k(x,y)$ are mapped to the nearest point on the line segment PQ as shown, where P is the point $B(x,y)e^{i\phi_F(x,y)}$ and Q is the point $B(x,y)e^{i[\phi_F(x,y)+\pi]}$.

4.5 Simulations of Cu_3Au CXD

To provide controlled testing data for the Gerchberg-Saxton and HIO algorithms, I created simulated Cu_3Au antiphase domain structures and computed the speckle patterns which would result from illuminating them with a coherent beam. Since the "truth image," as it is called in the optics literature, is known for these simulations, the fidelity of their reconstruction under various conditions can be examined.

The illuminating beam with amplitude $B(x,y)$ and phase $\phi_0(x,y)$ was constructed by calculating the Fresnel diffraction pattern from a rectangular aperture according to the following equations [11]:

$$a_F^{(x)}(x,y) = B(x,y)e^{i\phi_0(x,y)} = a_F^{(x)}(x)a_F^{(y)}(y)\,, \tag{4.28}$$

and

$$a_F^{(x)}(x) = \frac{1}{\sqrt{2}}\left\{[C(x_2) - C(x_1)] + i\,[S(x_2) - S(x_1)]\right\}\,, \tag{4.29}$$

where $C(z)$ and $S(z)$ are the Fresnel integrals

$$C(z) = \int_0^z \cos\left(\frac{\pi z'^2}{2}\right) dz' \text{, and } S(z) = \int_0^z \sin\left(\frac{\pi z'^2}{2}\right) dz' \text{,} \tag{4.30}$$

with

$$x_1 = \sqrt{\frac{2}{\lambda L_x}}\left(x - \frac{d_x}{2}\right) \text{, and } x_2 = \sqrt{\frac{2}{\lambda L_x}}\left(x + \frac{d_x}{2}\right) \text{.} \tag{4.31}$$

Analogous relations define $a_F(y)$, y_1, and y_2. The parameters d_x and d_y represent the horizontal and vertical slit sizes, while L_x and L_y are the distances from the horizontal slit and from the vertical slit to the sample. The program used to generate Fresnel diffraction patterns uses the slit sizes d_x and d_y as parameters, along with $d_x\sqrt{2/(\lambda L_x)}$ and $d_y\sqrt{2/(\lambda L_y)}$, which describe the shape of the function in a scale-invariant way. In the limit of small $d_x\sqrt{2/\lambda L_x}$, the Fresnel diffraction begins to resemble far-field Fraunhofer diffraction, but the coordinates have units of length rather than of inverse length. The Fourier transform of the Fresnel-diffraction illumination function is, to a very good approximation, the sinc-function Fraunhofer diffraction pattern of the rectangular slit, which is just what would be seen if the the beam were to propagate all the way to the detector with no sample interaction. The coordinate system for $B(x,y)e^{i\phi_0(x,y)}$ was typically rotated by 30° with respect to the grid, so that effects arising from the grid frequency could be isolated from those arising from the direction of the Fresnel illumination. See Figure 4.2 for an example of this type of Fresnel diffraction pattern.

To simulate antiphase domains of Cu_3Au, I wrote a simple Metropolis algorithm simulation of single-pixel cells on a square lattice. The simulation was not intended to model closely the dynamics of nucleation and coarsening of antiphase domains–it was only meant to produce structures with similar characteristics to those of real Cu_3Au. The cells were initially set to one of N possible states. For simulating antiphase domains, I typically allowed $N = 2$ states for the system, to represent the two pairs of domains which are in contrast for a superstructure Bragg reflection.

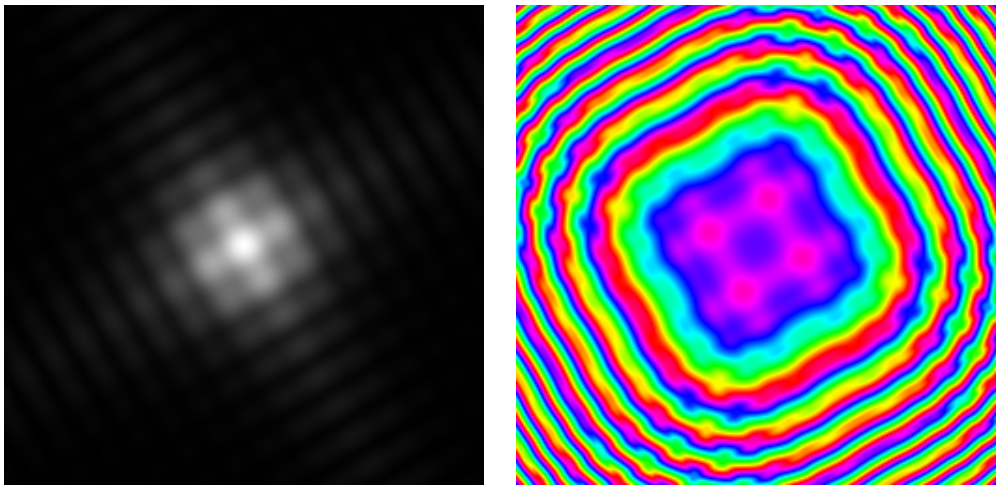

Figure 4.2: Computed Fresnel illumination for speckle simulation of Figure 4.3. On the left, the amplitude $B(x, y)$ is shown; the right panel shows $\phi_F(x, y)$. The arrays are 256×256 pixels. Phases are plotted here an in later figures using a cyclic red-blue-green-red color circle to represent 0 to 2π radians.

Allowing $N = 4$ states, two imparting a 0 phase shift to the illuminating wavefront, and two imparting a π phase shift, gave results very similar to the case of $N = 2$. The similarity of the contrasting domain structures of an $N = 4$ simulation with two distinct phases and of an $N = 2$ simulation with two distinct phases can be seen by comparing Figure 4.4 with Figure 4.5. The former was created having a higher interaction energy for the states, leading to smoother boundaries between domains and fewer nucleations.

The Metropolis algorithm for generating the Cu_3Au antiphase domain simulations consisted of two parts for each iteration. In the first part, a site was chosen at random from the two-dimensional square array and a neighboring site, randomly above or to the right with equal probability, was selected. The boundary conditions were periodic, so the neighbor above a top-row site was on the bottom row, and the neighbor right of a right-column site was on the left column. Then, the energies of four configurations were computed: (1) leave the sites unchanged, (2) exchange the two sites, (3) set both sites to the state of the current site, and (4) set both sites to the state of the partner site. Refer to these energies as E_1, E_2, E_3, and E_4. They were calculated as the sum of

the state energy of the site and its partner and a nearest-neighbor interaction energy of the site with its partner and of each with its three other neighbors. (For the case of Cu_3Au antiphase domains with only the lower-energy Type I domain boundaries, all states should have the same energy and all interfaces should have the same energy.) Next, the partition function for the four configurations was calculated according to

$$Z = \sum_{i=1}^{4} e^{-\beta E_i} \,, \tag{4.32}$$

where $\beta = (k_B T)^{-1}$ has units of inverse energy and is inversely proportional to the "temperature" of the simulation. To decide which configuration to accept, a random number s on the interval $[0, 1]$ was chosen. If

$$s < Z^{-1} e^{-\beta E_1} \,, \tag{4.33}$$

then the first configuration was taken. If instead

$$e^{-\beta E_1} Z^{-1} \leq s < (e^{-\beta E_1} + e^{-\beta E_2}) Z^{-1} \,, \tag{4.34}$$

then the second configuration was chosen. If

$$(e^{-\beta E_1} + e^{-\beta E_2}) Z^{-1} \leq s < (e^{-\beta E_1} + e^{-\beta E_2} + e^{-\beta E_3}) Z^{-1} \,, \tag{4.35}$$

then the third configuration was accepted, and finally, the fourth configuration was taken if

$$(e^{-\beta E_1} + e^{-\beta E_2} + e^{-\beta E_3}) Z^{-1} \leq s < 1 \,, \tag{4.36}$$

The second part of each Metropolis algorithm iteration was designed to allow nucleation of domains. First, a site was selected from the array at random. A random number t in the interval $[0, 1]$ was chosen. Then the state and interaction energy for setting the state to each of the N possible states were computed, and a resulting state was chosen using a partition function analogous to the above, except with N terms.

As an illustration of the simulation, Figure 4.3 shows a series of simulated Cu_3Au antiphase domains on a 256×256 site array. The top left image shows the initial

configuration, with a random set of four domains with equal probability for each. The middle left image shows the system after 2.5×10^5 iterations of the Metropolis algorithm, and the bottom left image shows the system after 10^6 iterations. The red and yellow pixels indicate states which have a zero phase, while the blue and cyan pixels indicate states which have a phase of π. The state of the bottom left image is also shown in Figure 4.4, which has the sites colored according to phase rather than according to state. In this example, nucleations were very rare, since the interaction energy was large compared to β, which was 0.75 energy units, while the state energies were all zero energy units, and the interaction energies were 5 energy units. The right column shows the simulated speckle amplitude for each of the simulated domain structures, assuming illumination by a wavefront having the $B(x, y)$ and $\phi_0(x, y)$ shown in Figure 4.2. As expected from the Scherrer formula, the overall width of the speckle patterns is inversely proportional to the characteristic size of the real-space structures, while the size of each speckle corresponds to the (fixed) size of the illuminating beam.

After coloring the sites according to their phase, as shown in the left panel, the contrasting domain structure as would be measured at a superstructure Bragg reflection can be seen. This represents the "truth image" which the reconstruction algorithms seek to obtain from the speckle amplitude and the amplitude $B(x, y)$ and the phase $\phi_0(x, y)$ of the illumination.

For a comparison of the simulation with the structure of real Cu_3Au, I have applied a standard edge-detection routine to the left image of Figure 4.4 to obtain the pattern of boundaries shown in the right image. This pattern should correspond to the system of antiphase domain boundaries that can be measured directly using dark-field TEM with a superstructure reflection selected. Comparison with the image shown in Figure 1.8 suggests that the simulation does provide an accurate enough model of domain coarsening for use in testing the image reconstruction methods

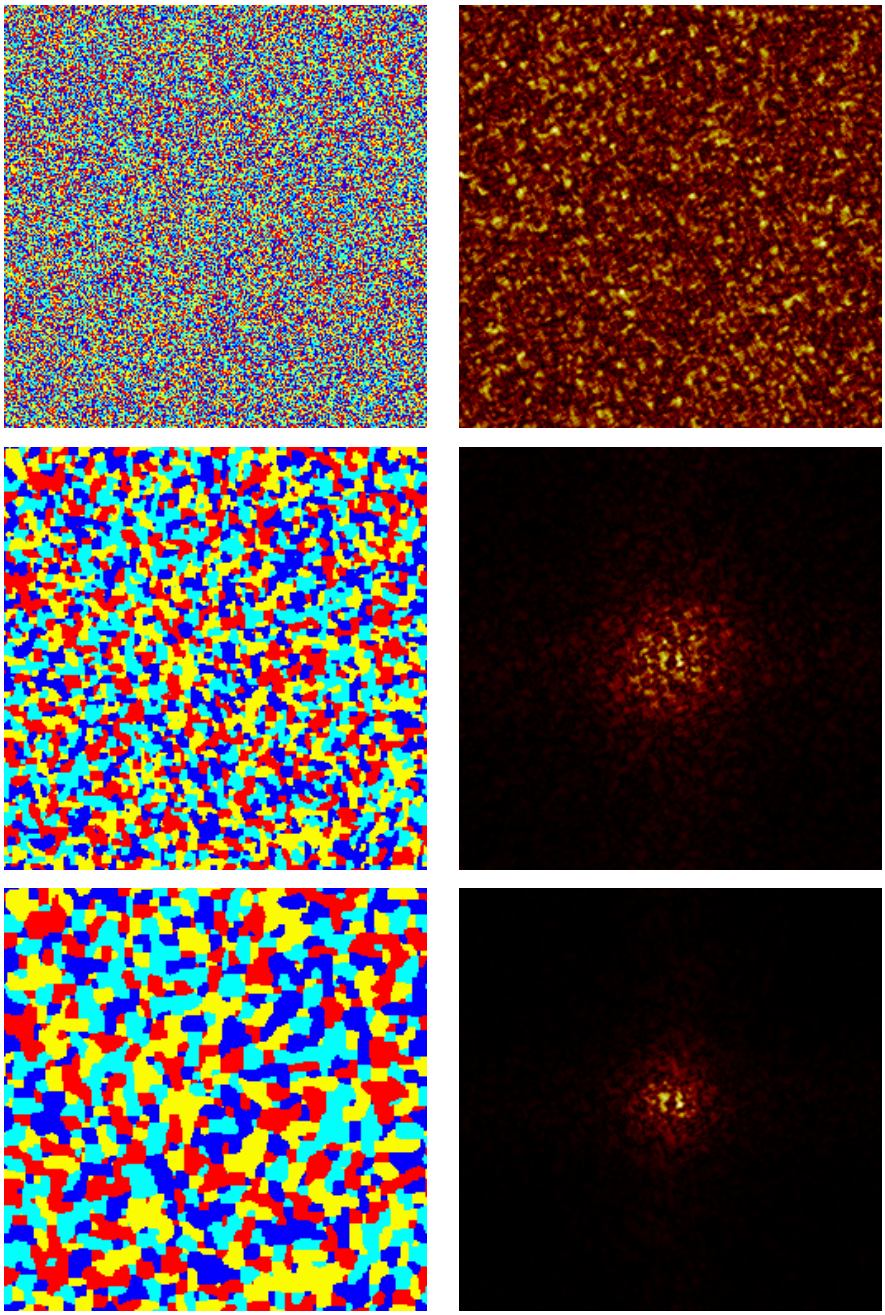

Figure 4.3: Simulated Cu_3Au antiphase domains with speckle patterns computed using the illumination of Figure 4.2. On the left column, the four domains are represented by red, blue, yellow, and cyan; the red and yellow have zero phase, while the blue and cyan have π phase. The right column shows the amplitude of the speckle patterns corresponding to the domain structures. The top, middle, and bottom rows show the simulation after 0, 2.5×10^5, and 10^6 Metropolis algorithm iterations, respectively. Each image shows the whole array of 256×256 sites.

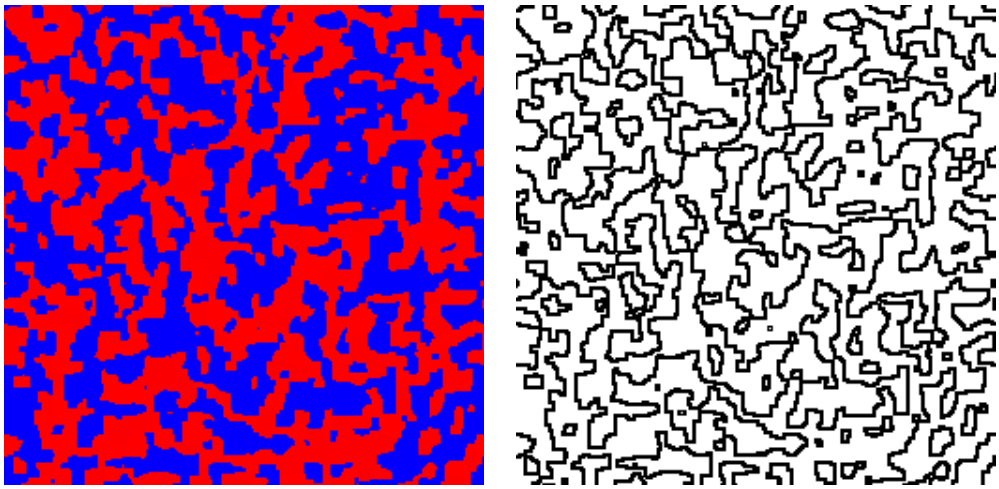

Figure 4.4: Contrasting antiphase domains and antiphase boundaries. Shown at left is the same antiphase domain structure as the bottom case of Figure 4.3, with the red and yellow domains (with zero phase) colored red here, and the blue and cyan domains (with π phase) colored blue. This is the contrasting antiphse domain structure to which the speckle simulation is sensitive. At right are shown the edges between the red and blue areas of the left image; compare this simulation with the antiphase boundaries depicted in Figure 1.8.

described in this chapter.

4.6 Oversampling in Reciprocal Space

One method which has been reported to improve the convergence of the Gerchberg-Saxton and HIO algorithms is to increase the sampling density in reciprocal space beyond the Bragg frequency [72]. However, subtle changes in the set of constraints which derive from any *a priori* information about the solution f can change the uniqueness and convergence properties of the reconstruction markedly. In order to test the effectivness of oversampling in reciprocal space in the special case of Cu_3Au CXD with a known illumination wavefront, I constructed a simulated antiphase domain structure with an array size of 128×128 pixels. Figure 4.5 shows the input wavefront amplitude and phase, the simulated antiphase domain structure, and the phase of the resulting real-space wavefront, which is the sum of the Fresnel phase with the phase modulation of the antiphase domains. In addition to the original array, I also

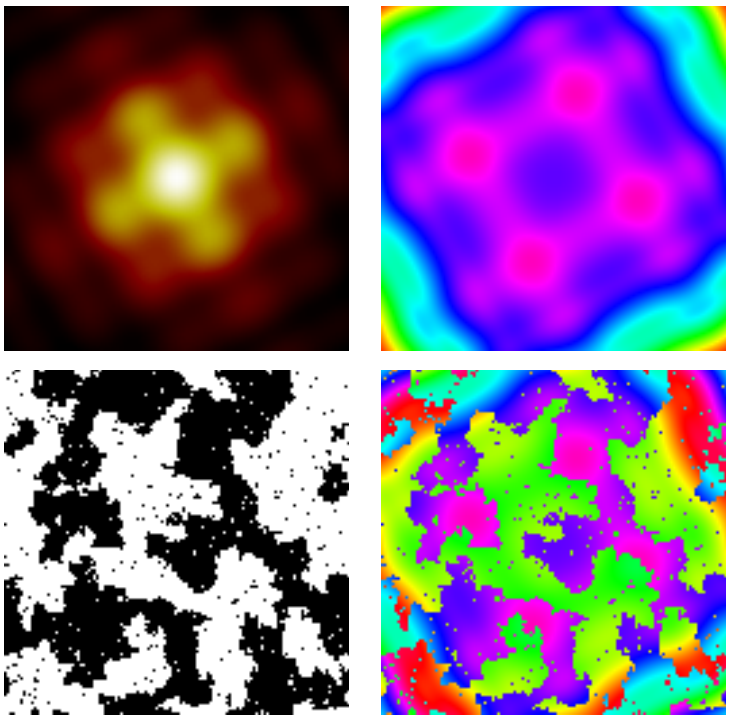

Figure 4.5: Input Fresnel illumination and simulated antiphase domains for the oversampling series. The amplitude $B(x, y)$ is shown at upper left, the Fresnel diffraction phase $\phi_0(x, y)$ at upper right, the simulated antiphase domains at lower left, and the real-space (object) phase at lower right. The array size is 128 $\times$ 128 in each image.

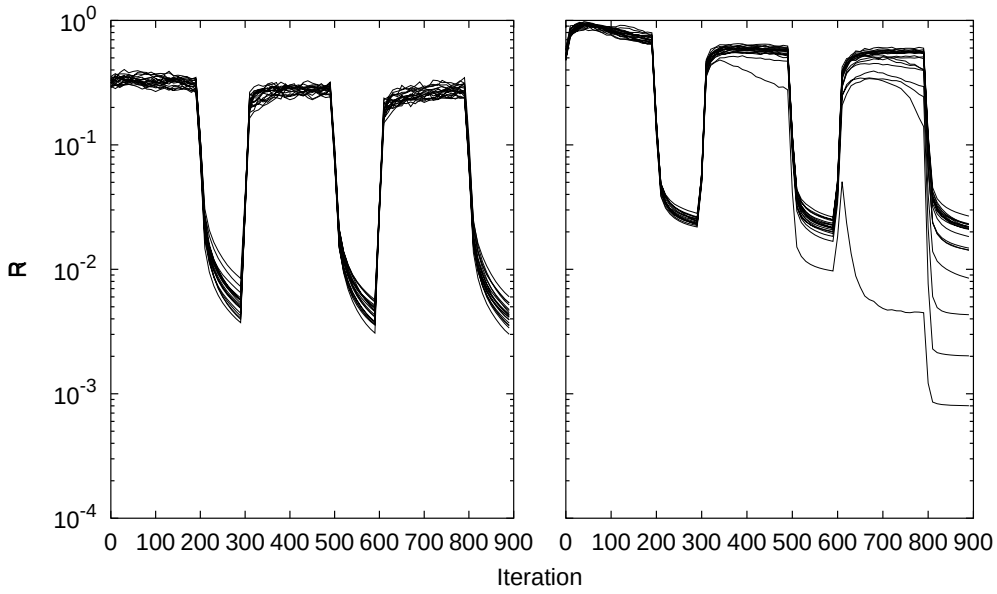

Figure 4.6: Error metric R_f vs. iteration number k for the 160 × 160 image and the 256 × 256 image. The fits for which the algorithms converge to the truth image can be easily distinguished by the rapid drop in R_f. Also, the "inflation" of the error metric at the beginning of each group of HIO iterations is evident. A representative set of fits are plotted for each of the two images.

padded with zeroes to 256 × 128, 128 × 256, 160 × 160, 192 × 192, 256 × 256, and 256 × 320. These correspond to $\sigma = 1$ for the original array, and $\sigma = 2$, $\sigma = 2$, $\sigma = 1.5625$, $\sigma = 2.25$, $\sigma = 4$, and $\sigma = 5$ for the respective arrays, and the computed speckle patterns indeed were oversampled, such that the same features were present in the larger arrays but described by more points.

For each oversampling ratio, I conducted 50 fits, with each fit starting with a different set of randomized starting phases. The fits had three cycles, each cycle consisting of 200 HIO iterations followed by 100 Gerchberg-Saxton iterations. Each ensemble of 50 fits requires about 2 hours of running time on a 400 MHz Pentium II, but the running time, of course, depends on the array size. The real-space error metric R_f, was computed after each iteration. The behavior of R_f with iteration number for two representative cases, 160 × 160 oversampling (left) and 256 × 256 oversampling (right), are shown in Figure 4.6. The significant drop of R_f, which is seen for some fits on the right but not in the fits on the left, is a characteristic of

those fits in which the image estimate has good fidelity with the truth image. Also, it was often observed that, when two fits ended with very nearly the same R_f, their image estimate were the same; thus, even though each had begun with a different set of random starting phases, they both converged to the same solution. Note that not all of the 50 fits for the 256×256 array have actually converged to the truth image. Perhaps some of those would have converged after many more iterations, but it has been found that a balance between the number of independent fits and the number of iterations in each should be found for finding the best solution in the minimum computation time. Also, running multiple independent fits of the same data allows a check of the reproducibility with which the solutions are being found. If there are a group of widely varying solutions, each with a terminating value of R_f either very near to one another, then the fit cannot be said to have reconstructed the image uniquely. Also, if several differing solutions exist for which R_f (and hence R_F) is so low that none of them can be excluded due to measurement noise, then no unique solution can be said to have been found. For these reasons, it seems advisable to run multiple independent fits in the case of a real measurement for which the truth image is not known.

One way to visualize the spectrum of terminating values of R_f for an ensemble of fits is to sort the fits by final R_f, as shown in Figure 4.7. The 50 fits from which the plots in the figure were generated are assumed to be representative of the infinite set of fits which would result from all of the possible sets of random starting phases. As such, the *shape* of the curves shown should be representative of the same curves if many more fits had been computed. Very flat regions having the same terminating R_f indicate a group of fits which have converged to the same image estimate; such a flat region at the extreme low-R_f end indicate that the image estimate with the best fidelity with the measurement is also reproducible, i. e. the fitting process is insensitive to the random set of initializing phases.

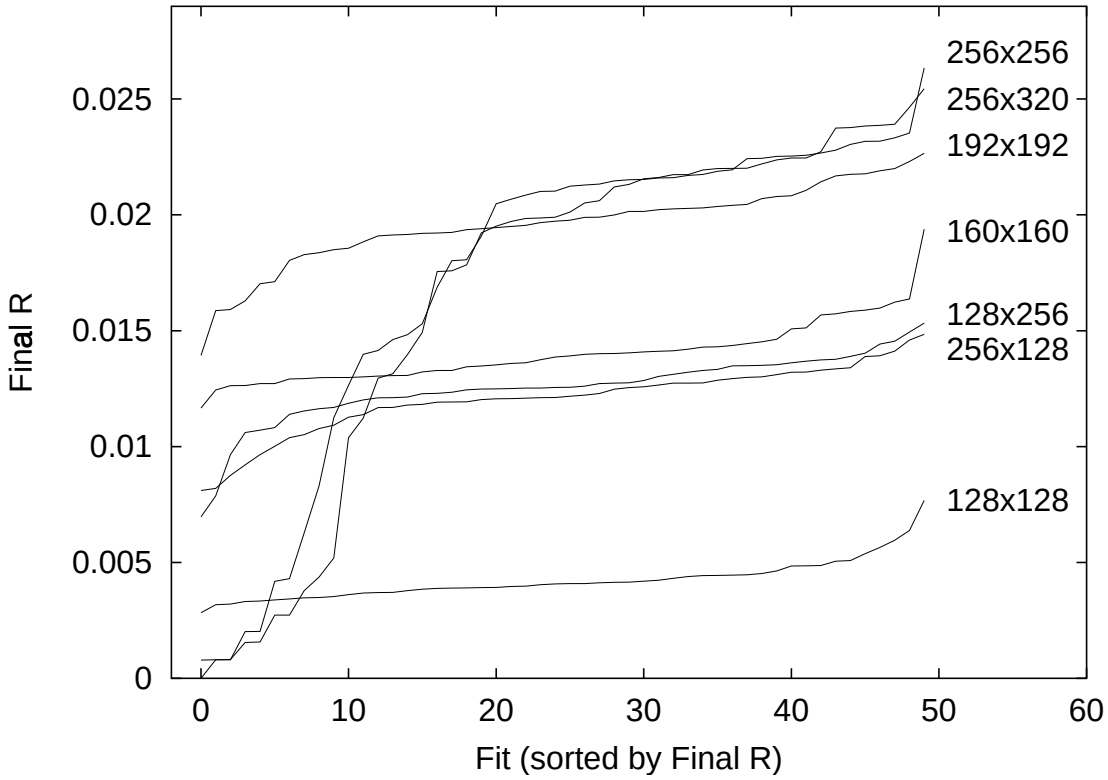

Figure 4.7: Sorted terminating values of R_f for 50 fits with seven different oversampling ratios. Since R_f does not scale in a clear way with the array size, it should not be used for comparison of the convergence of one array size with another.

In this example, it can be seen that the behavior changes as σ approaches two, and again as σ approaches four. For the two cases with $\sigma < 2$, the low-R_f end of the curves has very little rolloff from the gently sloping plateau. For $2 \leq \sigma < 4$, a significant rolloff is seen. When $\sigma \geq 4$, the shape of the observed curve changes again, so that a much greater fraction of the fits have a lower terminating R_f value than those on the plateau. The last point at the high-R_f end of the 160×160 curve is considered an outlier, which had a particularly difficult set of random phases at initialization.

The image estimates having the lowest terminating value of R_f for the seven levels of oversampling are shown in Figure 4.8. These seven images fall quite clearly into three groups. Those with $\sigma < 2$, panels (A) and (B), do not resemble the truth image to any degree. Note that the statistical properties of an image estimate, such as the size of the domains, can be obtained directly from the properties of its speckle pattern. Panels (C), (D), and (E) show the image estimate for which $2 \leq \sigma < 4$. These do reproduce the features of the truth image well, but not at the pixel-by-pixel level exhibited by the images estimates of (F) and (G), for which $\sigma \geq 4$.

It is possible to draw a some conclusions from this computer experiment, which will guide the application of these algorithms to real measurements of Cu_3Au. The Gerchberg-Saxton algorithm and the HIO algorithm (adapted for Cu_3Au CXD) begin to converge when the oversampling ratio σ exceeds two, but the best reconstructions tend to occur when the oversampling ratio is at least four. With $\sigma \geq 4$, very accurate reconstructions are possible, but it is still necessary to run multiple fits and accept the result with the lowest R_f. The results with 128×256 and 256×128 padding suggest that the effects of oversampling are dependent only on the *area* ratio σ and not on the degree of oversampling in each direction.

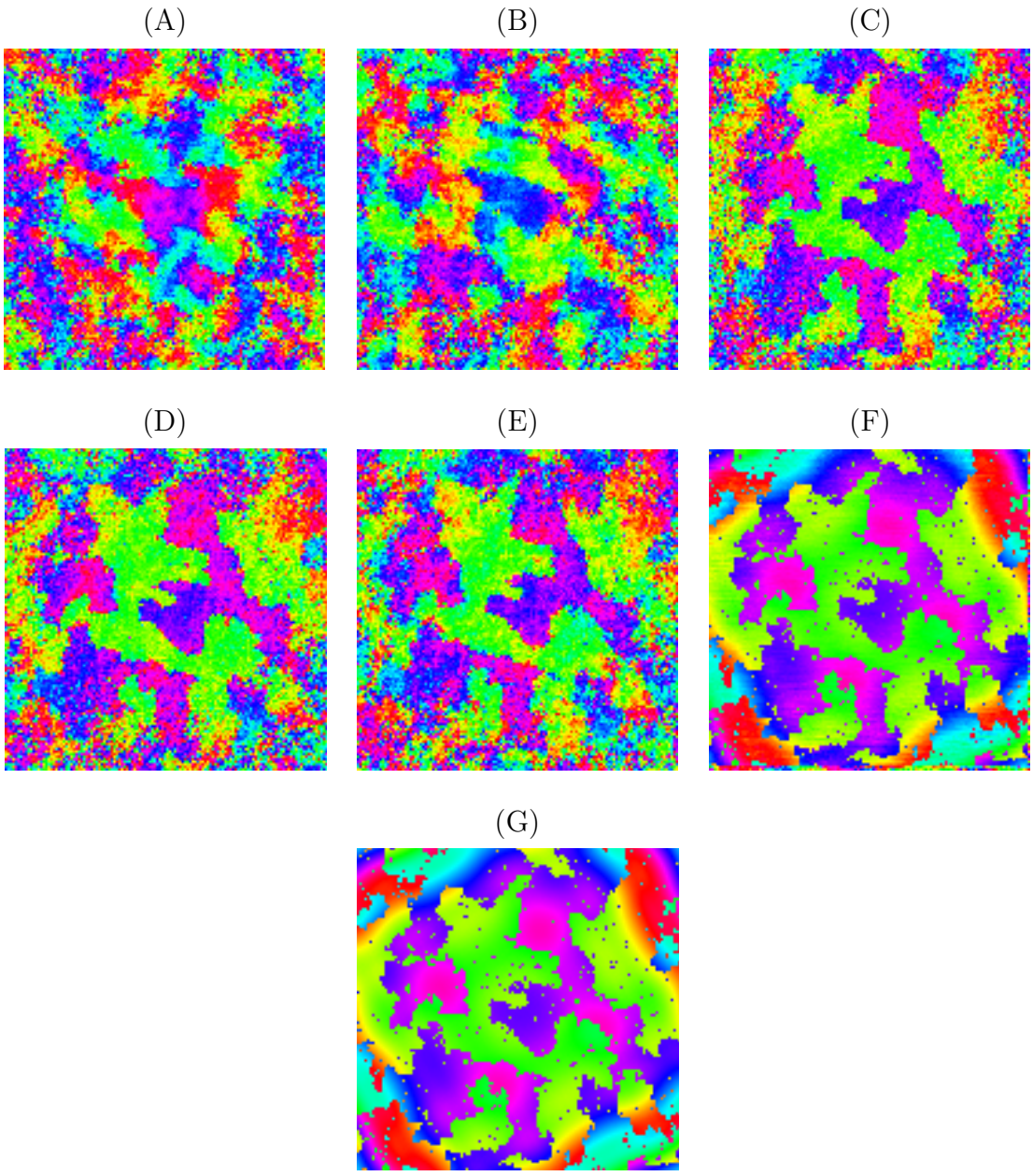

Figure 4.8: Resulting image estimates for seven levels of oversampling. Left to right, from top, the images show the phase of the lowest-R result of fits with (A) no oversampling, and (B) 160 × 160, (C) 128 × 256, (D) 256 × 128, (E) 192 × 192, (F) 256 × 256, and (G) 256 × 320 oversampling. Compare each image with the input phase in the lower left panel of Figure 4.5.

4.7 Truncation of the CXD Pattern

Often, in a real measurement, the CXD pattern will extend beyond the edge of the detector, leading to a truncated CXD pattern. Assuming that the CXD pattern is roughly centered on the detector, the part of the pattern which is lost by truncation contains the high spatial frequency information about the sample. While this can be overcome experimentally by moving the detector and splicing the CXD patterns together or by modifying the detection to sample a larger region of reciprocal space, it is also the case that the noise in the measurement becomes much more significant near the edges of the CXD pattern. As a result, the data may be truncated near the edges simply as a result of Poisson counting statistics.

I constructed a simulation to test the effect of truncation of the reciprocal-space data. A model Cu_3Au antiphase domain structure was computed, and the CXD pattern resulting from the domains and a simple, real-valued illumination was then calculated. The illumination in this case was generated using a product of pairs of Fermi functions in the x and y directions:

$$B(x,y) = \frac{1}{1+e^{\left(x-\frac{1}{2}d_x\right)/s_x}} \frac{1}{1+e^{\left(-x-\frac{1}{2}d_x\right)/s_x}} \frac{1}{1+e^{\left(y-\frac{1}{2}d_y\right)/s_y}} \frac{1}{1+e^{\left(-y-\frac{1}{2}d_y\right)/s_y}} . \quad (4.37)$$

The illumination with $d_x = 25.6$, $d_y = 51.2$, $s_x = 1$, and $s_y = 1$, on a 256×256 array, is shown in the left panel of Figure 4.9. The simulated domain structure is shown in the left-center panel of Figure 4.9. The Fourier transform of the array having the Fermi-function modulus and the phase given by the simulated antiphase domains yields the simulated CXD pattern shown in the top-left panel of Figure 4.10. Since the real-space wavefront is real-valued in this case, the CXD pattern is centrosymmetric.

This array was then modified to simulate truncation of the CXD pattern to its central 100×100 pixel region by setting all values outside the region to zero. Then, two cycles of 500 HIO iterations and 200 Gerchberg-Saxton iterations were run using the truncated CXD pattern and the true real-space illumination function $B(x,y)$.

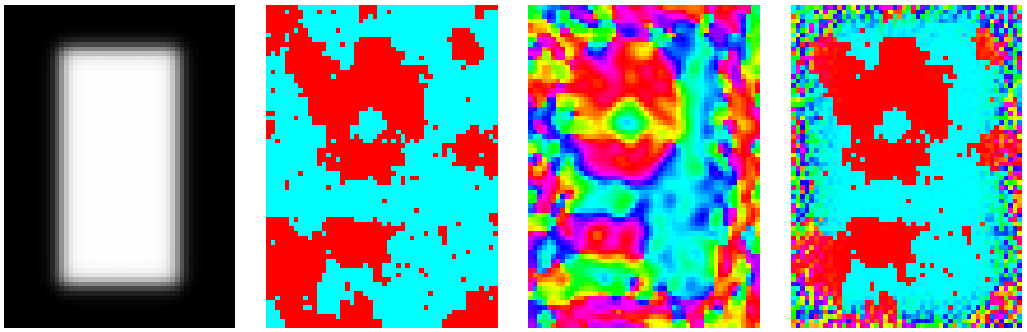

Figure 4.9: Real space input amplitude $B(x, y)$ (left), assumed phase (left center), phase reconstructed from truncated CXD pattern (right center), and phase reconstructed after restoration of the full CXD pattern (right). A 50 $\times$ 70 pixel region from the center of each 256 $\times$ 256 array is shown. Note that the CXD pattern contains no information regarding regions in real space where the illumination is zero.

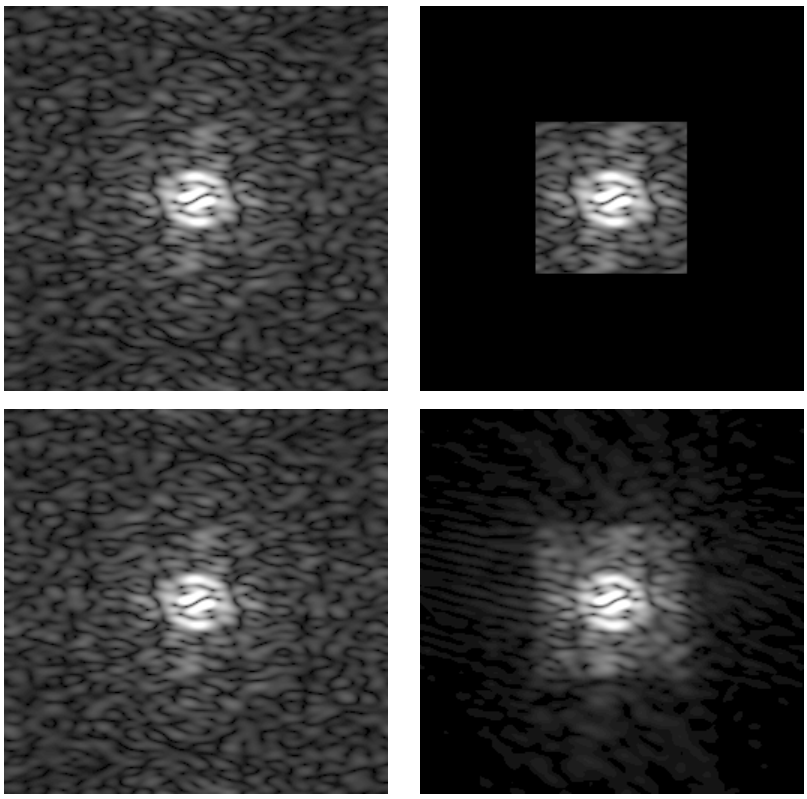

Figure 4.10: Reciprocal space arrays of the truncation test. The upper left panel shows the simulated CXD pattern computed directly from the real-space illumination and domain structure of Figure 4.9. The upper right panel shows the same array with the data truncated, so that each point outside the central 100 $\times$ 100 array is set to zero. The lower right panel shows the result of fitting the truncated data, and the lower left panel shows the result of continuing the same reconstruction with truncated part of the CXD pattern restored. The full 256 $\times$ 256 array is shown in each case.

Of 100 independent fits, the one with the lowest terminating R_F was selected, and its phase is shown in the right-center panel of Figure 4.9. The major features of the input image can be clearly seen in this reconstruction, even though it is based on only 15 percent of the information present in the full CXD pattern. The image shown here has been multiplied by a constant phase factor to align it with the original image; recall that such phase factors are not measurable in the experiment. Finally, the full CXD pattern was restored, and the fit was continued for 500 HIO iterations and 300 Gerchberg-Saxton iterations, with the result of the previous fit used as the initializing phases rather than the usual randomized phases. As can be seen, the final image reproduces very well the original image.

Even though a fit with good fidelity would likely have been obtained by proceeding directly with the reconstruction using the full CXD pattern, since for this case the ratio σ is approximately 18, this test does suggest that truncation of the CXD pattern does not necessarily prevent the reconstruction of an image with somewhat limited resolution. Since counting noise in an experiment tends to be most significant away from the center of the CXD pattern, this test demonstrates that at least some level of noise is tolerable for image reconstruction from CXD data. Furthermore, for some difficult image reconstruction problems, one may proceed with fitting the data by adding data for higher and higher resolutions in stages, as has been done in protein crystallograhy. This procedure is called "phase extension."

4.8 Phase Retrieval for Measured CXD Data

As an exploratory test, the phase retrieval procedure was applied to an experimentally obtained CXD pattern, the Cu_3Au (100) superstructure reflection obtained with $\alpha_i = 2^\circ$ ($\alpha_f = 11^\circ$) as shown in Figure 3.8. The values inside an 800 $\times$ 600 ellipse centered at the origin were selected, and after subracting from these values a constant

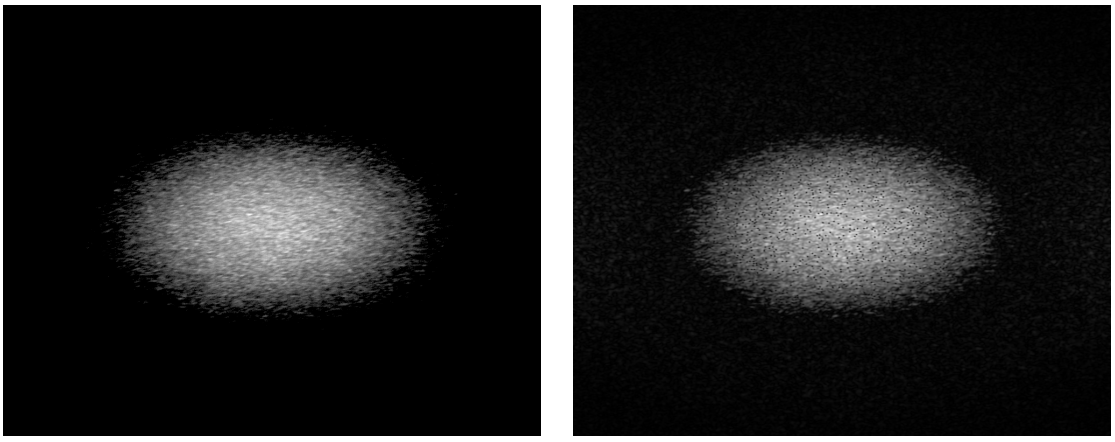

Figure 4.11: Measured amplitude data (left) and fit (right). The measured amplitude, obtained from the square root of the measurement shown in Figure 3.8, was truncated with a centered ellipse having a major axis of 400 pixels and a minor axis of 300 pixels. The result of a fit to this input is shown at right. The full 1000 × 800 arrays are shown in each case.

background such that the minimum point was zero, the selected values were placed in a 1000 × 800 array. The values in the array outside the ellipse were set to zero. The illumination was computed using the simple Fermi-function formula of Equation 4.37 instead of the more complicated Fresnel illumination, which would perhaps have been more accurate in describing the actual experiment. The size of the illumination was chosen based on the size of the observed speckles, and its edges were made very smooth. Smooth edges on the real-space illumination $B(x, y)$ had been observed to give rise to diffraction patterns with low contrast in the past.

A single independent fit was produced, having one cycle of 300 HIO iterations and 3000 Gerchberg-Saxton iterations. The fit was unsuccessful; it does not reproduce the features of the measured intensity well, as shown in Figure 4.11. It also did not yield the binary phase pattern expected for antiphase domains. An interesting set of defects or vortices scattered across the reconstructed CXD pattern can be seen, however. These consist of regions of about 2 × 2 pixels, and have nearly zero amplitude. The most intriguing feature of the vortices is that they resemble a sort of pole in the wavefront, such that the phase of the wavefront makes one complete

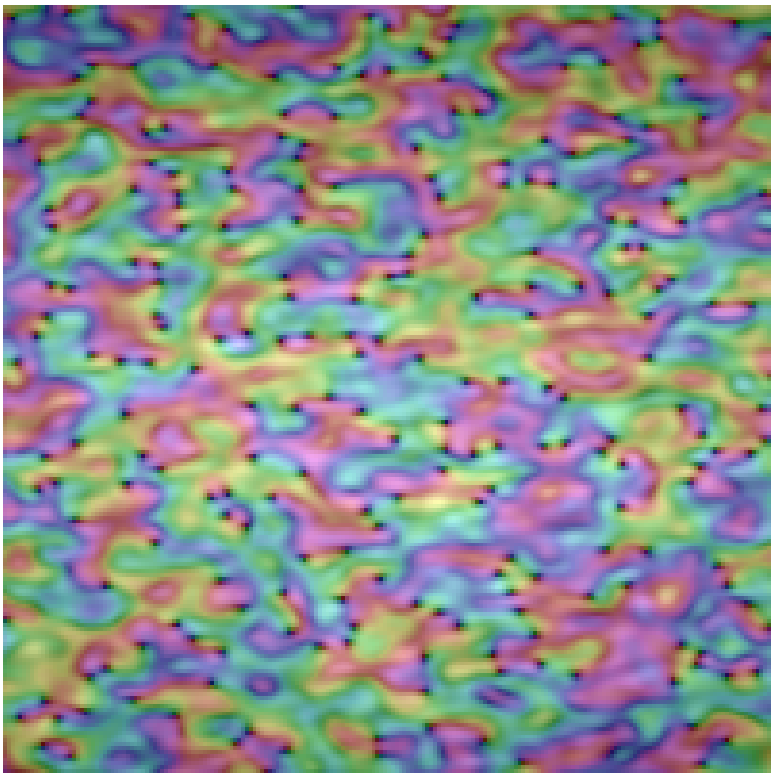

Figure 4.12: Detail of the reconstructed reciprocal-space wavefront. Shown here is a 200 × 200 pixel region from the center of the reciprocal-space fit shown in Figure 4.11. The phase is shown using the same cyclic color system as before, but is shaded with the modulus of the same array so that the small vortices can be located.

cycle of zero to 2π on a closed loop containing a single vortex. See Figure 4.12. The phases on small loops containing a single vortex always seem to make a single zero to 2π cycle; no vortices are observed around which a loop makes a 4π change. The vortices can have either sense, as can be seen in Figure 4.12 by noting that a blue-green red sequence is either clockwise or counterclockwise. Loops containing two vortices, as expected, can either make two complete cycles or zero. Once formed, the vortices did not spontaneously disappear on subsequent iterations of the phase retrieval algorithms.

The real-space array in the reconstruction has a similar behavior. The amplitude, which reproduces the smooth illumination function well aside from the local appearance of similar real-space vortices, is shown in Figure 4.13. A detailed view of the real-space array analogous to Figure 4.12 is shown in Figure 4.14. Here, the

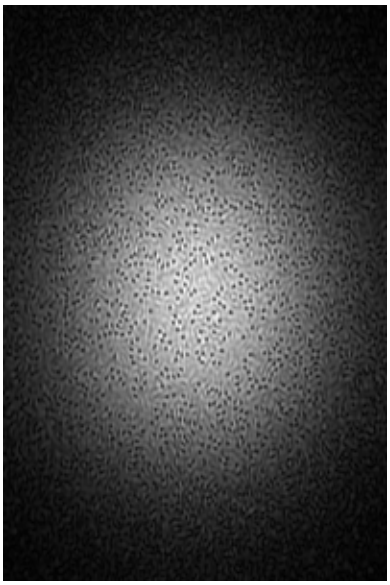

Figure 4.13: Fit to the real-space amplitude, with vortices clearly visible. A 200 × 300 pixel region from the center of the reconstructed amplitude is shown. Aside from the vortices and some noise, the shape of the assumed illumination is well-reproduced.

vortices have the same topological effect on the phase of the surrounding pixels. The reconstructed phases are not likely to represent the actual Cu_3Au antiphase domains in this case, since the fit to the data is poor, and the drop in R_F characteristic of successful convergence was not observed.

It has been suggested that real optical vortices might exist in an actual propagating wavefront [80]. What effect they may have on phase retrieval is unknown. If the vortices are not present in the physical wavefront, then some method must be found to anneal them out of the reconstruction, perhaps by forcing pairs with the opposite sense together so that they annihilate.

Several possible approaches for improving the performance of the phase retrieval algorithms for problems of this type exist. Increasing the oversampling ratio further would be likely lead to faster convergence. Some improved means of background subtraction, possibly in addition to correcting for the effects of partial coherence, should also improve the convergence. The illumination of the sample should be more precisely modelled using the Fresnel formulation, accounting for the parallax effect

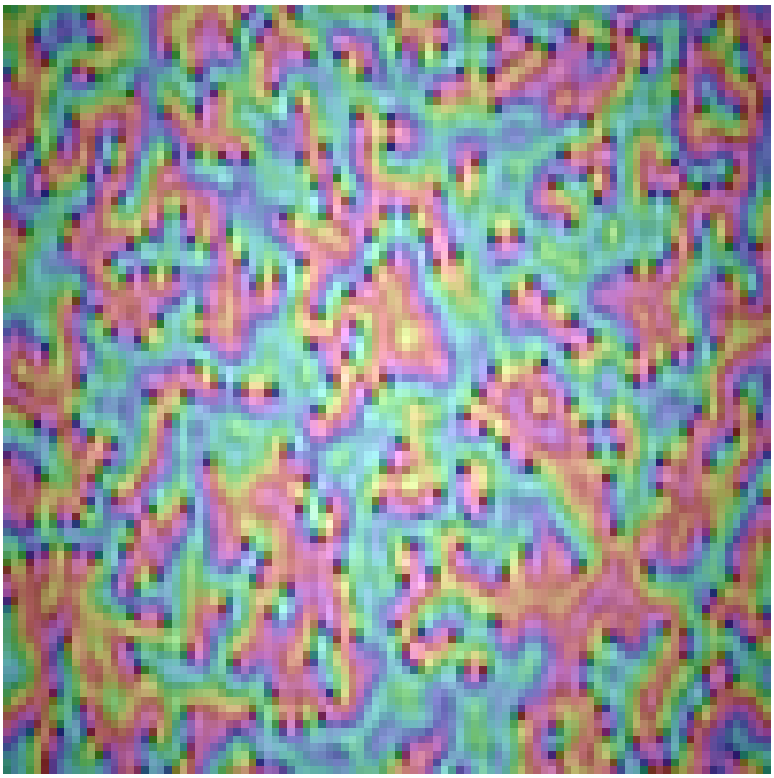

Figure 4.14: Detail of the reconstructed real-space phase structure, which should image the antiphase domains. Again, the cyclic color values for phase have been shaded by the corresponding amplitude values. A 100 × 100 pixel region from the center shows similar behavior of the phase near the vortices as was observed in the reciprocal-space fit.

of the roller-blade slits. Finally, better tuning of the mixing parameter β in the HIO algorithm may help avoid the onset of the vortices.

Chapter 5

Conclusions

The theoretical foundation for CXD is based on the familiar kinematical formulation for standard x-ray diffraction. In many ways, the diffraction physics of CXD can be more simply described than can the process of incoherent x-ray diffraction, since there is no ensemble averaging, and the detected signal is a simple complex amplitude sum over the scatterers within the illuminated volume. In CXD, there is no clear distinction, for example, between a Bragg reflection and the diffuse scattering surrounding it. The result, however, is that CXD measurements are sensitive to localized structures on a fairly wide range of length scales—from the size of the beam potentially down to the wavelength of the radiation. The limit of resolution will typically be set by the allowable dose for the sample or by the counting time possible in the experiment. In the case of a Cu_3Au superstructure reflection, half an hour of exposure yielded an effective real-space resolution of 50 nm, provided that an image could be reconstructed from the CXD pattern.

The experimental methods we utilized for conducting CXD measurements demonstrated that current x-ray sources, slit assemblies, and detection subsystems meet the requirements for CXD. The APS Undualor A, having a brilliance three orders of magnitude greater than previously available in the United States in the hard x-ray regime, delivers a usable coherent flux on a convenient length scale, matching well with many

specimens of experimental interest. The roller-blade slits gave us the capability to reproducibly set and position apertures with sub-micrometer resolution. Thus, we were able to measure the contrast ratio, and hence, the signal-to-noise ratio, of Cu_3Au CXD as a function of horizontal slit size, as shown in Figure 3.6. The length scale on which the contrast ratio fell with slit size was around 5 μm, as predicted from the van Cittert-Zernike theorem based on the stated source size and the distance from the source to the experiment. Since the far-field diffraction pattern of the roller-blade slits is well-understood, the illumination of the sample by them can be calculated in a straightforward way. This calculation can be crucial in making a reconstruction of the image of the sample.

The variation of the scattering geometry for two different Cu_3Au superstructure reflections was found to cause a marked elongation of the speckles along a well-defined direction as the grazing exit condition approached. Away from grazing exit, the major and minor axis length and the orientation of the speckles changed as well. The effect was quantified by computing the autocorrelation function for each series of images and then fitting each sharp central peak to an elliptical Gaussian. To explain the observation, a model was constructed, composed of a single cylindrical Gaussian of intensity oriented with its axis along the sample surface normal direction, which was evaluated on a plane to represent the sampling by the CCD in reciprocal space. The orientation of the plane was computed based only on the scattering geometry of the experiment. Since the reciprocal-space structures in question were of the same order in size as the bandwidth of the beam, we found it necessary to convolute the model images with a function representative of the wavenumber spread in the beam. The resulting model images reproduced the behavior of the observed speckles quite well, as shown in Figure 3.36, which supports the "bundle of rods" model for the reciprocal-space structure of Cu_3Au. By sweeping the energy of the incident beam, without moving the sample or the detector, it should be possible to sample

the entire superstructure reflection in three dimensions. After transforming such a measurement into the reciprocal-space coordinate system, one could reconstruct a full three-dimensional image of the illuminated volume of the sample using the Gerchberg-Saxton, HIO, and other algorithms.

Computer experiments were carried out to study the behavior of the Gerchberg-Saxton and HIO algorithms in a controlled way. To provide CXD data for these tests, I computed simulations of Cu_3Au antiphase domain coarsening using a simple Metropolis-algorithm program. The oversampling ratio, or equivalently the ratio of unknown pixels to the whole array size, was varied to determine what the oversampling ratio must be in order to reconstruct data for which a "truth image" is not known. It was found that the Gerchberg-Saxton/HIO algorithm combination begins to succeed when the oversampling ratio exceeds two, but that the fidelity of the reconstructed images improves markedly when the ratio exceeds four. Even though the benefit of oversampling had been reported previously, the system of constraints appropriate for Cu_3Au could be expected to cause different behavior than that observed with other kinds of constraints. The angular resolution of the CCD, when mounted 2.95 m from the sample, was shown to be sufficient to allow an oversampling ratio in the measurement of four or greater, depending on the slit size. Based on the computer experiment of Chapter 4, this is thought to be sufficient.

The work presented here represents a step toward the goal of turning static CXD, coupled with iterative phase retrieval techniques, into a general imaging tool. The measurements needed for CXD are potentially routine using existing facilities. The algorithms, which effectively allow a computer to substitute for a lens, have been demonstrated effective in the simulations and have also been utilized successfully in the laser and soft x-ray regimes [81; 82]. A number of issues remain to be resolved, however.

CXD with current hard x-ray sources will always be best described as only par-

tially coherent. The effect that partial coherence will have on phase retrieval is still unknown. One way to simulate this would be to add a background term of the same form as the incoherent diffuse scattering of Figures 3.1 and 3.2 to the computed CXD patterns before reconstruction. This is only a valid test if an actual CXD signal can be modelled as a sum of coherent and incoherent parts, as discussed in Chapter 1. It may be possible, however, to account for partial coherence within the phase retrieval process itself. A proper description for the propagation of partially coherent radiation involves functional forms much more complicated than the Fourier transform, so it is quite likely that the computational problem of implementing such a phase retrieval algorithm will be difficult indeed. With the availability of focussing optics in the APS 33-ID beamline, one could continuously vary the spatial coherence length by magnification or demagnification of the source, so that with a given slit size, the effect of partial coherence could be explored.

The CXD patterns we obtained from Cu_3Au superstructure reflections are strikingly complex. In order to scale a pattern such as the one shown in Figure 3.7 so that we still have $\sigma \geq 2$, or preferably $\sigma \sim 4$, and yet retain the bulk of the information present in the measurements, we would require quite a large array size. The support of the real-space image must have dimensions of about 15 μm $\times$ 15 μm to contain the illumination of the sample from a 5 μm $\times$ 5 μm slit and account for Fresnel diffraction. With oversampling by a factor of two in each direction, for $\sigma = 4$, the physical size of the real-space array is then 30 μm $\times$ 30 μm. This requires the physical step size of the real-space array, Δ_x, to satisfy $N_x\Delta_x = 30$ μm. Therefore, the physical step size of the reciprocal-space array would be $\Delta_{q_x} = 2\pi/$ (30 μm), or 2.1×10^{-5} Å^{-1}. The reciprocal-space displacement between the pixels in the measurement was 3.3×10^{-5} Å^{-1}, and the CXD pattern had a signal clearly above background over a 768 $\times$ 512 pixel area. Thus, the CXD pattern should be interpolated into a 1200 $\times$ 800 pixel array to rescale the reciprocal-space step size to

2.1×10^{-5} Å^{-1}. Since most of the computing time is spent in the FFT, the execution time of which scales as $O(n \log n)$, a set of 50 fits with the same number of iterations each as was done in the simulation, but on a 1200 $\times$ 800 pixel array, would require on the order of ten days of computation on the 400 MHz Pentium II. This estimate assumes that the number of iterations required for convergence does not also scale up with the array size in some way. The problem of applying the phase retrieval techniques to real data would thus be greatly facilitated by modifying the experiment so that a smaller number of features were illuminated, which would yield a simpler CXD pattern.

We have already performed preliminary experiments to obtain CXD patterns from single 0.1 μm grains of gold. In those experiments, the grains themselves select the beam, and the slits are needed only to limit the illuminated grains to only a few at a time. Thus, the distortion of the phase due to Fresnel diffraction should be eliminated.

The outlook for CXD is quite promising. The use of XIFS for the study of fluctuating or diffusing systems has already produced results. The same facilities, when augmented with the techniques of phase retrieval for static CXD patterns, could become powerful tools for structural studies. The length scales which can be probed are relevant to many materials of interest: single biological cells, membranes, domains in polycrystalline materials, colloids, and localized defects. It may even be possible to reconstruct local strains in crystalline materials.

References

[1] S. Brauer, G. B. Stephenson, M. Sutton, R. Brüning, E. Dufresne, S. G. J. Mochrie, J. Als-Nielsen, G. Grübel, and D. L. Abernathy. "X-ray intensity fluctuation spectroscopy observation of critical dynamics in Fe_3Al." *Phys. Rev. Lett.* **74** 2010–2013 (1995).

[2] S. B. Dierker, R. Pindak, R. M. Fleming, I. K. Robinson, and L. Berman. "X-ray photon correlation spectroscopy study of brownian motion of gold colloids in glycerol." *Phys. Rev. Lett.* **75** 449–452 (1995).

[3] T. Thurn-Albrecht, W. Steffen, A. Patkowski, G. Meier, E. W. Fischer, G. Grübel, and D. L. Abernathy. "Photon correlation spectroscopy of colloidal palladium using a coherent x-ray beam." *Phys. Rev. Lett.* **77** 5437–5440 (1996).

[4] O. K. C. Tsui and S. G. J. Mochrie. "Dynamics of concentrated colloidal suspensions probed by x-ray correlation spectroscopy." *Phys. Rev. E* **57** 2030–2034 (1998).

[5] S. G. J. Mochrie, A. M. Mayes, A. R. Sandy, M. Sutton, S. Brauer, G. B. Stephenson, D. L. Abernathy, and G. Grübel. "Dynamics of block copolymer micelles revealed by x-ray intensity fluctuation spectroscopy." *Phys. Rev. Lett.* **78** 1275–1278 (1998).

[6] J. Mainville, F. Bley, F. Livet, E. Geissler, J. F. Legrand, D. L. Abernathy, G. Grübel, S. G. J. Mochrie, and M. Sutton. "Speckle structure in small-angle coherent x-ray scattering." *J. App. Cryst* **30** 828–832 (1997).

[7] A. Malik, A. R. Sandy, L. B. Lurio, G. B. Stephenson, S. G. J. Mochrie, I. McNulty, and M. Sutton. "Coherent x-ray study of fluctuations during domain coarsening." *Phys. Rev. Lett.* **81** 5832–5835 (1998).

[8] B. E. Warren. *X-ray Diffraction* (Addison-Wesley Publishing, Reading, Mass., 1969).

[9] J. J. Sakurai. *Advanced Quantum Mechanics* (Addison-Wesley, New York, 1967).

[10] C. H. MacGillavry and G. D. Rieck, editors. *International Tables for X-ray Crystallography*, volume III (Dordrecht, Boston, 1983).

[11] M. Born and E. Wolf. *Principles of Optics*, 6th edition (Pergamon Press, Oxford, 1980).

[12] B. L. Henke, E. M. Gullikson, and J. C. Davis. "X-ray interactions: photoabsorption, scattering, transmission, and reflection at E = 50-30000 eV, Z = 1-92." *Atomic Data and Nuclear Data Tables* **54** 181–342 (1993).

[13] P. H. van Cittert. "Die warhscheinliche schwingungsverteilung in einer von einer lichtquelle direkt oder mittels einer linse beleuchteten ebene." *Physica* **1** 201–210 (1934).

[14] F. Zernike. "The concept of degree of coherence and its application to optical problems." *Physica* **5** 785–795 (1938).

[15] J. W. Goodman. *Statistical Optics* (John Wiley and Sons, New York, 1985).

[16] F. C. Nix and W. Shockley. "Order-disorder transformations in alloys." *Rev. Mod. Phys.* **10** 1–71 (1938).

[17] H. Lipson. *Prog. Metal Phys.* **2** 1 (1950).

[18] L. Guttman. *Solid State Phys.* **3** 145 (1956).

[19] A. Guinier. *X-ray Diffraction in Crystals, Imperfect Crystals, and Amorphous Bodies* (W. H. Freeman and Company, San Francisco, 1963).

[20] X.-M. Zhu, H. Zabel, I. K. Robinson, E. Vlieg, J. A. Dura, and C. P. Flynn. "Surface-induced heterophase fluctuation." *Phys. Rev. Lett.* **65** 2692–2695 (1990).

[21] H. Dosch, L. Mailander, H. Reichert, and J. Peisl. "Long-range order near the $Cu_3Au(001)$ surface by evanescent X-ray scattering." *Phys. Rev. B* **43** 13172–13186 (1991).

[22] I. K. Robinson and P. J. Eng. "Near-surface and bulk short-range order in Cu_3Au." *Phys. Rev. B* **52** 9955–9963 (1995).

[23] H. Reichert, P. J. Eng, H. Dosch, and I. K. Robinson. "Thermodynamics of surface segregation profiles at $Cu_3Au(001)$ resolved by X-ray scattering." *Phys. Rev. Lett.* **74** 2006–2009 (1995).

[24] T. Hashimoto, K. Nishimura, and Y. Takeuchi. "Dynamics of transitional ordering process in Cu_3Au alloy from disordered state to ordered state." *J. Phys. Soc. Jpn.* **45** 1127–1135 (1978).

[25] Y. Noda, S. Nishihara, and Y. Yamada. "Critical behavior and scaling law in ordering process of the first order phase transition in Cu_3Au alloy." *J. Phys. Soc. Jpn.* **53** 4241–4249 (1984).

[26] K. F. Ludwig, Jr., G. B. Stephenson, J. L. Jordan-Sweet, J. Mainville, Y. S. Yang, and M. Sutton. "Nucleated and continuous ordering in Cu_3Au." *Phys. Rev. Lett.* **61** 1859–1862 (1988).

[27] S. E. Nagler, R. F. Shannon, Jr., C. R. Harkless, and M. A. Singh. "Time-resolved X-ray scattering study of ordering and coarsening in Cu_3Au." *Phys. Rev. Lett.* **61** 718–721 (1988).

[28] R. F. Shannon, Jr., C. R. Harkless, and S. E. Nagler. "Effect of extra Cu on ordering kinetics in thin films of Cu_3Au." *Phys. Rev. B* **38** 9327–9330 (1988).

[29] R. F. Shannon, Jr., S. E. Nagler, C. R. Harkless, and R. M. Nicklow. "Time-resolved X-ray scattering study of ordering kinetics in bulk single-crystal Cu_3Au." *Phys. Rev. B* **46** 40–54 (1992).

[30] P. Hirsch, A. Howie, R. B. Nicholson, D. W. Pashley, and M. J. Wheelan. *Electron Microscopy of Thin Crystals, Second Revised Edition* (Robert E. Krieger Publishing, Malabar, Fla., 1977).

[31] D. T. Keating and B. E. Warren. "Long-range order in beta-brass and Cu_3Au." *J. Appl. Phys* **22** 286–290 (1951).

[32] I. G. Edmunds, R. M. Hinde, and H. Lipson. *Nature* **160** 304 (1947).

[33] I. G. Edmunds and R. M. Hinde. *Proc. Phys. Soc.* **B65** 716 (1952).

[34] R. S. Appleton. private communication (1999).

[35] J. D. Jackson. *Classical Electrodynamics*, 3rd edition (John Wiley & Sons, New York, 1999).

[36] R. J. Dejus, B. Lai, E. R. Moog, and E. Gluskin. "Undulator A characteristics and specifications: enhanced capabilites." Argonne National Laboratory Technical Bulletin ANL/APS/TB-17 (1994).

[37] H. M. Bizek. "The Advanced Photon Source list of parameters." Argonne National Laboratory Technical Bulletin ANL/APS/TB-26 (1996).

[38] J. W. M. DuMond. "Theory of the use of more than two successive x-ray crystal reflections to obtain increased resolving power." *Phys. Rev.* **52** 872–883 (1937).

[39] S. Brauer, G. B. Stephenson, M. Sutton, S. G. J. Mochrie, S. B. Dierker, R. M. Fleming, R. Pindak, I. K. Robinson, G. Grübel, J. Als-Nielsen, and D. L. Abernathy. "Asymmetrically cut crystals as optical elements for highly collimated x-ray beams." *Rev. Sci. Instrum.* **66** 1506–1509 (1995).

[40] J. L. Libbert, J. A. Pitney, and I. K. Robinson. "Asymmetric Fraunhofer diffraction from roller-blade slits." *J. Synch. Rad.* **4** 125–127 (1997).

[41] W. R. Busing and H. A. Levy. "Angle calculations for 3- and 4-circle x-ray and neutron diffractometers." *Acta Cryst.* **22** 457–464 (1967).

[42] I. K. Robinson. "Four-circle diffractometry for surfaces." *Rev. Sci. Instrum.* **60** 1541–1544 (1989).

[43] H. Dosch, L. Mailander, A. Lied, J. Peisl, F. Grey, R. L. Johnson, and S. Krummacher. "Experimental evidence for an interface delocalization trainsition in Cu_3Au." *Phys. Rev. Lett.* **60** 2382–2385 (1988).

[44] Princeton Instruments, Inc. "High performance digital CCD cameras." Product Literature (1995).

[45] M. Sutton, S. G. J. Mochrie, T. Greytak, S. E. Nagler, L. E. Berman, G. A. Held, and G. B. Stephenson. "Observation of speckle by diffraction with coherent x-rays." *Nature* **352** 608–610 (1991).

[46] K. F. Ludwig, Jr. "Comment on 'speckle in the diffraction patterns of Hendricks-Teller and icosahedral glass models'." *Phys. Rev. Lett.* **61** 1526 (1988).

[47] D. Crawford. "gnuplot: An interactive plotting program." Software manual for gnuplot v. 3.7 (1998).

[48] D. L. Abernathy, G. Grübel, S. Brauer, I. McNulty, G. B. Stephenson, S. G. J. Mochrie, A. R. Sandy, N. Mulders, and M. Sutton. "Small-angle x-ray scattering using coherent undulator radiation at the ESRF." *J. Synch. Rad.* **5** 37–47 (1998).

[49] O. K. C. Tsui, S. G. J. Mochrie, and L. E. Berman. "Statistical analysis of x-ray speckle at the NSLS." *J. Synch. Rad.* **5** 30–36 (1998).

[50] J. W. Goodman. "Statistical properties of laser speckle patterns." In *Laser Speckle and Related Phenomena*, J. C. Dainty, editor, pp. 1–75 (Springer-Verlag, Heidelberg, 1975).

[51] S. Wolfram. *The Mathematica Book*, 3rd edition (Cambridge University Press, Cambridge, 1996).

[52] I. A. Vartaniants, J. A. Pitney, J. L. Libbert, and I. K. Robinson. "Reconstruction of surface morphology from coherent x-ray reflectivity." *Phys. Rev. B* **55** 13193–13202 (1997).

[53] I. K. Robinson, J. A. Pitney, J. L. Libbert, and I. A. Vartaniants. "Surface morphology by reflectivity of coherent x-rays." *Physica B* **248** 387–392 (1998).

[54] J. L. Libbert, R. Pindak, S. B. Dierker, and I. K. Robinson. "Speckle in coherent x-ray reflectivity from Si(111) wafers." *Phys. Rev. B* **56** 6454–6457 (1997).

[55] I. K. Robinson, J. L. Libbert, I. A. Vartaniants, J. A. Pitney, D. M. Smilgies, D. L. Abernathy, and G. Grübel. "Coherent x-ray diffraction imaging of silicon oxide growth." *Phys. Rev. B* (1999). To be published.

[56] M. Francon. *Holography*, expanded English edition (Academic Press, New York, 1974).

[57] P. M. Len, T. Gog, C. S. Fadley, and G. Materlik. "X-ray fluorescence holography and multiple-energy x-ray holography: A critical comparison of atomic images." *Phys, Rev. B* **55** R3323–R3327 (1997).

[58] P. M. Len, T. Gog, D. Novikov, R. A. Eisenhower, G. Materlik, and C. S. Fadley. "Multiple energy x-ray holography: Incident-radiation polarization effects." *Phys, Rev. B* **56** 1529–1539 (1997).

[59] M. Tegze, G. Faigel, S. Marchesini, M. Belakhovsky, and A. I. Chumakov. "Three dimensional imaging of atoms with isotropic 0.5 Å resolution." *Phys, Rev. Lett.* **82** 4847–4850 (1999).

[60] D. W. Green, V. M. Ingram, and M. F. Perutz. *Proc. Phys. Soc.* **A225** 287 (1954).

[61] C. Bokhoven, J. C. Shoone, and J. M. Bijroet. *Acta Cryst.* **4** 275 (1951).

[62] R. Pepinsky and Y. Okaya. *Proc. Nat. Acad. Sci. USA* **42** 286 (1956).

[63] Y. Yacoby. "Structure factor amplitude and phase determination by a new two beam diffraction interference method." *Sol. State Comm.* **91** 529–533 (1994).

[64] H. Baltes, Y. Yacoby, R. Pindak, R. Clarke, L. Pfeiffer, and L. Berman. "Measurement of the x-ray diffraction phase in a 2D crystal." *Phys, Rev. Lett.* **79** 1285–1288 (1997).

[65] J. R. Fienup and C. C. Wackerman. "Phase-retrieval stagnation problems and solutions." *J. Opt. Soc. Am. A* **3** 1897–1907 (1986).

[66] R. Barakat and G. Newsam. "Necessary conditions for a unique solution to two-dimensional phase recovery." *J. Math. Phys.* **25** 3190–3193 (1984).

[67] R. H. T. Bates. "Fourier phase problems are uniquely solvable in more than one dimension. I: Underlying theory." *Optik* **61** 247–262 (1982).

[68] K. L. Garden and R. H. T. Bates. "Fourier phase problems are uniquely solvable in more than one dimension. II: One-dimensional considerations." *Optik* **62** 131–142 (1982).

[69] W. R. Fright and R. H. T. Bates. "Fourier phase problems are uniquely solvable in more than one dimension. III: Computational examples for two dimensions." *Optik* **62** 219–230 (1982).

[70] W. Lawton. "Uniqueness results for the phase retrieval problem for radial functions." *J. Opt. Soc. Am.* **71** 1519–1522 (1981).

[71] J. H. Seldin and J. R. Fienup. "Numerical investigation of the uniqueness of phase retrieval." *J. Opt. Soc. Am. A* **7** 412–427 (1990).

[72] J. Miao, D. Sayre, and H. N. Chapman. "Phase retrieval from the magnitude of the Fourier transforms of nonperiodic objects." *J. Opt. Soc. Am. A* **15** 1662–1669 (1998).

[73] J. R. Fienup, T. R. Crimmins, and W. Holsztynski. "Reconstruction of the support of an object from the support of its autocorrelation." *J. Opt. Soc. Am.* **72** 610–624 (1982).

[74] R. W. Gerchberg and W. O. Saxton. "A practical algorithm for the determination of phase from image and diffraction plane pictures." *Optik* **35** 237–246 (1972).

[75] W. O. Saxton. *Computer Techniques for Image Processing in Electron Microscopy* (Academic Pres, Malabar, Fla., 1977).

[76] P. M. Hirsch. "Method of making and object-dependent diffuser." U.S. Patent 3,619,022.

[77] J. R. Fienup. "Phase retrieval algorithms: a comparison." *Appl. Opt.* **21** 2758–2769 (1982).

[78] R. P. Millane and W. J. Stroud. "Reconstructing symmetric images from their undersampled Fourier intensities." *J. Opt. Soc. Am. A* **14** 568–579 (1997).

[79] R. P. Millane and W. J. Stroud. "Phase retrieval from undersampled intensity data." In *Image Reconstruction and Restoration II*, T. J. Schulz, editor, volume 3170, pp. 116–127 (1997).

[80] J. Scheuer and M. Orenstein. "Optical vortices crystals: spontaneous generation in nonlinear semiconductor microcavities." *Science* **285** 230–233 (1999).

[81] J. N. Cederquist, J. R. Fienup, J. C. Marron, and R. G. Paxman. "Design and execution of a phase retrieval demonstration experiment." In *Digital Image Recovery and Synthesis*, P. S. Idell, editor, volume 828, pp. 190–194 (1987).

[82] J. Miao, P. Charalambous, J. Kirz, and D. Sayre. "Extending the methodology of x-ray crystallography to allow imaging of micrometre-sized non-crystalline specimens." *Nature* **400** 342–344 (1999).

Vita

John Allen Pitney was born on September 8, 1973, in Farmington, Missouri, to Marvin and Ruth Ann Pitney of Ironton, Missouri. He began undergraduate study at the University of Missouri-Columbia in August of 1991. While at the University of Missouri-Columbia, John received scholarship support from an ASARCO Foundation-sponsored National Merit Scholarship, a Missouri Higher Education Academic Scholarship, and departmental scholarships from the physics and mathematics departments. After receiving B.S. degrees in physics and in mathematics from the University of Missouri-Columbia in May, 1995, John began graduate studies at the University of Illinois at Urbana-Champaign in the Department of Physics. After two semesters as a teaching assistant for introductory physics courses, John began work as a research assistant with Professor Ian K. Robinson in the summer of 1996.